Computational Design of Wearable Chemical Sensors for Personalized Healthcare

Thesis by

Daniel Mukasa

In Partial Fulfillment of the Requirements for
the degree of
Doctor of Philosophy

CALIFORNIA INSTITUTE OF TECHNOLOGY
Pasadena, California

2024
(Defended July 2024)

Daniel Mukasa
ORCID: 0000-0001-8379-3648

ACKNOWLEDGEMENTS

I would like to express my deepest gratitude to my professor and scientific mentor Wei Gao. Over the past 5 years he has been an extraordinarily insightful and patient advisor. When I first joined the lab I was coming into medical engineering formally trained as a physicist. I had a long road to take to learn how to make chemical sensors, integrate them into a wearable device, and find a place for computational simulation to make an impact in this field. In many ways we found ourselves to be the first and only people in the field to develop some novel and very useful methods. Although this was challenging, every second was worth it and none of this would have been possible without your guidance.

I would also like to thank each member of my committee, Dr. William Goddard, Dr. Julia Kornfield and Dr. Keith Schwab, for their advice may it haven been purely scientific, career related, or life related. Each of you were instrumental in helping me become the scientist and person I am today. Events ranging from Goddard's weekly dinners where I could have talks with him and other students on how I could best use the computational methods they were experts in, to having lunch time chats with Kornfield and Schwab were invaluable. Each of you being so willing to help when I felt lost or did not know exactly what I was doing is what makes Caltech so special.

Inside the lab I would like to thank each member of the Gao lab for their help and support both scientifically and even emotionally or mentally. We have all created an extraordinarily high standard for our work and having each of you there for support has made a feeling of family that cant be replicated. I will always remember our camping trips we took and late night star gazing while having deep talks about science and the world.

I would also like to thank each of my friends in the Caltech community for helping me through my journey at this school. My time in organizations like the Black Scientist and Engineers of Caltech (BSEC) and the friends I made here and at other venues truly kept me hopeful even in the hardest parts of my degree.

Last but certainly not least I would like to thank my parents Eva and Herman Mukasa. Education has always been a central value for our family. You both moved from Uganda, the only place you knew as home at the time, to come to America and give me and my siblings a better chance at an education that could change our lives. All of your sacrifice, long hours working and commitment to making sure we live the best lives possible has not gone unnoticed. I'm living a life I used to only dream of when I grew up and none of that would be possible without you. Thank you for everything you've ever done.

ABSTRACT

Wearable sweat sensors have the potential to revolutionize precision medicine as they can non-invasively collect molecular information closely associated with an individual’s health status. However, the majority of clinically relevant biomarkers cannot be continuously detected in situ using existing wearable approaches. Molecularly imprinted polymers (MIPs) are a promising candidate to address this challenge but haven’t yet gained widespread use due to their complex design and optimization process yielding variable selectivity. Despite their promise, MIPs have historically been known to be exceedingly difficult to optimize. Changes in the monomer/monomers used, polymerization solvent, and crosslinking agent have been shown to change the performance of MIP sensors significantly. This is particularly a concern in sweat-based sensors where the concentration of analytes is very low and chemical diversity is very high as a drop of sweat can contain vitamins, hormones, and amino acids. Consequentially, any sweat based sensor must exhibit high sensitivity (ability to detect low analyte concentrations) and selectivity (ability to distinguish one analyte from another). Computational methods have been introduced to design MIP sensitivity alone, however these prior methods do not cover all aspects essential for using a sensor in a wearable device such as selectivity optimization, detection of non-electroactive analytes, and scalable manufacturing. Here, we introduce a full computational method that allows for high throughput materials discovery for wearable devices. We will describe how to design novel sensing materials with QuantumDock, an automated computational framework for universal MIP development toward wearable applications. Then we delve into further technical details on signal transduction and scalable manufacturing approaches for these wearable devices. We present a number of novel devices designed with these computational methods including a wearable non-invasive phenylalanine monitoring system (the first of its kind), a wearable nutritional tracker ‘Nutritrek’ capable of monitoring a range of metabolic disorders, and an implantable pharmaceutical drug monitoring system for cancer patients.

PUBLISHED CONTENT AND CONTRIBUTIONS

1. “Mukasa, D.; Wang, M.; Min, J.; Yang, Y.; Solomon, S. A.; Han, H.; Ye, C.; Gao, W. A Computationally Assisted Approach for Designing Wearable Biosensors toward Non-Invasive Personalized Molecular Analysis. Advanced Materials 2023, 35 (35), 2370246. https://doi.org/10.1002/adma.202212161”
2. “Wang, M.; Yang, Y.; Min, J.; Song, Y.; Tu, J.; Mukasa, D.; Ye, C.; Xu, C.; Heflin, N.; McCune, J. S.; Hsiai, T. K.; Li, Z.; Gao, W. A Wearable Electrochemical Biosensor for the Monitoring of Metabolites and Nutrients. Nature Biomedical Engineering 2022, 6, 1225–1235. https://doi.org/10.1038/s41551-022-00932-7”
3. “Min, J.; Tu, J.; Xu, C.; Lukas, H.; Shin, S.; Yang, Y.; Solomon, S. A.; Mukasa, D.; Gao, W. Skin-Interfaced Wearable Sweat Sensors for Precision Medicine. Chemical Reviews 2023, 123 (8), 5049–5138. https://doi.org/10.1021/acs.chemrev.2c00823.”
4. “Song, Y.; Mukasa, D.; Zhang, H.; Gao, W. Self-Powered Wearable Biosensors. Accounts of Materials Research, 2021, 2 (3), 184-197. https://doi.org/10.1021/accountsmr.1c00002.”
5. "Wang, M.; Ye, C.; Yang, Y.; Mukasa, D.; Wang, C.; Xu, C.; Min, J.; Solomon, S. A.; Tu, J.; Shen, G.; Tang, S.; Hsiai, T. K.; Li, Z.; McCune, J. S.; Gao, W. Printable molecule-selective core-shell nanoparticles for wearable and implantable sensing. Submitted to Nature Materials 2024."

TABLE OF CONTENTS

Chapter 1

INTRODUCTION

Modern diagnostic procedures in healthcare typically require going into a doctor's office and collecting biofluids such as blood or interstitial fluid which contain biomarkers. These biomarkers like glucose, A1C, cholesterol and a host of others are key for monitoring an individual's metabolic health in the long term. Regular monitoring of these metabolites in annual intervals has been associated with increased life expectancy to a margin of 10 years[1]. Currently clinicians only monitor these markers once a year, primarily due to the use of large and costly diagnostic equipment like high performance liquid chromatography, that resides in the hospital or off-site labs. This gives us the equivalent of a screenshot of human health.

The dynamic nature of human health however requires greater resolution to understand disease development and progression. It is well documented that cancer survival rates are highest with early diagnosis[2]. Similarly for many diseases including diabetes prevention yields better patient outcomes than treatment[3]. To facilitate early detection, wearable medical devices have become essential in healthcare. Devices like Dexcom's Glucometer and Abbott's FreeStyle Libre have shown the potential of wearable to give health data on the resolution of minutes, showing patients how each of their meals and daily activities impacts their blood sugar levels.

This concept of continuous monitoring can be carried further by monitoring more biomarkers than just glucose. Sweat-based wearables can non-invasively monitor biomarkers including ions, amino acids, hormones, and proteins in sweat.[4,5,6] These biomarkers can be used to monitor diseases including cancer, cystic fibrosis, gout, stress, and metabolic disorders as just a few examples.[7-10] The detection of said biomarkers relies on accurate biosensors for biomarker detection. Typical biosensors rely on antibodies, enzymes, or ion-selective to facilitate either selective binding or reactions to the biomarker of interest. Despite their success thus far, each of these sensing mechanisms faces challenges that limit their realistic application in wearable systems. While enzymes and ion-selective electrodes can specifically detect certain molecules, they typically cannot detect trace level biomarkers. This capability is essential in the case of sweat biomarkers which can reach concentrations as low as the nanomolar range.[11] Antibodies can exhibit lower detection limits but are limited to a single use making them incompatible for continuous health monitoring. Furthermore, these sensors are limited to a small set of biomarkers for which antibodies or enzymes already exist. Alternative techniques like differential pulse voltammetry (DPV) have been used to detect ultra-low concentrations of electroactive biomarkers from their oxidation current at a special voltage.[8] This oxidation current increases with increasing analyte concentration. However, this technique as well is limited to a small set of electroactive biomarkers and has limited selectivity as interfering molecules with similar oxidation potentials can’t be distinguished limiting the prosect of use in biofluids.

Molecularly imprinted polymers (MIPs) are a promising low-cost sensing solution that can join the highly sensitive detection capabilities of DPV with a selective and reusable sensing mechanism.[12] These sensors are fabricated by electropolymerizing and subsequently eluting a biomarker from a functional polymer matrix, leaving biomarker-shaped imprints. Such imprints facilitate selective rebinding of biomarkers as shown in **Figure 1-1a**, increasing the device selectivity. When used in tandem with voltametric techniques like

DPV, MIPs can achieve very low detection limits. Their detection capability can be expanded to non-electroactive biomarkers by integrating a redox layer under the imprinted polymer layer. Subsequent rebinding in this case lowers the probes redox current enabling accurate detection of various molecules. In order to prepare the MIP-sensors with high sensitivity, mass-producible low-cost laser-engraved graphene electrodes can be used as their offer particularly high electron transfer rates and thus could achieve low detection limits (**Figure 1-2**).[13] This can facilitate the detection of swear biomarkers like tryptophan and leucine at their trace physiological concentration, as shown in **Figure 1-1b**. Along with these superior sensing capabilities, MIPs can be used multiple times by eluting rebound biomarkers with an electric current, enabling reusable of these highly specific biosensors.

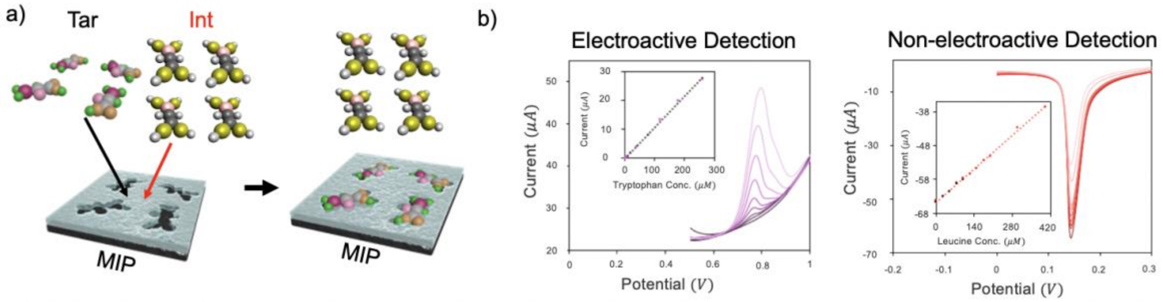

Figure 1-1*: a) Selective absorption of biomarkers by a MIP layer b) Electrochemical detection of both an electroactive target Tryptophan and a non-electroactive target Leucine*

These sensors have not gained mainstream acceptance as biosensors however due to their complex design process. Ones choice of functional monomer dramatically influences sensor selectivity rendering some MIPs ineffective in biofluids. Computational methods like density functional theory (DFT) and molecular docking (MD) are ideal tools for simplifying the MIP design process. These methods use ab-initio calculations to model physical interactions between molecules. They are commonly used in MIP development to rationally choose functional monomers by simulating binding energies between monomers and biomarkers.

Such binding energies can quickly be calculated between a target biomarker and a library of potential functional monomers in the design process. This method has produced a number of successful MIPs,[14] but is fundamentally limited. Maximizing the biomarker-monomer binding energy may adversely impact selectivity by promoting non-selective binding, as a high binding energy to one biomarker may also imply a high binding energy to an unwanted interferent molecules. Selectivity in particular is traditionally still left to experimental optimization which costs a tremendous amount of time and resources. This metric however is critical for wearable sweat based devices where we must distinguish between classes of molecules with similar structure (i.e. amino acids) which MIPs do not inherently differentiate between easily.

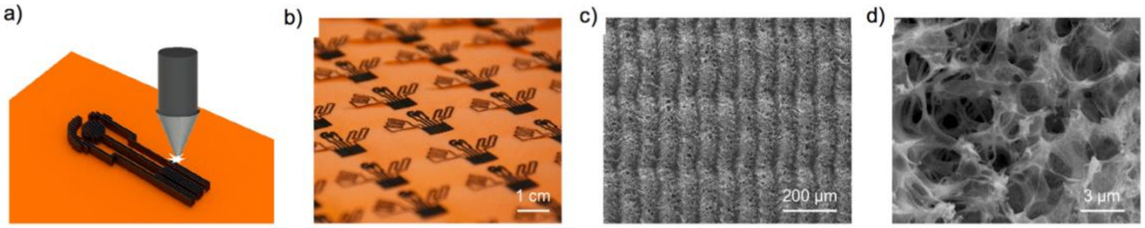

Figure 1-2: Large-scale low-cost fabrication of highly sensitive graphene-based sensor via laser engraving

In the reminder of this thesis, we will detail each of the essential components of a wearable device including sensing modalities, signal transduction, sensor data analysis, and detail how computational methods like DFT can be used to accelerate each bottleneck of production. Will conclude with remarks on scaling manufacturing and future remarks on how computational methods will improve in the future of AI and machine learning.

BIBLIOGRAPHY

[1] Shao, H., Guo, J., Singh Ospina, N. "Life expectancy and diabetes: Gains associated with control of glycemic and cardiovascular risk factors." JAMA Netw. Open, 2022, 5(5), e2211627.

[2] Hawkes, N. Cancer survival data emphasise importance of early diagnosis. BMJ, 2019, 364, l408. https://doi.org/10.1136/bmj.l408

[3] Hawkes, N. Rise in type 2 diabetes shows that prevention is more important than ever. BMJ, 2023, 380, e065214. https://doi.org/10.1136/bmj.e065214.

[4] Yang, Y., Gao, W. Wearable and flexible electronics for continuous molecular monitoring, Chem. Soc. Rev., 2019, 48, 1465–1491.

[5] Kim, J et al. Wearable biosensors for healthcare monitoring, Nat. Biotechnol., 2019, 37, 389-406

[6] Bariya, M., Nyein, H.Y.Y., Javery, A, Nat. Electron., 2018, 1, 160-171

[7] Mena-Bravo, A., Luque de Castro, M.D., Sweat: A sample with limited present applications and promising future in metabolomics, J. Pharm. Biomed. 2014, 90, 139–147.

[8] Yang, Y. et al. A laser-engraved wearable sensor for sensitive detection of uric acid and tyrosine in sweat, Nat. Biotechnol., 2020, 38, 217–224.

[9] Torrente-Rodriguez, R. M. et al. Investigation of Cortisol Dynamics in Human Sweat Using a Graphene Based Wireless mHealth System, Matter, 2020, 2, 921-937

[10] Gao, W. et al. Fully integrated wearable sensor arrays for multiplexed *in situ* perspiration analysis, Nature, 2016, 529, 509-514

[11] Harvey, C.J., LeBouf, R.F., Stefaniak, A.B. Formulation and stability of a novel artificial human sweat under conditions of storage and use, Tocicol. In Vitro, 2010, 24, 1790-1796.

[12] Wackerlig, J., Schirhagl, R., Applications of Molecularly Imprinted Polymer Nanoparticles and Their Advances toward Industrial Uses: A Review, Anal. Chem., 2016, 88, 250-261.

[13] Tehrani, F., Bavarian, T. Facile and scalable disposable sensor based on laser engraved graphene for electrochemical glucose detection, Sci. Rep., 2016, 6, 27975.

[14] Cowen, T., Karim, K.m Piletsky, S. Computational approaches in the design of synthetic receptors – A review, Anal. Chim. Acta., 2016, 936, 62-74.

Chapter 2

Biosensing modalities

Materials from this chapter adapted from “Song, Y.; Mukasa, D.; Zhang, H.; Gao, W. Self-Powered Wearable Biosensors. Accounts of Materials Research, 2021, 2 (3), 184-197. https://doi.org/10.1021/accountsmr.1c00002.”

Introduction

In recent years, wearable electronics have greatly improved the quality of daily life and have become indispensable tools[1,2]. Wearable devices targeted for detecting diversified biophysical and biochemical signals offer a noninvasive means for extracting physiological indicators[3,4]. The real-time monitoring of these indicators can provide valuable information for the early diagnosis and prevention of a number of health conditions such as cardiovascular diseases, gout, diabetes, and coronavirus disease 2019 (COVID-19)[5-8]. Emerging nanotechnology, materials science, and flexible electronics have led to wearable biophysical sensors that are capable of monitoring human activities, body motion, and electrophysiological signals (e.g., electroencephalogram (EEG) and electrocardiogram (ECG))[1,3]. In addition, wearable biochemical sensors are emerging for noninvasive detection of molecular-level indicators (e.g., electrolytes and metabolites) from biofluids[9,10].

This chapter provides a systematic introduction and highlights recent advances of self-powered wearable biosensors in the field of personalized healthcare. Section 2.1 introduces sensing technologies and preparation methods of wearable biochemical sensors. Section 2.2 discusses wearable biophysical sensors that are available for noninvasively measuring biopotentials, physical motions, and optical signals associated with human activities. With the conformal attachment on the skin, they can detect various physical indicators. By exploiting different essential sensing elements, wearable biochemical sensors realize continuous tracking of chemical biomarkers from biofluids that indicate health status and allow for an early disease diagnosis.

2.1 Wearable Biochemical Sensors

Considering that wearable biophysical sensors only monitor vital signs and physical activities, wearable biochemical sensors are essential to assess the human health state at the biomolecular level. Biofluids, such as saliva, tears, sweat, and interstitial fluids, are ideal analytes, as they can be retrieved noninvasively and contain a wealth of physiological information[8]. With techniques including potentiometry, amperometry, voltammetry, and impedance spectroscopy, wearable biochemical sensors can continuously monitor dynamic variations of biomarkers in biofluids[9]. Biomarkers including ions, metabolites, amino acids, hormones, and drugs can be detected to monitor or diagnose conditions like cystic fibrosis, gout, mental disorders, and drug abuse[8].

2.1.1 Enzymatic and Ion-Selective Sensors

Metabolites and electrolytes in biofluids are excellent indicators of a healthy state and can provide warnings for various diseases[38]. For example, an imbalance of glucose leads to severe threats to human health for individuals afflicted with diabetes mellitus, and increased lactate levels can correspond to cardiac diseases, endotoxic shock, or liver disease. Concentrations of ions including sodium, potassium, and calcium are also markers for dehydration during exercise activities. Key metabolites such as glucose and lactate can be monitored with amperometric enzymatic sensors, while a number of electrolytes (e.g., Na^+, K^+, NH_4^+, and Ca^{2+}) can alternatively be detected via potentiometric ion-selective sensors. **Figure 2-1A** demonstrates an electrochemical sensor array consisting of enzymatic and ion-selective sensors that can simultaneously monitor lactate and glucose as well as sodium and potassium ions in sweat via amperometric and potentiometric techniques, respectively[14]. In some special cases, a combination of enzymatic and potentiometric sensors is sometimes needed to realize an accurate detection of a given analyte. For example, an enzymatic urea sensor can be developed based on an NH_4^+ ion-selective electrode (**Figure 2-1B**)[17]. The urease layer of the sensor converts urea to

NH_4^+, which is subsequently detected. This combination of sensors allows for a real-time monitoring of urea in sweat.

2.1.2 Voltammetric Sensor

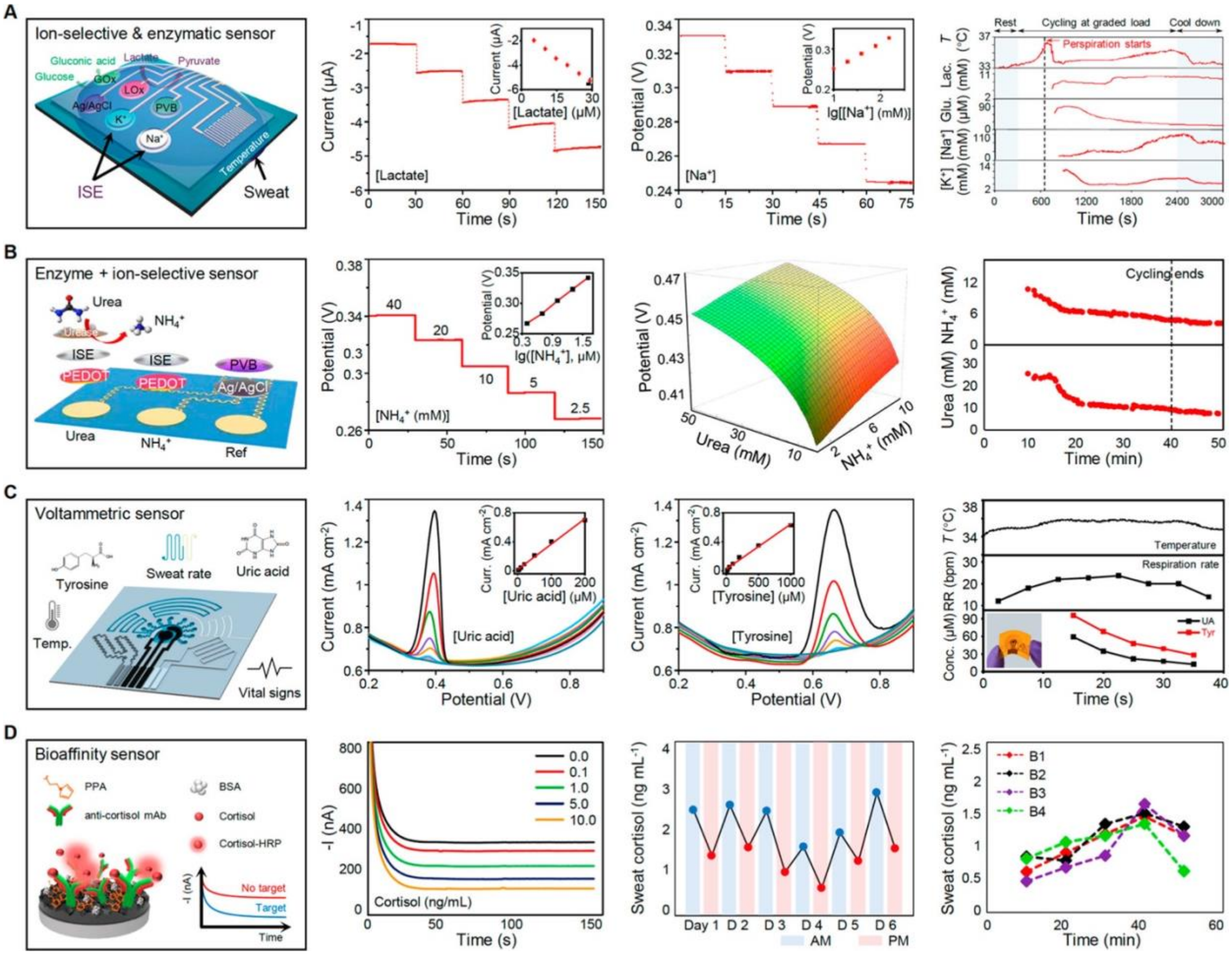

Figure 2-1: Wearable biochemical sensors. (A) Enzymatic and ion-selective sensors for a continuous analysis of metabolites and electrolytes. Reproduced with permission from ref (14). Copyright 2016 Springer Nature. (B) Enzymatic sensors based on ion-selective electrodes for a continuous urea sensing. Reproduced with permission from ref (17). Copyright 2020 American Academy for the Advancement of Science. (C) Voltammetric sensor for a sensitive detection of uric acid and tyrosine. Reproduced with permission from ref (15). Copyright 2020 Springer Nature. (D) Bioaffinity sensor based on the antibody–antigen interactions for a cortisol analysis. Reproduced with permission from ref (42). Copyright 2020 Elsevier.

Voltammetric sensors are the most relevant methods for the rapid and accurate detection of electroactive analytes. Similar to amperometric sensors, voltammetric sensors adopt a three-electrode configuration. The measured potential dramatically increases at a redox potential within the oxidization/reduction range of the analytes. Electroactive analytes, such as certain drugs, amino acids, and vitamins, can be directly oxidized at a specific potential. To achieve a high sensitivity and low detection limits, pulsed techniques such as differential pulse voltammetry (DPV) are commonly used to measure analyte oxidation. **Figure 2-1C** illustrates a wearable voltammetric sensor for continuously monitoring the uric acid and tyrosine in human sweat[15]. The laser-engraved graphene (LEG) biochemical sensor exhibits great selectivity and sensitivity within the target's physiological concentration range in sweat. For on-body validation, the integration of a multi-inlet microfluidic module and the LEG-based voltammetric sensors ensures a reliable analysis process with a high accuracy and temporal resolution. Combined with a preconcentration process, voltammetric sensors can also be used to monitor heavy metal ions (e.g., Cu^{2+}, Zn^{2+}, and Pb^{2+}) in biofluids[39].

2.1.3 Bioaffinity Sensor

Despite the current challenges for wearable implementation, bioaffinity sensors have emerged as an efficient and powerful analysis method for analyzing a broad spectrum of biomarkers, including protein, peptides, and hormones[40-42]. In general, bioaffinity sensors work via a specific detection of target-bioreceptor interactions (such as antigen–antibody binding). **Figure 2-1D** shows one example in which the antibody-based immunosensors are applied to monitor the dynamics of cortisol in biofluids[42]. Cortisol is linked to chronic stress, which enhances the threats of depression, anxiety, suicide, fragile immune system, and cardiovascular diseases. The fully integrated mHealth system is capable of measuring the cortisol diurnal cycle and the dynamic stress-response profile noninvasively on the body.

2.2. Wearable Biophysical Sensors

2.2.1 Pressure and Strain Sensors

Epidermal pressure and strains caused by the arterial pulse, human motion, and breathing rate are closely related to human physiological activity[3]. Soft wearable tactile sensors are also of great importance for applications in personalized healthcare, electronic skin, and prosthesis control[24]. Wearable pressure and strain sensors operate by detecting stimuli via changes in sensor material properties including piezoresistive, capacitive, piezoelectric, and triboelectric effects.

Piezoresistive pressure sensors are prevalent due to their cost-efficient fabrication, simple designs, and easy acquisition of both static and dynamic responses. Active materials including conductive polymers, carbon nanotubes, graphene, and nanowires are promising candidates with mechanical robustness and electrical reliability[25]. Microstructure-engineered designs such as wrinkles, cracks, woven materials, and porous materials can greatly enhance the sensitivity by accommodating geometrical deformations[25]. The synergistic effect of actively conductive materials with intrinsic structure provides a feasible approach to obtain a satisfying performance. Capacitive pressure sensors perform with both high sensitivity and low hysteresis. The microstructured dielectric layer allows for the detection of subtle changes in pressure[26]. Piezoelectric and triboelectric pressure sensors provide suitable approaches to dynamic measurements with fast responses and high signal-to-noise ratios. Upon deformation, mechanical to electrical energy conversion occurs allowing for a quantification of applied pressure. Thus, wearable pressure sensors that exploit different sensing modalities have a broad utility in health monitoring, human–machine interfaces, and soft robotics applications[24]. **Figure 2-2A** shows a porous piezoresistive pressure sensor based on a carbon nanotube–poly(dimethylsiloxane) (CNT-PDMS) conductive elastomer through a solution-evaporation fabrication method[20]. With an optimized dimension and content ratio, this pressure sensor achieves 0.51 kPa^{-1} in a 2 kPa linear region and induces stable resistance responses in accordance to the joint bending states, as well as other muscle movements.

The conventional strain sensors, mainly based on brittle materials, typically suffer from low stretchability and are inappropriate for the detection of human motion. Two mainstream strategies are available to construct stretchable conductive materials. The first involves introducing stretchability into intrinsically brittle materials to develop different geometric patterns, such as cracks and buckled structures[27]. The second strategy adopts percolating conductive nanomaterial networks including nanoparticles, nanowires, and nanotubes[25]. On the basis of these strategies, **Figure 2-2B** presents a highly robust and stretchable strain sensor by a three-dimensional (3D) self-assembly of carbon nanotubes and microsphere composites[28]. When the strain sensor is stretched, an applied stress induces the disconnection of overlapped carbon nanotubes due to the weak interfacial binding and large stiffness mismatch between the stretchable elastomer matrix and nanomaterials, resulting in an increasing electrical resistance.

2.2.2 Temperature Sensor

Body temperature is a critical indicator to monitor human activities and determine health conditions. It maintains an extraordinarily narrow range between 36 and 37 °C through thermoregulation, and abnormal changes provide insightful information related to cardiovascular health, cognitive condition, wound healing, and many other syndromes[29]. Traditional methods rely on simple thermometers and are not applicable for a continuous point-of-care use. Temperature-sensitive materials embedded in a flexible or stretchable substrate can exhibit a high sensitivity, fast response, long-term reliability, and skin compatibility. Zhu et al. present circuit design strategies to improve the accuracy and robustness of a wearable temperature sensor based on stretchable carbon nanotube transistors (**Figure 2-2C**)[30]. The stretchable temperature sensor circuit can trace sensor output as a function of temperature, and negligible change in the temperature output occurs under a repeatedly uniaxial strain of 15% in the device. To further minimize the strain-induced errors, smaller feature sizes will enable the integration of instrumentation electronics closer to the sensor elements and thereby allow an accurate temperature monitoring under different stretching strains.

2.2.3 Humidity Sensor

Besides the measurement of the typically physical parameters mentioned above, the analysis of skin humidity can yield insights into various aspects of physiological health. A real-time measurement of the hydration levels of human skin can be used to monitor respiration and water evaporation[31], which are important in monitoring disease states and in assessing factors related to an abnormal skin response. **Figure 2-2D** shows a wearable humidity sensor with a wrinkled CNT-PDMS, the resistance of which changes due to the presence of water molecules[32]. The wrinkled structure supports a more hydrophilic and anisotropic wetting surface with an enlarged surface area, thus enhancing the humidity sensing performance. Through the modulation of the CNT ratio, the wearable humidity sensor shows great sensitivity and reliable repeatability, especially in human motion or breathing monitoring.

2.2.4 Electrophysiological Sensor

Biopotential signals are effective indicators for medical diagnosis and health monitoring. Wearable electrophysiological sensors are available to measure biopotentials including ECG, EEG, electromyography (EMG), and electrooculography (EOG) noninvasively[1,3]. These informative signals can be used to monitor heart, brain, muscle, and eye activities, respectively. To acquire weak biopotential signals, wearable electrophysiological sensors with skin-compatible materials should perform with high signal-to-noise ratios, stable adhesion, and low motion artifacts for accurate signal processing[33]. Furthermore, functional materials with an optimal modulus, minimal skin irritation, and long-term usage offer compelling benefits to achieve a seamless and conformal contact with human skin. Son et al. employed self-healing electrodes as active components to fabricate a wearable ECG sensor composed of three electrodes (**Figure 2E)**[34]. The sensor achieves ECG data acquisition through the percolated CNT network in a polymer matrix and is capable of returning to its original state within seconds even after the damage occurred.

2.2.5 Optical Vital Sign Monitor

Optical sensors capture the amount of light either transmitted or scattered and convert signal changes into electrical outputs. Wearable optical sensors have utilized nanostructured materials like quantum dots, nanocrystals, two-dimensional (2D) materials, and perovskite materials to provide clinically relevant information for disease diagnosis and treatment[35]. Optical analysis of the blood flow, for example, allows for the calculation of key physiological parameters such as arterial oxygen saturation via pulse oximetry and heart rate variability via photoplethysmography (PPG)[36]. An example in **Figure 2-2F** shows a wearable optical sensor powered by a near-field communication (NFC) technology for a wireless optical characterization of the skin[37]. Arterial pulse waves temporally modulate the backscattered light, and the measured signals reveal both systolic peaks and dicrotic notches, which are relevant to both remote diagnostics and health warnings. Wearable optical sensors require a high photoresponse sensitivity and flexibility to ensure an efficient transport of photogenerated carriers and minimize motion artifacts. Ultimately these sensors must be able to measure parameters such as flow rate, pulse wave velocities, and heart disease. Integrating a device with both wearable optical sensors and other biophysical sensors can facilitate a multimodal network of sensors across the body, allowing for a more complete assessment of one's health status.

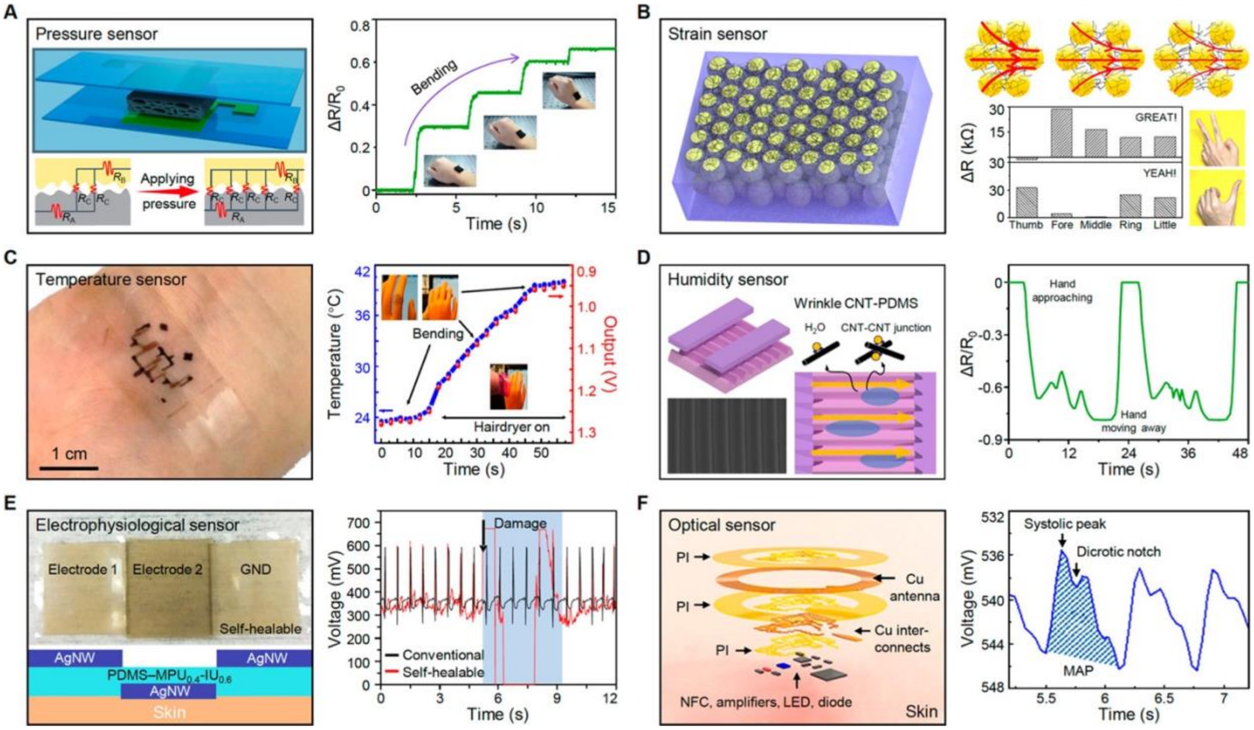

Figure 2-2: Wearable biophysical sensors. (A) Porous CNT-PDMS based piezoresistive pressure sensor for body motion monitoring. Reproduced with permission from ref (20). Copyright 2018 Elsevier. (B) Strain sensor with immobilized MWCNT networks for finger gesture recognition. Reproduced with permission from ref (28). Copyright 2017 Wiley-VCH. (C) Stretchable temperature sensor for strain-independent temperature sensing. Reproduced with permission from ref (30). Copyright 2018 Springer Nature. (D) Wrinkled CNT-PDMS as a humidity sensor for hand approaching detection. Reproduced with permission from ref (32). Copyright 2019 American Chemical Society. (E) Self-healable electrocardiogram sensor for measurement of cardiac signals. Reproduced with permission from ref (34). Copyright 2018 Springer Nature. (F) Epidermal optical sensor for heart rate and mean arterial pressure recording. Reproduced with permission from ref (37). Copyright 2016 American Academy for the Advancement of Science.

BIBLIOGRAPHY

1. Minglu Hu, Pei He, Weikai Zhao, Xianghui Zeng, Jiaorui He, Yucheng Chen, Xiaowen Xu, Jia Sun, Zheling Li, Junliang Yang. Machine Learning-Enabled Intelligent Gesture Recognition and Communication System Using Printed Strain Sensors. *ACS Applied Materials & Interfaces* **2023**, *15* (44) , 51360-51369. https://doi.org/10.1021/acsami.3c10846
2. Anubha Yadav, Rahul Patil, Saikat Dutta. Advanced Self-Powered Biofuel Cells with Capacitor and Nanogenerator for Biomarker Sensing. *ACS Applied Bio Materials* **2023**, *6* (10) , 4060-4080. https://doi.org/10.1021/acsabm.3c00640
3. Zongman Zhang, Zhongtai Zhu, Pengcheng Zhou, Yunfan Zou, Jiawei Yang, Hossam Haick, Yan Wang. Soft Bioelectronics for Therapeutics. *ACS Nano* **2023**, *17* (18) , 17634-17667. https://doi.org/10.1021/acsnano.3c02513
4. Junjie Qin, Wei Wang, Lixin Cao. Photonic Hydrogel Sensing System for Wearable and Noninvasive Cortisol Monitoring. *ACS Applied Polymer Materials* **2023**, *5* (9) , 7079-7089. https://doi.org/10.1021/acsapm.3c01119
5. Debmalya Roy, Vaishnav B, Sarathlal Koyiloth Vayalil, Ajay Gupta, N. Eswara Prasad, Benedikt Sochor, Matthias Schwartzkopf, Stephan V. Roth, Tobias Kraus. In Situ Study of Structure Formation under Stress in Stretchable Conducting Nanocomposites. *The Journal of Physical Chemistry Letters* **2023**, *14* (25) , 5834-5840. https://doi.org/10.1021/acs.jpclett.3c00929
6. Dalia Jane Saldanha, Anqi Cai, Noémie-Manuelle Dorval Courchesne. The Evolving Role of Proteins in Wearable Sweat Biosensors. *ACS Biomaterials Science & Engineering* **2023**, *9* (5) , 2020-2047. https://doi.org/10.1021/acsbiomaterials.1c00699

7. Neelkanth M. Bardhan, (Guest Editor)Milica Radisic, (Guest Editor)Md Nurunnabi (Guest Editor). Bioinspired Materials for Wearable Diagnostics and Biosensors. *ACS Biomaterials Science & Engineering* **2023**, *9* (5) , 2015-2019. https://doi.org/10.1021/acsbiomaterials.3c00348
8. Jihong Min, Jiaobing Tu, Changhao Xu, Heather Lukas, Soyoung Shin, Yiran Yang, Samuel A. Solomon, Daniel Mukasa, Wei Gao. Skin-Interfaced Wearable Sweat Sensors for Precision Medicine. *Chemical Reviews* **2023**, *123* (8) , 5049-5138. https://doi.org/10.1021/acs.chemrev.2c00823
9. Yanni Bi, Mimi Sun, Jingjuan Wang, Ziyu Zhu, Jing Bai, Mohammed Y. Emran, Ahmed Kotb, Xiangjie Bo, Ming Zhou. Universal Fully Integrated Wearable Sensor Arrays for the Multiple Electrolyte and Metabolite Monitoring in Raw Sweat, Saliva, or Urine. *Analytical Chemistry* **2023**, *95* (16) , 6690-6699. https://doi.org/10.1021/acs.analchem.3c00361
10. Yifei Luo, Mohammad Reza Abidian, Jong-Hyun Ahn, Deji Akinwande, Anne M. Andrews, Markus Antonietti, Zhenan Bao, Magnus Berggren, Christopher A. Berkey, Christopher John Bettinger, Jun Chen, Peng Chen, Wenlong Cheng, Xu Cheng, Seon-Jin Choi, Alex Chortos, Canan Dagdeviren, Reinhold H. Dauskardt, Chong-an Di, Michael D. Dickey, Xiangfeng Duan, Antonio Facchetti, Zhiyong Fan, Yin Fang, Jianyou Feng, Xue Feng, Huajian Gao, Wei Gao, Xiwen Gong, Chuan Fei Guo, Xiaojun Guo, Martin C. Hartel, Zihan He, John S. Ho, Youfan Hu, Qiyao Huang, Yu Huang, Fengwei Huo, Muhammad M. Hussain, Ali Javey, Unyong Jeong, Chen Jiang, Xingyu Jiang, Jiheong Kang, Daniil Karnaushenko, Ali Khademhosseini, Dae-Hyeong Kim, Il-Doo Kim, Dmitry Kireev, Lingxuan Kong, Chengkuo Lee, Nae-Eung Lee, Pooi See Lee, Tae-Woo Lee, Fengyu Li, Jinxing Li, Cuiyuan Liang, Chwee Teck Lim, Yuanjing Lin, Darren J. Lipomi, Jia Liu, Kai Liu, Nan Liu, Ren Liu, Yuxin Liu, Yuxuan Liu, Zhiyuan Liu, Zhuangjian Liu, Xian Jun

Loh, Nanshu Lu, Zhisheng Lv, Shlomo Magdassi, George G. Malliaras, Naoji Matsuhisa, Arokia Nathan, Simiao Niu, Jieming Pan, Changhyun Pang, Qibing Pei, Huisheng Peng, Dianpeng Qi, Huaying Ren, John A. Rogers, Aaron Rowe, Oliver G. Schmidt, Tsuyoshi Sekitani, Dae-Gyo Seo, Guozhen Shen, Xing Sheng, Qiongfeng Shi, Takao Someya, Yanlin Song, Eleni Stavrinidou, Meng Su, Xuemei Sun, Kuniharu Takei, Xiao-Ming Tao, Benjamin C. K. Tee, Aaron Voon-Yew Thean, Tran Quang Trung, Changjin Wan, Huiliang Wang, Joseph Wang, Ming Wang, Sihong Wang, Ting Wang, Zhong Lin Wang, Paul S. Weiss, Hanqi Wen, Sheng Xu, Tailin Xu, Hongping Yan, Xuzhou Yan, Hui Yang, Le Yang, Shuaijian Yang, Lan Yin, Cunjiang Yu, Guihua Yu, Jing Yu, Shu-Hong Yu, Xinge Yu, Evgeny Zamburg, Haixia Zhang, Xiangyu Zhang, Xiaosheng Zhang, Xueji Zhang, Yihui Zhang, Yu Zhang, Siyuan Zhao, Xuanhe Zhao, Yuanjin Zheng, Yu-Qing Zheng, Zijian Zheng, Tao Zhou, Bowen Zhu, Ming Zhu, Rong Zhu, Yangzhi Zhu, Yong Zhu, Guijin Zou, Xiaodong Chen. Technology Roadmap for Flexible Sensors. *ACS Nano* **2023**, *17* (6) , 5211-5295. https://doi.org/10.1021/acsnano.2c12606

11. Xingchen Ma, Chao Song, Fei Zhang, Ying Dai, Pengfei He, Xiaoqing Zhang. Soft, Multifunctional, Robust Film Sensor Using a Ferroelectret with Significant Longitudinal and Transverse Piezoelectric Activity for Biomechanical Monitoring. *ACS Applied Materials & Interfaces* **2022**, *14* (45) , 51291-51300. https://doi.org/10.1021/acsami.2c14378
12. Yaotian Wu, Eric Bakker. Self-Powered Signal Transduction of Ion-Selective Electrodes to an Electronic Paper Display. *ACS Sensors* **2022**, *7* (10) , 3201-3207. https://doi.org/10.1021/acssensors.2c01826
13. Hossein Roghani-Mamaqani Hanieh Mardani . Types of Surface Modifications of Carbon Nanotubes. , 67-90. https://doi.org/10.1021/bk-2022-1424.ch004

14. Shengli Zhai, Yuan Chen. Graphene-Based Fiber Supercapacitors. *Accounts of Materials Research* **2022**, *3* (9) , 922-934. https://doi.org/10.1021/accountsmr.2c00087
15. Suvrajyoti Mishra, Smita Mohanty, Ananthakumar Ramadoss. Functionality of Flexible Pressure Sensors in Cardiovascular Health Monitoring: A Review. *ACS Sensors* **2022**, *7* (9) , 2495-2520. https://doi.org/10.1021/acssensors.2c00942
16. Yuan Zhang, Hao Zhu, Zi Ying, Xinghua Gao, Wei Chen, Yueping Zhan, Lingyan Feng, Chung Chiun Liu, Yifan Dai. Design and Application of Metal Organic Framework ZIF-90-ZnO-MoS2 Nanohybrid for an Integrated Electrochemical Liquid Biopsy. *Nano Letters* **2022**, *22* (16) , 6833-6840. https://doi.org/10.1021/acs.nanolett.2c01613
17. Yaotian Wu, Eric Bakker. Direct Energy Transfer from a pH Glass Electrode to a Liquid Crystal Display. *Analytical Chemistry* **2022**, *94* (29) , 10408-10414. https://doi.org/10.1021/acs.analchem.2c01557
18. Xun Zhao, Guorui Chen, Yihao Zhou, Ardo Nashalian, Jing Xu, Trinny Tat, Yang Song, Alberto Libanori, Shili Xu, Song Li, Jun Chen. Giant Magnetoelastic Effect Enabled Stretchable Sensor for Self-Powered Biomonitoring. *ACS Nano* **2022**, *16* (4) , 6013-6022. https://doi.org/10.1021/acsnano.1c11350
19. Yude Su, Lu Lu, Ming Zhou. Wearable Microbial Fuel Cells for Sustainable Self-Powered Electronic Skins. *ACS Applied Materials & Interfaces* **2022**, *14* (7) , 8664-8668. https://doi.org/10.1021/acsami.2c00313
20. Maggie M. Potter, Megan E. Phelan, Pradeep Balaji, Phillip Jahelka, Haley C. Bauser, Rebecca D. Glaudell, Cora M. Went, Michael J. Enright, David R. Needell, André Augusto, Harry A. Atwater, Ralph G. Nuzzo. Silicon Heterojunction Microcells. *ACS Applied Materials & Interfaces* **2021**, *13* (38) , 45600-45608. https://doi.org/10.1021/acsami.1c11122

21. Zhang Dai, Ning Wang, Yang Yu, Ye Lu, Longlong Jiang, Di-An Zhang, Xiaoxiong Wang, Xu Yan, Yun-Ze Long. One-Step Preparation of a Core-Spun Cu/P(VDF-TrFE) Nanofibrous Yarn for Wearable Smart Textile to Monitor Human Movement. *ACS Applied Materials & Interfaces* **2021**, *13* (37) , 44234-44242. https://doi.org/10.1021/acsami.1c10366
22. Roozbeh Ghaffari, Da Som Yang, Joohee Kim, Amer Mansour, John A. Wright, Jr., Jeffrey B. Model, Donald E. Wright, John A. Rogers, Tyler R. Ray. State of Sweat: Emerging Wearable Systems for Real-Time, Noninvasive Sweat Sensing and Analytics. *ACS Sensors* **2021**, *6* (8) , 2787-2801. https://doi.org/10.1021/acssensors.1c01133
23. Seung-Mo Kang, Jung Ho Shin, Jeong Hyeon Kim, Hyun Seok Kang, Chang Kyu Jeong, Han Eol Lee, Byeong-Soo Bae. Polarity control of siloxane composite films for triboelectric nanogenerator based self-powered body temperature monitoring. *Nano Energy* **2024**, *127* , 109742. https://doi.org/10.1016/j.nanoen.2024.109742
24. Akhilesh Kumar Gupta, Alexey Viktorovich Krasnoslobodtsev. Fueling the Future: The Emergence of Self-Powered Enzymatic Biofuel Cell Biosensors. *Biosensors* **2024**, *14* (7) , 316. https://doi.org/10.3390/bios14070316
25. Md. Harun-Or-Rashid, Most. Nazmin Aktar, Veronica Preda, Noushin Nasiri. Advances in electrochemical sensors for real-time glucose monitoring. *Sensors & Diagnostics* **2024**, *3* (6) , 893-913. https://doi.org/10.1039/D4SD00086B
26. Brij Mohan, Virender, Rakesh Kumar Gupta, Armando J. L. Pombeiro, Alexander A. Solovev, Gurjaspreet Singh. Advancements in Metal-Organic, Enzymatic, and Nanocomposite Platforms for Wireless Sensors of the Next Generation. *Advanced Functional Materials* **2024**, *15* https://doi.org/10.1002/adfm.202405231

27. Yang Zou, Zhou Li. Self-Powered Sensors for Wearable Detections. **2024**, 207-232. https://doi.org/10.1002/9783527841080.ch10
28. Qazi Muhammad Saqib, Abdul Mannan, Muhammad Noman, Mahesh Y. Chougale, Chandrashekhar S. Patil, Youngbin Ko, Jungmin Kim, Swapnil R. Patil, Muhammad Yousuf, Rayyan Ali Shaukat, Young Pyo Jeon, Deepak Dubal, Jinho Bae. Miniaturizing Power: Harnessing Micro-Supercapacitors for advanced micro-electronics. *Chemical Engineering Journal* **2024**, *490* , 151857. https://doi.org/10.1016/j.cej.2024.151857
29. Muhammad Adeel, Hong Seok Lee, Kanwal Asif, Sabrina Smith, Hasan Kurt, Flavio Rizzolio, Salvatore Daniele, Firat Güder. Micro-Supercapacitors for Self-Powered Biosensors. *Small Science* **2024**, *110* https://doi.org/10.1002/smsc.202400096
30. Suparna Das, Hirak Mazumdar, Kamil Reza Khondakar, Ajeet Kumar Kaushik, Yogendra Kumar Mishra. Quantum Biosensors: Principles and Applications in Medical Diagnostics. *ECS Sensors Plus* **2024**, https://doi.org/10.1149/2754-2726/ad47e2
31. Yao Chen, Xinhao Wan, Guanglei Li, Jianqi Ye, Jie Gao, Dan Wen. Metal Hydrogel-Based Integrated Wearable Biofuel Cell for Self-Powered Epidermal Sweat Biomarker Monitoring. *Advanced Functional Materials* **2024**, *22* https://doi.org/10.1002/adfm.202404329
32. Guang Yao, Xingyi Gan, Yuan Lin. Flexible self-powered bioelectronics enables personalized health management from diagnosis to therapy. *Science Bulletin* **2024**, *549* https://doi.org/10.1016/j.scib.2024.05.012
33. Zhengfei Wang, Bolin Li, Bin Liu, Jin-Woo Lee, Qingqing Bai, Wanli Yang, Junwei Wang, Jie Yang, Xiage Zhang, Huiliang Sun, Xi Yang, Bumjoon J. Kim, Xugang Guo. Facilely Modified Nickel-Based Hole Transporting Layers for Organic Solar Cells

with 19.12% Efficiency and Enhanced Stability. *Small* **2024**, *382* https://doi.org/10.1002/smll.202400915

34. Hongchun Luo, Tao Yang, Xingjian Jing, Yingxuan Cui, Weiyang Qin. Environmental energy harvesting boosts self-powered sensing. *Materials Today Energy* **2024**, *40* , 101502. https://doi.org/10.1016/j.mtener.2024.101502
35. Swarup Biswas, Sang Won Lee, Yongju Lee, Hyo-Jeong Choi, Jianjun Chen, Xiao Yang, Yuxuan Du, Natashya Falcone, Natan Roberto de Barros, Sung-Min Lee, Hyeok Kim, Ali Khademhosseini, Yangzhi Zhu. Emerging Energy Harvesters in Flexible Bioelectronics: From Wearable Devices to Biomedical Innovations. *Small Science* **2024**, *4* (3) https://doi.org/10.1002/smsc.202300148
36. P.N. Blessy Rebecca, D. Durgalakshmi, S. Balakumar, R. Ajay Rakkesh. Enhancing self-powered wearable device performance: ZIF-8/rGO hybrid nanostructures for extended operation and electrochemical glucose detection. *Chemical Engineering Journal* **2024**, *1* , 149789. https://doi.org/10.1016/j.cej.2024.149789
37. Mayank Garg, Arpana Parihar, Md. Saifur Rahman. Advanced and personalized healthcare through integrated wearable sensors (versatile). *Materials Advances* **2024**, *5* (2) , 432-452. https://doi.org/10.1039/D3MA00657C
38. Santosh Kumar Parupelli, Salil Desai. The 3D Printing of Nanocomposites for Wearable Biosensors: Recent Advances, Challenges, and Prospects. *Bioengineering* **2024**, *11* (1) , 32. https:doi.org/10.3390/bioengineering11010032
39. Ihor Sobianin, Sotiria D. Psoma, Antonios Tourlidakis. A 3D-Printed Piezoelectric Microdevice for Human Energy Harvesting for Wearable Biosensors. *Micromachines* **2024**, *15* (1) , 118. https://doi.org/10.3390/mi15010118

40. Kun Liao, Zhaochu Yang, Dong Tao, Libo Zhao, Nuno Pires, Carlos Alberto Dorao, Bjørn Torger Stokke, Lars Eric Roseng, Wen Liu, Zhuangde Jiang. Exploring the Intersection of Brain–Computer Interfaces and Quantum Sensing: A Review of Research Progress and Future Trends. *Advanced Quantum Technologies* **2024**, *7* (1) https://doi.org/10.1002/qute.202300185

Chapter 3

WEARABLE SENSOR DATA ANALYSIS

Materials from this chapter adapted from “Min, J.; Tu, J.; Xu, C.; Lukas, H.; Shin, S.; Yang, Y.; Solomon, S. A.; Mukasa, D.; Gao, W. Skin-Interfaced Wearable Sweat Sensors for Precision Medicine. Chemical Reviews 2023, 123 (8), 5049–5138. https://doi.org/10.1021/acs.chemrev.2c00823.”

Data processing is a critical aspect of wearable sweat sensors that enables the extraction of valuable health information from a wave of raw and unstructured sensor readouts. On the low level, data processing algorithms such as data smoothing, curve fitting, or peak detection enable the accurate calibration of biomarker concentrations from raw sensor data. On the higher level, these biomarker concentrations can be processed through learning algorithms to establish personalized baseline and cautionary biomarker levels, enabling personalized and preventative healthcare.

3.1. Multimodal Sensors

3.1.1. Multiplexed Data Acquisition

Given the success in the biosensor field, the natural next step is to integrate sensors onto wearable devices. By measuring multiple electrochemical or physical sensor readouts, one can potentially obtain an array of information ranging from skin temperature, heart rate, and blood pressure to more complex biochemical measurements used in the diagnosis of diseases like cancer or COVID.[3,4,9,12,13] To achieve this diagnostic power, wearable sweat sensors must be integrated with multiple sensing modalities. Simultaneous monitoring of ECG signals and sweat lactate concentrations have been reported, for example (**Figure 3-1a**).[5] ECG is well-known for its applications in cardiovascular health, while lactate can be used as an index of physical exhaustion. Coupling these two pieces of information into a single device gives health professionals both insight into tissue oxygenation from lactate and exertion from measured heart rates. Similarly, a laser-scribed sensor patch has been reported with the capability of measuring caffeine, uric acid, and glucose in sweat while accurately measuring heart rate and heart rate variation (**Figure 3-1b**).[14] More recently, work has been done to push multimodal devices to not only detect sweat biomarkers (alcohol) but also interstitial fluid biomarkers (glucose) in hopes of painting a more complete picture of a user's health (**Figure 3-1c**).[10] In addition to multiplex biomarker detection, vital sign sensing of blood pressure and heart rate has been successfully integrated with biochemical sensors including lactate, alcohol, glucose, and caffeine.[9] The device thoughtfully utilizes ultrasonic transducers for vital monitoring. Such transducers not only allow for that accurate measurement of these vitals, but were shown to exhibit minimal crosstalk with chemical sensors given an optimal operating distance away from these sensors. Further, the coupling of these sensors paints a picture of a user's health status by quantifying alcohol and caffeine consumption while also measuring exertion levels from vital sensors. As the field has progressed, multiple sensing modalities have been implemented in devices as to achieve cheaper and easier device implementation. While the previously mentioned devices have a high degree of accuracy, they all rely on electrochemical analysis for which compartments like potentiostats, batteries, or Bluetooth radios are costly. Further, when such bulky components are inflexible, they can limit the potential to miniaturize the wearable device. A thin, flexible colorimetric device has been reported with the capability of measuring pH, sweat rate, chloride, lactate, and glucose (**Figure 3-1d**).[7] By utilizing a biofuel cell-based sensor in conjunction with NFC-based sensor readout and wireless communication, the need for a battery was removed, rendering the device battery-free. Multiple sensing modalities have also opened doors for the classification of more complex biophysical states. Stress states have been predicted with a sweat-based wearable device by measuring multiple stressed-related biomarkers (**Figure 3-1e**).[8] By integrating a lateral flow immunoassay with fluorescence-based assays, simultaneous measurement of sweat cortisol and ascorbic acid levels is achieved. Cortisol, being well-known as the stress biomarker, can reveal an individual's stress levels while ascorbic acid (i.e., vitamin C) can correlate to immune response and potentially can be used in the treatment evaluation.

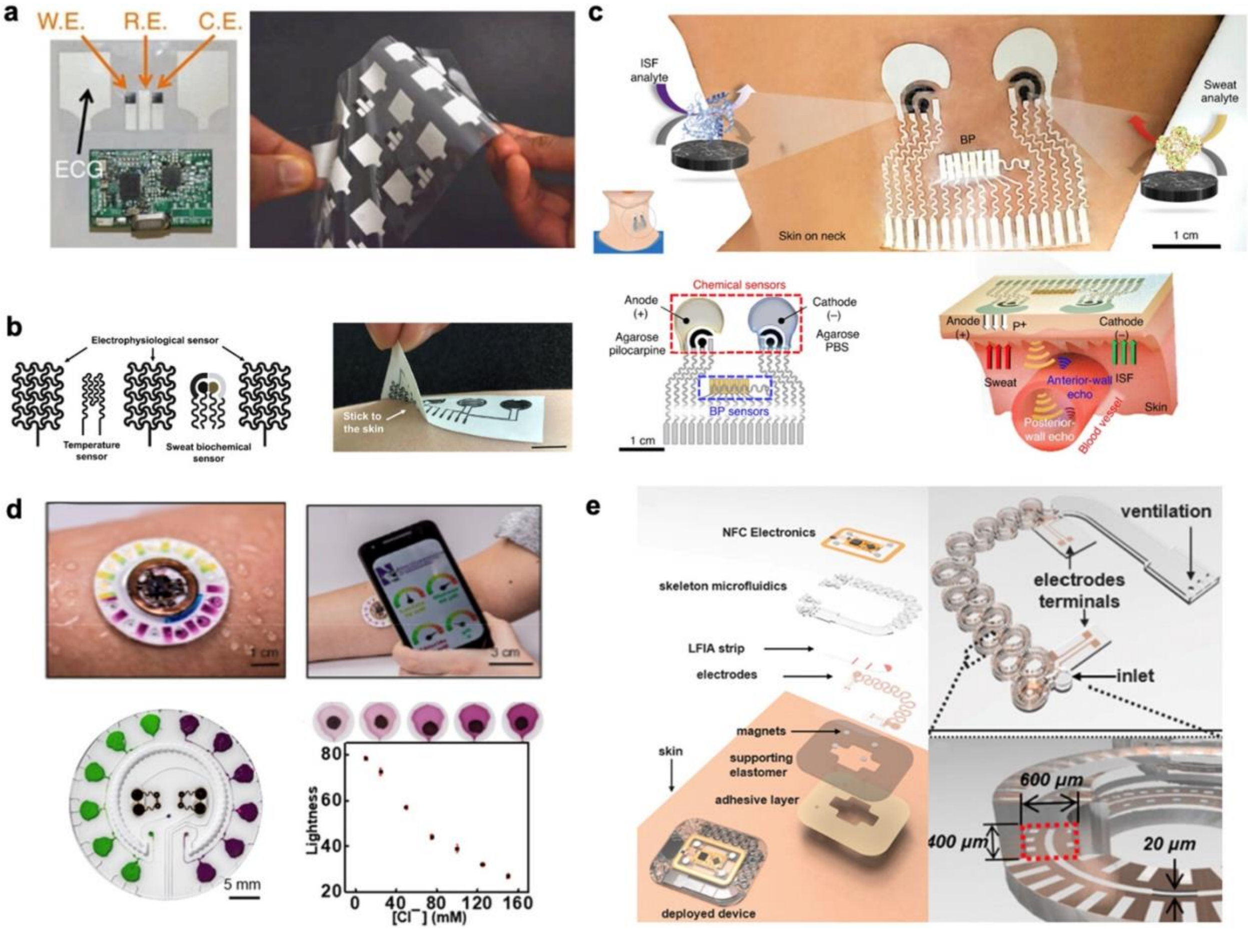

Figure 3-1: Multimodal data acquisition. **a**, Multimodal ECG and sweat lactate measuring device. Reproduced with permission from ref (5) under CC BY 4.0. Copyright 2016 Imani et al. **b**, Laser engraved biosensor with multiple sensing modalities and a high degree of flexibility. Scale bar, 1 cm. Reproduced with permission from ref (14). Copyright 2022 The American Association for the Advancement of Science. **c**, Wearable device with both sweat and ISF sensing capabilities. Reproduced with permission from ref (10) under CC BY 4.0. Copyright 2018 Wiley. **d**, Colorimetric wearable device with glucose and lactate sensors. Reproduced with permission from ref (7). Copyright 2019 The American Association for the Advancement of Science. **e**, Stress detecting wearable device integrated with lateral flow immunoassay. Reproduced with permission from ref (8) under CC BY 4.0. Copyright 2020 Proceedings of the National Academy of Sciences.

3.1.2. Sensor Crosstalk and Calibration

Another essential feature of multimodal sensors is their capability to self-calibrate other sensors on a wearable device, rendering the entire wearable system more accurate. Most of the aforementioned sensors, for example, rely on enzyme-based sensing, which can be influenced by operating temperatures.[1,15–17] On-skin temperature sensors could therefore serve a dual purpose to both measure skin temperature for diagnostic and calibrating sensor reading (**Figure 3-2a**).[2] This strategy was employed in a wearable sensor array for the continuous measurement of sweat glucose and lactate.[18] With the measured temperature and known temperature's influence on enzymatic sensor performance, glucose and lactate measurements can be calibrated. Similarly, a wearable system for the collection of exercise sweat to avoid hypoglycemic shock in diabetics has been reported.[19] Again, glucose measurements are normalized via temperature readouts showing the impact this method has on the wearable field. Resistive temperature sensors should, however, take into consideration the effect of strain-responsive change in resistance as shown in laser-engraved graphene sensors.[3]

Serpentine patterns could be adapted into temperature sensor designs to reduce the strain-induced change in resistance. Chemical sensors in particular face many challenges with interferences from the complex matrix in biofluids, including various coexisting biomarkers which may skew the quantitation of the target biomarker. Reports have shown that the ionic strength of sweat (i.e., Na+ concentrations) has the potential to influence a sensor's output signal (**Figure 3-2b**).[4,20] Moreover, as sweat rate could influence certain biomarker levels during exercises, sweat Na+ level (which showed a linear correlation with sweat rate) may be used to further calibrate sensors for continuous personalized monitoring. In addition, chemical measurements are susceptible to further signal drift depending on their chemical environment. For example, when NH4+ level interferes with urea sensor reading, quantitation of urea would require simultaneous measurement of NH4+ and real-time calibration (**Figure 3-2c**).[11] In addition to certain ions, pH could pose an influence on sweat chemical sensing. For example, glucose oxidase was shown to be affected by pH and requires pH calibration in real time (**Figure 3-2d**).[6] Multimodal physiochemical sensing systems are highly promising for realizing precision medicine. The collected vital sign or physical parameter data could be used for calibrating the chemical sensor readings. Moreover, such data could supplement the molecular information and provide a comprehensive picture of an individual's health state, which is a crucial step in realizing precision medicine.

3.2. Machine Learning-Based Data Analysis

Wearable devices, in particular sweat sensors, have the potential to generate a spectrum of medical data, with each recorded biomarker painting an incomplete picture about the health of the patient. Artificial intelligence (AI), specifically machine learning (ML), offers a way to organize this information in an interpretable or useful manner. In the literature, ML has been applied to synthesize on-body biochemical profiles to predict the presence of diseases,[21] mental disorders,[22] emotional states,[23] drug intake, and nutritional levels[24,25] only using analytes in the sweat. By optimizing the expected ML accuracy, one can further determine which chemicals hold predictive information,[26,27]

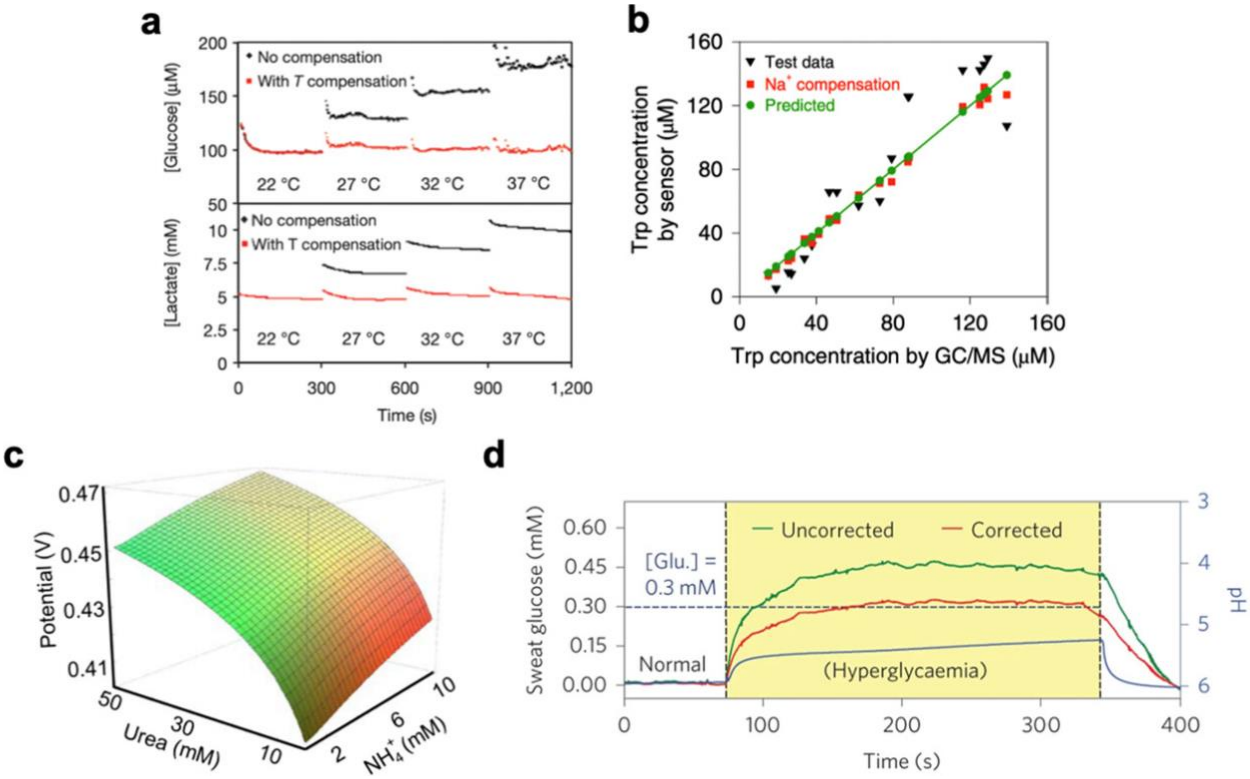

Figure 3-2: Figure 40. Sensor crosstalk and calibration. **a**, Influence of temperature on glucose and lactate sensors. Reproduced with permission from ref (2). Copyright 2016 Springer Nature. **b**, Influence of electrolyte (Na^+) level on tryptophan biosensor response. Reproduced with permission from ref (4). Copyright 2022 Springer Nature. **c**, Influence of ammonium (NH_4^+) on urea biosensors. Reproduced with permission from ref (11). Copyright 2020 The American Association for the Advancement of Science. **d**, Influence of pH on glucose biosensors. Reproduced with permission from ref (6). Copyright 2016 Springer Nature.

how to organize sensors on a patch,[28] as well as the optimal placement of sensors on the skin.[28] Each of these experiments can be broadly broken up into the following sections (**Figure 3-3a**): sensor design, on-body experiments, data processing, feature extraction, ML model selection, and updating experimental parameters.[29] So far, this review has discussed the process of sensor design, on-body experiments, and data processing. The following section will go into feature extraction, ML model selection, and updating experimental parameters. To achieve these goals, there are three general subcategories of ML algorithms one can utilize: supervised learning, unsupervised learning, and reinforcement learning. Unsupervised and reinforcement learning utilize unlabeled data (unmarked samples), requiring a large amount of data to make predictions. In a laboratory setting, this can be impractical for many emerging technologies still in the prototype stage that cannot generate a large quantity of high-quality data. Furthermore, these two methods are error-prone and can misinterpret ground truth for early experiments as the ML model is being refined. Because of these limitations, in this section, we will focus on supervised learning, the most common examples being convolutional neural networks (CNNs), support vector machines (SVMs), k-nearest neighbors (KNNs), logistical regression, and artificial neural networks.

3.2.1. Curse of Dimensionality

In machine learning, features refer to measurable properties or characteristics about an experiment. As there is no standard method to extract features, it is rather important to understand how features can broadly affect ML models. For supervised learning in wearable devices, each sweat analyte (such as uric acid) acts as an independent variable (feature) that potentially correlates with a quantifiable or observable event (e.g., gout). The more data one collects about a feature the more defined this association appears. From this point of view, a feature represents information added to a model. This leads many to believe that adding more information (features) to a model yields a better prediction. The following section will explore this idea further, highlighting the benefits and consequences of feature extraction. The main deterrent for extracting features is that each piece of information carries an additional degree of freedom when solving for the underlying trend. In plain words, when building a model, each feature is not considered in isolation, but is rather compared against all existing inputs. As shown in **Figure 3-3**, as the dimensionality (number of features) increases, the feature space grows exponentially. Practically, with 4 datapoints evenly sampled across 1 feature, one would require 16data points to achieve the same level of confidence in a 2-dimentional feature-space. For a fixed data set, this leads to a trade-off: adding more information to the model vs adding more uncertainty about the connections between this information. Unfortunately, there is no universal standard limit to the number of features one should use for a given number of points. This is because in practice most data cannot be controlled and evenly sampled across a feature; rather, one might see duplicates or clusters inside a feature dimension. In practice, this means that adding more features tends to initially increase the accuracy due to more information in the model; however, there exists a point when the accuracy will decrease with each new feature added. This occurs because in a small data set the model cannot extract meaningful trends from the feature-space. This phenomenon is referred to as the curse of dimensionality, also known as the peaking phenomenon or Hughes phenomenon. In plain terms, there exists a feature dimension where the average predictive power of any classifier degrades when increasing the feature space. Unfortunately, collecting data for novel sensors can often be arduous due to experimental error, time, as well as finding enough distinctive and representative subjects. Therefore, machine learning problems using wearable devices are often feature-limited by a small data set. If data is not limited, collecting more points will add certainty to the model's final prediction, leading to the alternative question: how much data is too much. Luckily, there is no upper limit to the amount of data one could collect, as more data creates more certainty in the analysis. Nonetheless, in practice, one finds that the initial points drastically change the model's accuracy until it reaches a steady state. To determine if enough data has been collected, it is best to withhold some samples from the model as a validation set or test set and check whether their input has a significant effect on the model's final performance. The best way to improve a model's accuracy, without adding more data, is to improve the feature extraction procedure, thereby reducing noise in the feature set. In machine learning, gathering clean, robust features from signals is preferred overutilizing extra, unnecessary information to make the same prediction

3.2.2. Feature Selection

To remove features from a model, one must select the combination of features with the most nonoverlapping and relevant information to the prediction. There are a variety of well-known algorithms to accomplish this goal. The simplest method is to brute force try each feature combination, selecting the set that performs the best. Brute-force feature selection is widely used in the literature and has been applied to determine biomarkers in brain–machine interfaces,[33] to detect COVID-19 from acoustic waves,[34] and to detect breast cancer from images. This is because for a static model brute force feature selection is guaranteed to yield an optimal solution across multiple training sessions; however, it is computationally and time intensive, making it unreasonable for selecting information from a large feature pool, a large data set, or on a complex model due to the training time. Fortunately, there are alternative feature selection algorithms that can handle these cases, the most popular choices being principal component analysis (PCA), linear discriminant analysis (LDA), and Shapley additive explanations (SHAP). In contrast to brute-force selection, LDA and PCA use a mathematical approach to eliminate features. PCA accomplishes this by transforming potentially correlated features into a basis set of orthogonal components using an eigenvalue decomposition. The final features are a linear combination of the original set. Like the brute-force method, PCA analysis can be used in similar situations to predict breast cancer,[35] categorize gene expression from different cell lines (**Figure 3-3b**),[30] and analyze COVID-19.[36] Furthermore, PCA analysis has been used to find sweat metabolite combinations that are indicative of lung cancer.[26,37] Meanwhile, LDA reduces the feature dimension by looking for a subspace of features that maximizes the separation between two classifications. Like PCA, LDA has also been commonly used to detect breast cancer biomarkers.[38,39] Given that both methods have been applied to similar problems, one might wonder when one algorithm is preferred. PCA analysis is an unsupervised algorithm, making it optimal when working with unlabeled data or when looking for patterns in the features. In contrast, LDA works well when classifying data into groups. When both algorithms can be applied, LDA works better when the feature space is noisy, as PCA analysis will not overlook noise when creating a basis set in the feature space. Recently, SHAP has become another popular feature selection tool. The SHAP analysis utilizes a game theory approach to explain an individual feature's contribution to the final prediction.[40] The SHAP value of feature A is calculated by taking the difference between the model's output with feature A and the average output after iterating through the feature-space of A.[40] SHAP values can be applied to discrete features for the detection of drugs in sweat[41] as well as in images to find important structural features for the activity prediction of chemicals[27] (**Figure 3-3c**). Despite providing greater insight into each feature, one drawback to the SHAP analysis is how computationally expensive the analysis is for many features due to training the model across the entire feature's dimension. There are many other feature selection algorithms not discussed in this section such as local interpretable model-agnostic explanations (LIME),[42] single feature importance (SFI), and mean decrease accuracy (MDA). Some researchers have found that utilizing an aggregation of feature extraction techniques can improve the search for optimal feature combinations. Using an ensemble of feature selection methods will correct for any biases in one algorithm. The ensemble approach has been used in discovering important metabolites in a mouse's liver.[43] More research into ensemble feature selection methods will mitigate the problem of missing important features and aid in creating a more robust biomarker discovery tool; however, the biggest limitation of this technique is the computational time required for large feature pools

3.2.3. Model Selection

There are a variety of machine learning models presented in the literature, each with broad, overlapping applications in the wearable space, which often make it hard to select the optimal algorithm to use. For quantifying chemicals in sweat, CNNs can measure lactate with an F1 score of 0.990,[24] decision trees can measure glucose with a root mean squared of 0.1 mg/dL,[44] KNNs can improve drifting errors in cortisol detection,[45] and KNNs can measure tyrosine and uric acid (**Figure 3-3**d).[31] On-body sensors have diagnosed depression from a random forest algorithm,[32] emotional states from support vector machines,[23,46] and stress from logistical regression.[47] From measuring chemicals in the sweat to psychological states, the use of different ML algorithms for similar problems highlights an important question: does the specific ML architecture matter when most algorithms are interchangeable while still maintaining ahigh accuracy. The simple answer is that ML models do not create the final trends in the input variables; rather, ML is a tool that connects information from the input-space to an observable output, if such a connection exists. As a tool, models can achieve the same results while taking different paths. In this regard, the choice of model often depends on situational parameters such as time/computational efficiency, interpretability, and reproducibility. In terms of efficiency, the rate limiting factor in the training time is model complexity. The benefit of complex neural architectures is that they have greater flexibility to adapt to any subtleties present in the feature space. This makes them extremely good at finding weak trends within the data, such as identifying ethnicity and age from sweat lipid profiles using a gradient boosting tree ensemble.[48] Unfortunately, complex models also require more data for training and risk overfitting noisy sensors. Furthermore, if the model is too complex, it becomes hard to create an interpretable mathematical expression relating the feature space to the final output. Using a complex 7-convolution layer CNN, a wearable device was able to monitor Parkinson’s disease.[49] In this complex case, machine learning demonstrates the relevance of input features, but not why they are relevant. This makes it hard to reproduce and validate the outcome, due to small differences in the input space (i.e., electrodes, subjects, and sensing technique) as well as possible randomness inherent in the algorithm. A common example of poor interpretability, yet widely applicable, is deep learning networks, which have previously been used to surpass the limit of detection of six different metal ions in sweat.[50] Model selection is a trade-off between simple architectures and high accuracy; however, it has underlying dependence on whether the model is meant to be interpretable, easily reproducible, and efficient.

3.2.4. Machine Learning Inspired Designs

After selecting a model, one can further extend the analysis to update experimental parameters. This is achieved by monitoring a model's accuracy change while varying different experimental attributes. Through this technique, one can find a combination of optimal antigen sensors to diagnose Lymedisease,[28] find the best placement of electrodes on the skin,[28] as well as optimize the material, structural, and excitation characteristics of gas sensors.[51] Upon finding an optimal configuration, one must recollect new data, extract features, and retrain the model (**Figure 3-3e**).[32] This process can be repeated multiple times, performing a gradient-descent search as one refines the final experimental parameters. When performed on a single subject, this method can aid in the development of a more personalized device for the patient.

3.2.5. Machine Learning Discussions

Machine learning can be applied to the development of physiochemical sensors, personalized healthcare, and biomarker discovery.[51] When developing machine learning models for wearable devices, there are a variety of factors to consider from input features to model architecture. Adding robust, nonoverlapping information is the best way to increase the accuracy of a model; however, selecting these features can often be challenging as different feature selection algorithms may favor specific combinations. Feature selection is further limited by the choice of model. When constructing a machine learning model, simple architectures with a small subset of features provide greater insight into the underlying mechanisms of how the feature-space maps the health of the patient. Therefore, while itis attractive to work on complex designs with many features, limiting the scope of the analysis can afford a deeper understanding of how each feature pairing affects the final diagnosis and health of the patient. The application of machine learning in wearable sweat biosensors is still a budding field. It is well-known in the machine learning community that features can greatly impact the final accuracy.

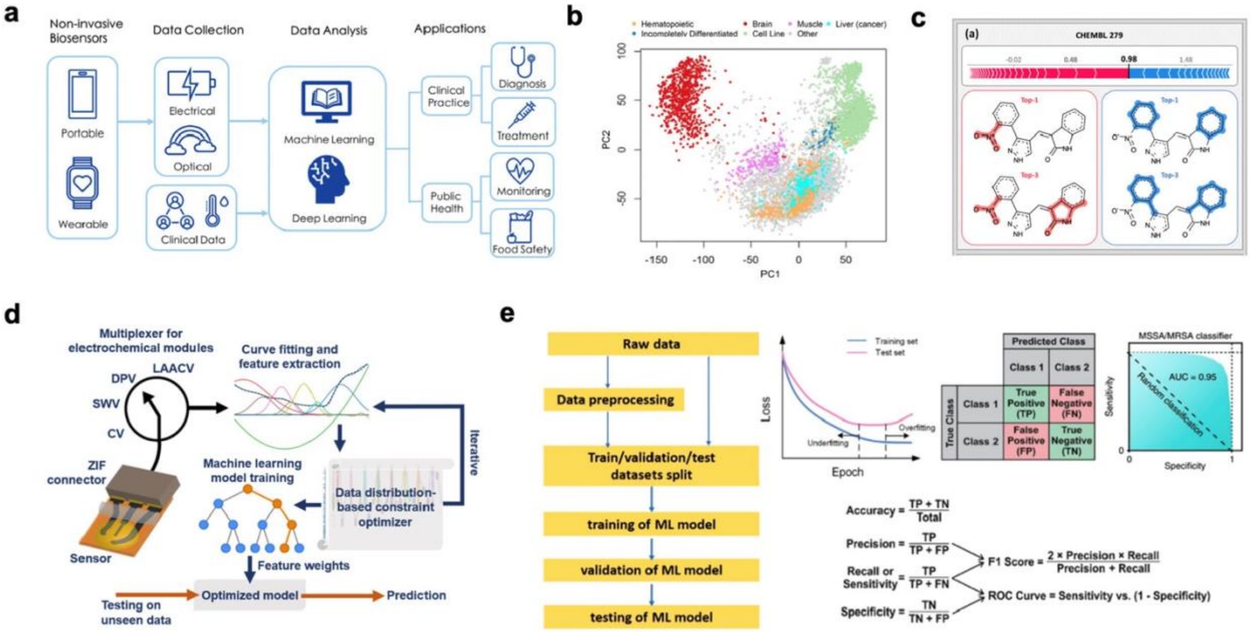

Figure 3-3: Data processing and machine learning. **a**, Broad overview of the machine learning experimental pipeline from biosensor fabrication to industry application. Reproduced with permission from ref (617). Copyright 2021 Wiley. **b**, Principal component analysis (PCA) analysis that can categorize different cell lines based on gene expression. Reproduced with permission from ref (618) under CC BY 4.0. Copyright 2016 Lenz et al. **c**, Shapley additive explanations (SHAP) analysis of two kinase inhibitors, displaying functional groups that help (red) or hurt (blue) its potency. Reproduced with permission from ref (615) under CC BY 4.0. Copyright 2020 Rodríguez-Pérez et al. **d**, Flowchart for extracting features from electrochemical measurements, training a model, and predicting analyte concentrations. Reproduced with permission from ref (619). Copyright 2022 Elsevier. **e**, Generic training process for a neural network. Reproduced with permission from ref (620). Copyright 2020 American Chemical Society.

Further investigations should look into biochemical features that can be extracted from wearable devices, especially considering the accuracy improvements that have already been seen in multimodal wearable devices when one considers the impacts of sweat rate, ionic strength, pH, and skin temperature. There is great potential for a device which measures these signals to improve the accuracy, as well as the sensitivity or selectivity, of coexisting chemical sensors. Another significant problem affecting the accuracy is noise in the form of motion artifact. Removing these artifacts to enable a system to measure the underlying signal could be of particularly high impact and help push wearable devices to the market.

BIBLIOGRAPHY

1. Bariya, M.; Nyein, H. Y. Y.; Javey, A. Wearable Sweat Sensors. *Nat. Electron.* **2018**, *1*, 160– 171, DOI: 10.1038/s41928-018-0043-y
2. Gao, W.; Emaminejad, S.; Nyein, H. Y. Y.; Challa, S.; Chen, K.; Peck, A.; Fahad, H. M.; Ota, H.; Shiraki, H.; Kiriya, D.; Lien, D.-H.; Brooks, G. A.; Davis, R. W.; Javey, A. Fully Integrated Wearable Sensor Arrays for Multiplexed *in Situ* Perspiration Analysis. *Nature* **2016**, *529*, 509– 514, DOI: 10.1038/nature16521
3. Yang, Y.; Song, Y.; Bo, X.; Min, J.; Pak, O. S.; Zhu, L.; Wang, M.; Tu, J.; Kogan, A.; Zhang, H.; Hsiai, T. K.; Li, Z.; Gao, W. A Laser-Engraved Wearable Sensor for Sensitive Detection of Uric Acid and Tyrosine in Sweat. *Nat. Biotechnol.* **2020**, *38*, 217– 224, DOI: 10.1038/s41587-019-0321-x
4. Wang, M.; Yang, Y.; Min, J.; Song, Y.; Tu, J.; Mukasa, D.; Ye, C.; Xu, C.; Heflin, N.; McCune, J. S.; Hsiai, T. K.; Li, Z.; Gao, W. A Wearable Electrochemical Biosensor for the Monitoring of Metabolites and Nutrients. *Nat. Biomed. Eng.* **2022**, *6*, 1225– 1235, DOI: 10.1038/s41551-022-00916-z
5. Imani, S.; Bandodkar, A. J.; Mohan, A. M. V.; Kumar, R.; Yu, S.; Wang, J.; Mercier, P. P. A Wearable Chemical-Electrophysiological Hybrid Biosensing System for Real-Time Health and Fitness Monitoring. *Nat. Commun.* **2016**, *7*, 11650, DOI: 10.1038/ncomms11650
6. Lee, H.; Choi, T. K.; Lee, Y. B.; Cho, H. R.; Ghaffari, R.; Wang, L.; Choi, H. J.; Chung, T. D.; Lu, N.; Hyeon, T.; Choi, S. H.; Kim, D.-H. A Graphene-Based Electrochemical Device with Thermoresponsive Microneedles for Diabetes Monitoring and Therapy. *Nat. Nanotechnol.* **2016**, *11*, 566– 572, DOI: 10.1038/nnano.2016.38

7. Bandodkar, A. J.; Gutruf, P.; Choi, J.; Lee, K.; Sekine, Y.; Reeder, J. T.; Jeang, W. J.; Aranyosi, A. J.; Lee, S. P.; Model, J. B.; Ghaffari, R.; Su, C.-J.; Leshock, J. P.; Ray, T.; Verrillo, A.; Thomas, K.; Krishnamurthi, V.; Han, S.; Kim, J.; Krishnan, S.; Hang, T.; Rogers, J. A. Battery-Free, Skin-Interfaced Microfluidic/Electronic Systems for Simultaneous Electrochemical, Colorimetric, and Volumetric Analysis of Sweat. *Sci. Adv.* **2019**, *5*, eaav3294 DOI: 10.1126/sciadv.aav3294
8. Kim, S.; Lee, B.; Reeder, J. T.; Seo, S. H.; Lee, S.-U.; Hourlier-Fargette, A.; Shin, J.; Sekine, Y.; Jeong, H.; Oh, Y. S.; Aranyosi, A. J.; Lee, S. P.; Model, J. B.; Lee, G.; Seo, M.-H.; Kwak, S. S.; Jo, S.; Park, G.; Han, S.; Park, I.; Jung, H.-I.; Ghaffari, R.; Koo, J.; Braun, P. V.; Rogers, J. A. Soft, Skin-Interfaced Microfluidic Systems with Integrated Immunoassays, Fluorometric Sensors, and Impedance Measurement Capabilities. *Proc. Natl. Acad. Sci. U. S. A.* **2020**, *117*, 27906– 27915, DOI: 10.1073/pnas.2012700117
9. Sempionatto, J. R.; Lin, M.; Yin, L.; De la paz, E.; Pei, K.; Sonsa-ard, T.; de Loyola Silva, A. N.; Khorshed, A. A.; Zhang, F.; Tostado, N.; Xu, S.; Wang, J. An Epidermal Patch for the Simultaneous Monitoring of Haemodynamic and Metabolic Biomarkers. *Nat. Biomed. Eng.* **2021**, *5*, 737– 748, DOI: 10.1038/s41551-021-00685-1
10. Kim, J.; Sempionatto, J. R.; Imani, S.; Hartel, M. C.; Barfidokht, A.; Tang, G.; Campbell, A. S.; Mercier, P. P.; Wang, J. Simultaneous Monitoring of Sweat and Interstitial Fluid Using a Single Wearable Biosensor Platform. *Adv. Sci.* **2018**, *5*, 1800880, DOI: 10.1002/advs.201800880
11. Yu, Y.; Nassar, J.; Xu, C.; Min, J.; Yang, Y.; Dai, A.; Doshi, R.; Huang, A.; Song, Y.; Gehlhar, R.; Ames, A. D.; Gao, W. Biofuel-Powered Soft Electronic Skin with Multiplexed and Wireless Sensing for Human-Machine Interfaces. *Sci. Robot.* **2020**, *5*, eaaz7946 DOI: 10.1126/scirobotics.aaz7946
12. Torrente-Rodríguez, R. M.; Lukas, H.; Tu, J.; Min, J.; Yang, Y.; Xu, C.; Rossiter, H. B.; Gao, W. SARS-CoV-2 RapidPlex: A Graphene-Based Multiplexed Telemedicine Platform for Rapid

and Low-Cost COVID-19 Diagnosis and Monitoring. *Matter* **2020**, *3*, 1981– 1998, DOI: 10.1016/j.matt.2020.09.027

13. Lukas, H.; Xu, C.; Yu, Y.; Gao, W. Emerging Telemedicine Tools for Remote COVID-19 Diagnosis, Monitoring, and Management. *ACS Nano* **2020**, *14*, 16180– 16193, DOI: 10.1021/acsnano.0c08494
14. Zhao, G.; Ling, Y.; Su, Y.; Chen, Z.; Mathai, C. J.; Emeje, O.; Brown, A.; Alla, D. R.; Huang, J.; Kim, C.; Chen, Q.; He, X.; Stalla, D.; Xu, Y.; Chen, Z.; Chen, P.-Y.; Gangopadhyay, S.; Xie, J.; Yan, Z. Laser-Scribed Conductive, Photoactive Transition Metal Oxide on Soft Elastomers for Janus on-Skin Electronics and Soft Actuators. *Sci. Adv.* **2022**, *8*, eabp9734 DOI: 10.1126/sciadv.abp9734
15. Prieto, M. A.; Vazquez, J. A.; Murado, M. A. A New and General Model to Describe, Characterize, Quantify and Classify the Interactive Effects of Temperature and pH on the Activity of Enzymes. *Analyst* **2015**, *140*, 3587– 3602, DOI: 10.1039/C4AN02136C
16. Wiorek, A.; Parrilla, M.; Cuartero, M.; Crespo, G. A. Epidermal Patch with Glucose Biosensor: pH and Temperature Correction toward More Accurate Sweat Analysis during Sport Practice. *Anal. Chem.* **2020**, *92*, 10153– 10161, DOI: 10.1021/acs.analchem.0c02211
17. Jobst, G.; Moser, I.; Varahram, M.; Svasek, P.; Aschauer, E.; Trajanoski, Z.; Wach, P.; Kotanko, P.; Skrabal, F.; Urban, G. Thin-Film Microbiosensors for Glucose-Lactate Monitoring. *Anal. Chem.* **1996**, *68*, 3173– 3179, DOI: 10.1021/ac950630x
18. Yokus, M. A.; Songkakul, T.; Pozdin, V. A.; Bozkurt, A.; Daniele, M. A. Wearable Multiplexed Biosensor System toward Continuous Monitoring of Metabolites. *Biosens. Bioelectron.* **2020**, *153*, 112038, DOI: 10.1016/j.bios.2020.112038
19. **607** Hong, Y. J.; Lee, H.; Kim, J.; Lee, M.; Choi, H. J.; Hyeon, T.; Kim, D. H. Multifunctional Wearable System that Integrates Sweat-Based Sensing and Vital-Sign Monitoring to Estimate Pre-

/Post-Exercise Glucose Levels. *Adv. Funct. Mater.* **2018**, *28*, 1805754, DOI: 10.1002/adfm.201805754

20. Pei, X.; Sun, M.; Wang, J.; Bai, J.; Bo, X.; Zhou, M. A Bifunctional Fully Integrated Wearable Tracker for Epidermal Sweat and Wound Exudate Multiple Biomarkers Monitoring. *Small* **2022**, *18*, 2205061, DOI: 10.1002/smll.202205061
21. Zhou, Z.; Alvarez, D.; Milla, C.; Zare, R. N. Proof of Concept for Identifying Cystic Fibrosis from Perspiration Samples. *Proc. Natl. Acad. Sci. U.S.A.* **2019**, *116*, 24408– 24412, DOI: 10.1073/pnas.1909630116
22. Kumar, S.; Chong, I. Correlation Analysis to Identify the Effective Data in Machine Learning: Prediction of Depressive Disorder and Emotion States. *Int. J. Environ. Res. Public Health* **2018**, *15*, 2907, DOI: 10.3390/ijerph15122907
23. Sharma, K.; Castellini, C.; van den Broek, E. L.; Albu-Schaeffer, A.; Schwenker, F. A Dataset of Continuous Affect Annotations and Physiological Signals for Emotion Analysis. *Sci. Data* **2019**, *6*, 196, DOI: 10.1038/s41597-019-0209-0
24. Yüzer, E.; Doğan, V.; Kılıç, V.; Şen, M. Smartphone Embedded Deep Learning Approach for Highly Accurate and Automated Colorimetric Lactate Analysis in Sweat. *Sens. Actuators B Chem.* **2022**, *371*, 132489, DOI: 10.1016/j.snb.2022.132489
25. Monge, J.; Postolache, O.; Plopa, O.; Trandabat, A.; Schreiner, O.; Schreiner, T. Glucose Detection in Sweat Using Biosensors. *IEEE E-Health Bioengineering Conference* , 2019, DOI: 10.1109/EHB47216.2019.8970023 .
26. Delgado-Povedano, M. del M.; Calderón-Santiago, M.; Priego-Capote, F.; Jurado-Gámez, B.; Luque de Castro, M. D. Recent Advances in Human Sweat Metabolomics for Lung Cancer Screening. *Metabolomics* **2016**, *12*, 166, DOI: 10.1007/s11306-016-1116-4

27. Rodríguez-Pérez, R.; Bajorath, J. Interpretation of Machine Learning Models Using Shapley Values: Application to Compound Potency and Multi-Target Activity Predictions. *J. Comput. Aided Mol. Des.* **2020**, *34*, 1013–1026, DOI: 10.1007/s10822-020-00314-0
28. Ballard, Z.; Brown, C.; Madni, A. M.; Ozcan, A. Machine Learning and Computation-Enabled Intelligent Sensor Design. *Nat. Mach. Intell.* **2021**, *3*, 556– 565, DOI: 10.1038/s42256-021-00360-9
29. Zhang, K.; Wang, J.; Liu, T.; Luo, Y.; Loh, X. J.; Chen, X. Machine Learning-Reinforced Noninvasive Biosensors for Healthcare. *Adv. Healthcare Mater.* **2021**, *10*, 2100734, DOI: 10.1002/adhm.202100734
30. Lenz, M.; Müller, F.-J.; Zenke, M.; Schuppert, A. Principal Components Analysis and the Reported Low Intrinsic Dimensionality of Gene Expression Microarray Data. *Sci. Rep.* **2016**, *6*, 25696, DOI: 10.1038/srep25696
31. Kammarchedu, V.; Butler, D.; Ebrahimi, A. A Machine Learning-Based Multimodal Electrochemical Analytical Device Based on EMoSx-LIG for Multiplexed Detection of Tyrosine and Uric Acid in Sweat and Saliva. *Anal. Chim. Acta* **2022**, *1232*, 340447, DOI: 10.1016/j.aca.2022.340447
32. Cui, F.; Yue, Y.; Zhang, Y.; Zhang, Z.; Zhou, H. S. Advancing Biosensors with Machine Learning. *ACS Sens.* **2020**, *5*, 3346– 3364, DOI: 10.1021/acssensors.0c01424
33. Mend, M.; Kullmann, W. H. Human Computer Interface with Online Brute Force Feature Selection. *Biomed. Technol. (Berl)* **2012**, *57*, 659– 662, DOI: 10.1515/bmt-2012-4082
34. Stasak, B.; Huang, Z.; Razavi, S.; Joachim, D.; Epps, J. Automatic Detection of COVID-19 Based on Short-Duration Acoustic Smartphone Speech Analysis. *J. Healthc. Inform. Res.* **2021**, *5*, 201– 217, DOI: 10.1007/s41666-020-00090-4

35. Hasan, H.; Tahir, N. M. Feature Selection of Breast Cancer Based on Principal Component Analysis. *IEEE Int. Conf. Signal Image Processing Appl.* **2010**, 242– 245, DOI: 10.1109/CSPA.2010.5545298

36. Fujisawa, K.; Shimo, M.; Taguchi, Y.-H.; Ikematsu, S.; Miyata, R. PCA-Based Unsupervised Feature Extraction for Gene Expression Analysis of COVID-19 Patients. *Sci. Rep.* **2021**, *11*, 17351, DOI: 10.1038/s41598-021-95698-w

37. Calderón-Santiago, M.; Priego-Capote, F.; Turck, N.; Robin, X.; Jurado-Gámez, B.; Sanchez, J. C.; Luque de Castro, M. D. Human Sweat Metabolomics for Lung Cancer Screening. *Anal. Bioanal. Chem.* **2015**, *407*, 5381– 5392, DOI: 10.1007/s00216-015-8700-8

38. Chan, H.-P.; Wei, D.; Helvie, M. A.; Sahiner, B.; Adler, D. D.; Goodsitt, M. M.; Petrick, N. Computer-Aided Classification of Mammographic Masses and Normal Tissue: Linear Discriminant Analysis in Texture Feature Space. *Phys. Med. Biol.* **1995**, *40*, 857– 876, DOI: 10.1088/0031-9155/40/5/010

39. Suhail, Z.; Denton, E. R. E.; Zwiggelaar, R. Classification of Micro-Calcification in Mammograms Using Scalable Linear Fisher Discriminant Analysis. *Med. Biol. Eng. Comput.* **2018**, *56*, 1475– 1485, DOI: 10.1007/s11517-017-1774-z

40. Lundberg, S. M.; Lee, S.-I. A Unified Approach to Interpreting Model Predictions. *Proceedings of the 31st International Conference on Neural Information Processing Systems* 2017; pp 4768– 4777.

41. Bittremieux, W.; Advani, R. S.; Jarmusch, A. K.; Aguirre, S.; Lu, A.; Dorrestein, P. C.; Tsunoda, S. M. Physicochemical Properties Determining Drug Detection in Skin. *Clinical Translational Sci.* **2022**, *15*, 761– 770, DOI: 10.1111/cts.13198

42. Ribeiro, M. T.; Singh, S.; Guestrin, C. Why Should I Trust You?": Explaining the Predictions of Any Classifier. *arXiv:1602.04938* **2016**. DOI: 10.48550/arXiv.1602.04938 .

43. Shahrjooihaghighi, A.; Frigui, H.; Zhang, X.; Wei, X.; Shi, B.; Trabelsi, A. An Ensemble Feature Selection Method for Biomarker Discovery. *IEEE Int. Conf. Signal Process. Comput. Control* **2017**, 416– 421

44. Sankhala, D.; Sardesai, A. U.; Pali, M.; Lin, K.-C.; Jagannath, B.; Muthukumar, S.; Prasad, S. A Machine Learning-Based on-Demand Sweat Glucose Reporting Platform. *Sci. Rep.* **2022**, *12*, 2442, DOI: 10.1038/s41598-022-06434-x

45. Shahub, S.; Upasham, S.; Ganguly, A.; Prasad, S. Machine Learning Guided Electrochemical Sensor for Passive Sweat Cortisol Detection. *Sens. Bio-Sens. Res.* **2022**, *38*, 100527, DOI: 10.1016/j.sbsr.2022.100527

46. Ayata, D.; Yaslan, Y.; Kamasak, M. Emotion recognition via galvanic skin response: Comparison of machine learning algorithms and feature extraction methods. *IU-J. Electr. Electron. Eng.* **2017**, *17*, 3129– 3136

47. Pandey, P. S. Machine Learning and IoT for Prediction and Detection of Stress. *International Conference on Computational Science and Its Applications* , 2017. DOI: 10.1109/ICCSA.2017.8000018 .

48. Zhou, Z.; Zare, R. N. Personal Information from Latent Fingerprints Using Desorption Electrospray Ionization Mass Spectrometry and Machine Learning. *Anal. Chem.* **2017**, *89*, 1369– 1372, DOI: 10.1021/acs.analchem.6b04498

49. Um, T. T.; Pfister, F. M. J.; Pichler, D.; Endo, S.; Lang, M.; Hirche, S.; Fietzek, U.; Kulić, D. Data Augmentation of Wearable Sensor Data for Parkinson’s Disease Monitoring Using Convolutional Neural Networks. *Proceedings of the 19th ACM International Conference on Multimodal Interaction*; Association for Computing Machinery: New York, NY, 2017; pp 216– 220.

50. Cho, S.-Y.; Lee, Y.; Lee, S.; Kang, H.; Kim, J.; Choi, J.; Ryu, J.; Joo, H.; Jung, H.-T.; Kim, J. Finding Hidden Signals in Chemical Sensors Using Deep Learning. *Anal. Chem.* **2020**, *92*, 6529– 6537, DOI: 10.1021/acs.analchem.0c00137

51. Potyrailo, R. A.; Brewer, J.; Cheng, B.; Carpenter, M. A.; Houlihan, N.; Kolmakov, A. Bio-Inspired Gas Sensing: Boosting Performance with Sensor Optimization Guided by “Machine Learning.. *Faraday Discuss.* **2020**, *223*, 161– 182, DOI: 10.1039/D0FD00035C

Chapter 4

QUANTUMDOCK: COMPUTATIONAL DESIGN OF NUTRIONAL SENSORS

Materials from this chapter adapted from “Mukasa, D.; Wang, M.; Min, J.; Yang, Y.; Solomon, S. A.; Han, H.; Ye, C.; Gao, W. A Computationally Assisted Approach for Designing Wearable Biosensors toward Non-Invasive Personalized Molecular Analysis. Advanced Materials 2023, 35 (35), 2370246. https://doi.org/10.1002/adma.202212161”

4.1: Introduction

Wearable sensors have great potential to revolutionize the field of personalized medicine as they can continuously and non-invasively monitor an individual's physiological and health status.[1-9] While commercially available wearable health monitors mainly track physical vital signs, wearable sweat biosensors could offer rich health information at molecular levels.[10-23] Continuous analysis of sweat biomarkers including amino acids, vitamins, metabolites, drugs, hormones, and proteins could have a profound impact in remote monitoring and management of a variety of health conditions such as stress, gout, metabolic disorders, cardiovascular diseases, and cancers.[24-40, 21] Most currently reported wearable electrochemical sweat biosensors can only monitor a limited group of small molecules (e.g., glucose, lactate, and ions) using enzymatic or ion-selective sensors.[24-30] The majority of clinically relevant biomarkers in sweat cannot be detected in situ using these wearable sensing approaches. Bioaffinity sensors based on bioreceptors such as antibodies can be highly sensitive and selective, but are limited to single-point use and usually require additional sample preparation or washing steps.[41-44]

Molecularly imprinted polymers (MIPs) are synthetic bioreceptors fabricated via the polymerization of functional monomers in the presence of the target analyte.[45, 46] Subsequent elution of the template molecule from the polymer matrix leaves target analyte-shaped imprints that can act as artificial antibodies to facilitate selective target rebinding. The integration of an additional redox probe in the sensor design can transduce such rebinding recognition into measurable electrochemical signals.[35, 47] We recently demonstrated continuous monitoring of circulating metabolites and nutrients such as branched-chain amino acids in human sweat by combining MIPs with mass-producible laser-engraved graphene (LEG).[35] Despite the great promise of using MIPs in wearable sweat biosensing, MIPs have not yet gained widespread use in the field of biosensors due to their complex design and optimization process.[48] The choice of functional monomers and cross-linkers dramatically influences sensor selectivity and overall performance, rendering many MIPs ineffective for biofluid analysis due to the lack of selectivity. Considering the large library of monomer and target biomarker choices, experimental optimization of new MIPs is extremely time-consuming, costly, and substantially impedes the broad application of MIP-based wearable sensor in personalized healthcare.

Computational approaches such as semiempirical calculations and density functional theory (DFT) have great potential to simplify and accelerate the MIP design process. Although fast, semiempirical methods utilize the neglect of diatomic differential overlap approximation which is known to significantly underestimate binding affinities, limiting the ability to correlate to experimental results. DFT enables researchers to utilize highly accurate quantum mechanics simulations to probe molecular interactions between a potential monomer and biomarker. Traditionally DFT has been used to calculate binding energies between monomers and target biomolecules, since maximizing this quantity maximizes the amount of target molecules to be absorbed which in return maximizes MIP sensitivity.[49-51] However, finding the most stable binding configuration between two biomolecules tends to be a time intensive task, further slowing down the MIP design process. Further, previous studies lack experimental validation for biomarker analysis and have not fully addressed the fundamentally limiting factor in MIP performance for in situ wearable sensing applications – selectivity.

In this work, we introduce QuantumDock, an automated computational framework for universal MIP development toward a wide range of wearable biosensing applications (**Figure 4-11a**). QuantumDock utilizes quantum theory, specifically DFT, to probe molecular interactions between monomers and the target/interference molecules. QuantumDock employs a novel theory to optimize selectivity: A molecular docking approach is employed to find the most stable binding geometries and to calculate a novel selectivity metric for the optimal choice of monomer (and cross-linker when necessary), enabling accelerated MIP fabrication (**Figure 4-11b–g**; **Figure A1**, **Appendix A**). Through these innovations, QuantumDock addresses all previously discussed shortcomings of semiempirical calculations and traditional DFT and is the first standardized method for calculating binding energies reproducibly with a modern level of theory (**Table A1**, **Appendix A**). In addition to optimizing the choice of existing monomers, QuantumDock also has the potential to explore various unknown monomers/molecules for general MIP design with potentially higher selectivities than traditionally used monomers. Using an essential amino acid phenylalanine (Phe) as the exemplar, we experimentally validated the model using solution-synthesized MIP nanoparticles (NPs) and demonstrated for the first time – the correct prediction of the exponential relation between binding energy difference and selectivity in MIPs. This is particularly important for wearable sensor field as for practical in situ body fluid analysis, selectivity is the main limiting factors of the MIP design. Moreover, we designed a skin-interfaced wearable sweat sensing system and demonstrated the potential usage of a QuantumDock-optimized MIP wearable sensor for personalized nutritional and healthcare applications (**Figure 4-11h,i**).

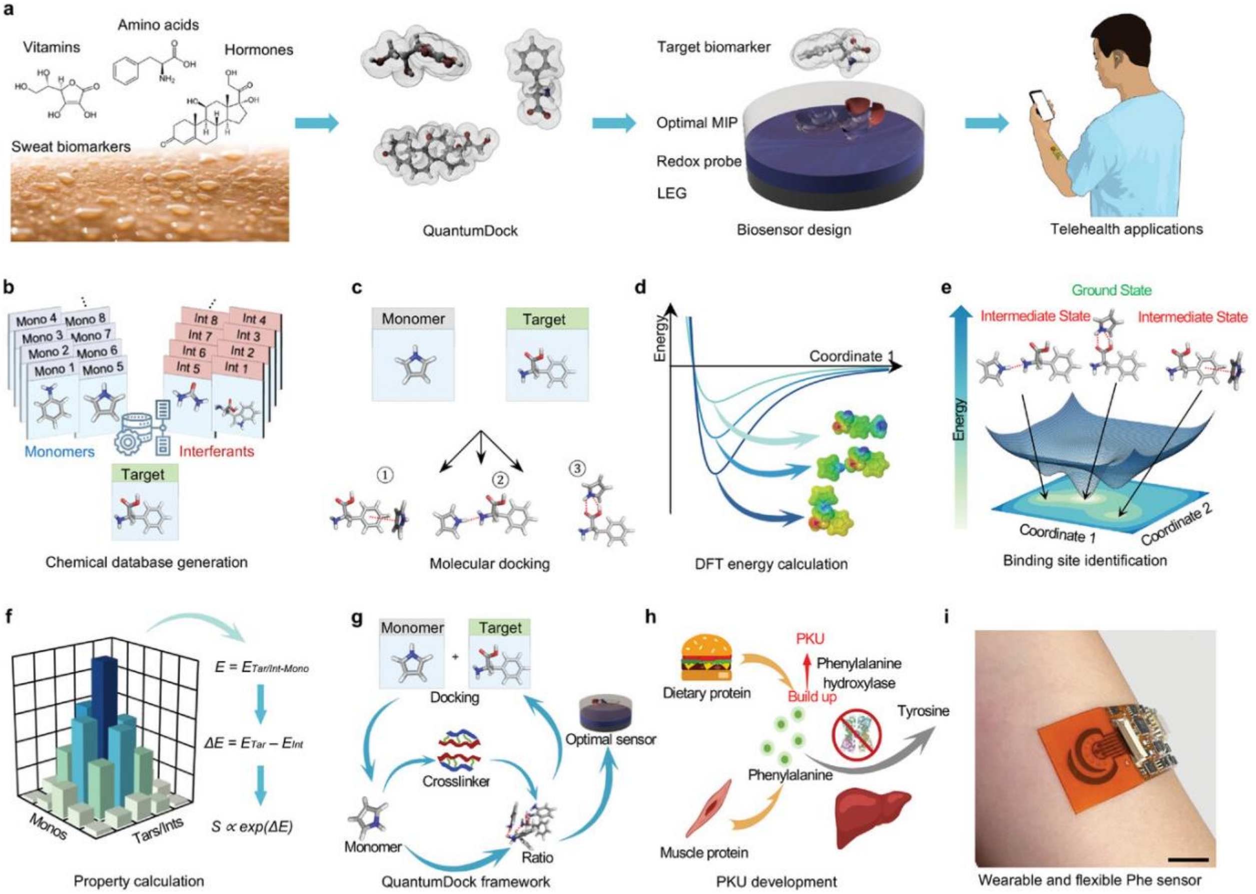

Figure 4-11: QuantumDock, a rational bioaffinity biosensor design approach for wearable molecular monitoring. a) QuantumDock-enabled molecularly imprinted polymer (MIP)-based wearable biosensor design and optimization for circulating biomarker monitoring toward personalized healthcare. LEG, laser-engraved graphene. b–g) The general procedures of QuantumDock-based MIP design: chemical database generation b), molecular docking c), density functional theory (DFT)-based binding energy calculation d), binding site and ground state identification e), target/interference-monomer property calculation for selectivity evaluation f), repeated computational optimization across targets and monomers libraries g). E, binding energy; Tar, target; Int, interferent; Mono, monomer; S, selectivity. h) The role of phenylalanine (Phe) in phenylketonuria (PKU) development. i) A fully-integrated wearable sensor based on QuantumDock-enabled Phe MIP for wireless Phe sensing toward PKU and nutritional monitoring. Scale bar, 1 cm.

4.2 Results and Discussion

4.2.1 The Process of QuantumDock-Based MIP Development

Chemically selective interactions are observed naturally in antibodies, proteins, and alike. The physical basis of this phenomena has been characterized extensively, particularly with selective isotope binding. Simply put, selective binding occurs when a target molecule (Tar) binds stronger to a candidate material than an interferant molecule (Int) in their respective ground states. The strength of binding is quantified via the binding energy (E), hence selective binding is encapsulated by the inequality $E_{Tar} > E_{Int}$ or $\Delta E = E_{Tar} - E_{Int} > 0$. For systems of molecular biomarkers, the ground state geometric configuration can be quite elusive to find. Biomolecules have multiple sites in which non-covalent interactions including hydrogen bonds, ionic bonds, and van der Waals interactions can take place (**Figures A2 and A3**, **Appendix A**). Finding the ground state, or the most stable interaction, between a target molecule and monomer can take a long time especially when the number of monomers and targets is very large (**Figure 4-11b**). Failing to do an exhaustive search for the ground state however, can yield inaccurate selectivity predictions.

To approach this issue QuantumDock employs an exhaustive yet computationally efficient docking approach in which a monomer is docked to a potential binding site on a target molecule until all binding sites have been probed (**Figure 4-11c**). All noncovalent interactions that can occur in a pre-polymerized MIP solution (hydrogen bond, electrostatic, and van der Waals) are considered in this step. The energy near every binding site is quickly calculated over hundreds of potential molecular orientations using a fast-screening method, enabling an exhaustive search of the potential energy surface for its strongest binding sites (**Figure 4-11d,e**). The most stable geometric conformations from this screening step are used in a final DFT calculation to determine the true ground state energies and binding selectivities (**Figure 4-11f**). This process can be repeated across all targets and monomers in a computational library until the optimal choices are found (**Figure 4-11g**). It should be clarified that the main application of QuantumDock is not to discover new monomers never reported before, but rather is to identify the most suitable monomer/cross-linker choices (over many monomers that could be used to prepare a biomarker MIP) with highest selectivity performance over the many potential interferences (particularly those with similar molecular structures) in their specific biosensing applications. The QuantumDock-based MIP optimization can serve as a universal approach for designing next-generation wearable biosensors that can monitor a broad spectrum of biomarkers related to various health conditions.

4.2.2 Quantum Dock-Enabled Computational Phe MIP Optimization

Being an essential amino acid, Phe plays an important role in the production of tyrosine and multiple crucial neurotransmitters (e.g., dopamine, norepinephrine, and epinephrine).[52] It is also a well-known biomarker for phenylketonuria (PKU), an inherited disorder in which the human body is unable to process Phe to tyrosine, causing an array of bodily harm.[53, 54] Despite the importance and urgent demand of personalized Phe monitoring, its wearable sensing in human subjects via sweat analysis has not been demonstrated. As such we chose Phe as a model biomarker for MIP development. Using the QuantumDock procedure, we docked 7 commonly used monomers to Phe including pyrrole (PYR), 4-vinmylbenzoic acid (4VB), acrylamide (ACM), methacrylic acid (MAA), aniline (ANI), 3-aminophenylboronic acid (APB), and o-phenylenediamine (OPD) for MIP fabrication (**Figure 4-12a**). Although many of the monomers we chose here could be used to prepare the Phe MIP based on past reports, there is no study on comparing the selectivity performance of these monomers over the major interferences (particularly those with similar molecular structures). Potential binding orientations between Phe and each monomer were first screened using semiempirical quantum mechanical calculations (**Figure 4-12b**). Such methods are particularly advantageous as they allow for quick yet fairly accurate approximations of binding energies in monomer-biomarker complexes, taking on the order of seconds to calculate molecular energies. Results from this screening correctly revealed two potential binding sites on Phe on the carboxyl (COOH) and amine (NH_2) functional groups. Semiempirical calculations are however historically known to have less accuracy than more intricate DFT calculations for calculating binding energies as they compromise accuracy for speed.[55, 56] This inaccuracy could lead to downstream errors where the predicted sensitivities and selectivities would be poorly ranked, emphasizing the need for more accurate DFT energy calculations (**Figure A4, Appendix A**). Subsequent DFT energy calculations on the most stable screened molecules indicate that the carboxylic group on Phe tends to form the most stable bonds with all monomers in our study (**Figure 4-12c,d**; **Figure S3**, **Appendix A**). This is because Phe is highly charged and has both a hydrogen bond donor and acceptor making a relatively stronger and larger binding site for strong hydrogen bonds, in agreement with molecularly electrostatic potential calculation (**Figure 4-12e**).

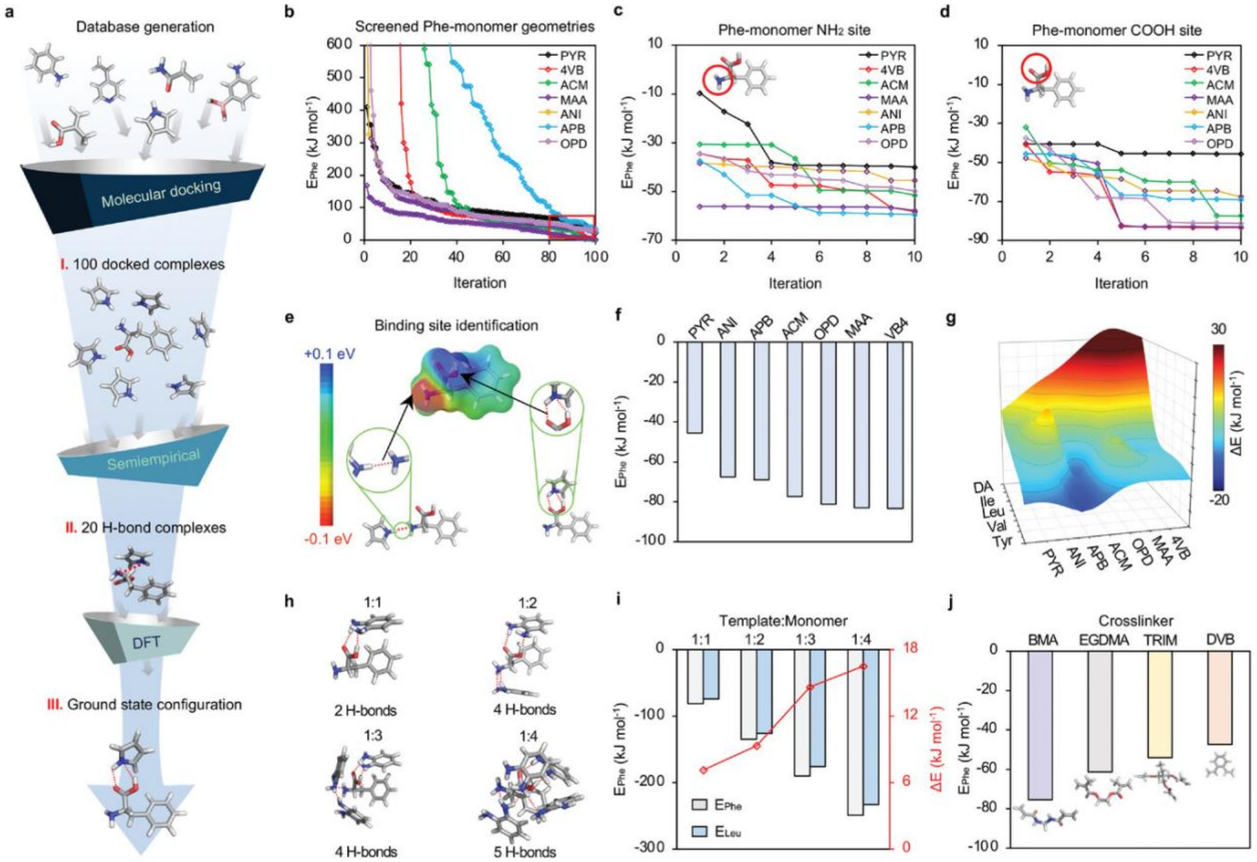

Figure 4-12: QuantumDock-based computational Phe MIP optimization. a) The procedure of QuantumDock-based Phe-monomer ground state configuration. H-bond, hydrogen bond. b) Semiempirical energy calculations based on 100 docked monomer-Phe complexes for each monomer. PYR, pyrrole; 4-VB, 4-vinmylbenzoic acid; ACM, acrylamide; MAA, methacrylic acid; ANI, aniline; APB, 3-aminophenylboronic acid; OPD, o-phenylenediamine. c,d) DFT energy calculations on the most stable screened molecules based on Phe-monomer NH_2 site c) and Phe-monomer COOH site d). e) Electrostatic potential of a Phe molecule. f) DFT-calculated binding energy of Phe-monomer. g) Colored mapping of the binding energy differences between Phe-monomer and interference-monomer complexes. Tyr, tyrosine; Val, valine; Leu, leucine; Ile, isoleucine; DA, dopamine. h) H-bonds formed in Phe-OPD complexes (ratio 1:1, 1:2, 1:3, and 1:4). i) Binding energies of Phe/OPD and Leu/OPD (target vs monomer ratio 1:1, 1:2, 1:3, and 1:4), and corresponding bonding energy differences. j) Binding energies of Phe/cross-linker. BMA, butyl methacrylate; EGDMA, ethylene glycol dimethylacrylate; TRIM, trimethylolpropane trimethacrylate; DVB, divinylbenzene.

The ground state binding energy, being the most stable or most negative calculated energy, is stored from these DFT calculations (**Figure 4-12f**; **Figure A5**, **Appendix A**). Following this quantum dock method, we find these final ground state energies to be highly reproducible (**Figure A6**, **Appendix A**). Traditionally the ground state binding energy has been used to optimize MIP sensitivity, with higher binding energies indicating a MIP will bind more target molecules to its surface. This subsequently aids detection of low concentrations when less target molecules are present in solution. Despite the use of this metric in theory, there is not much variation amongst our calculated binding energies. Of the 7 monomers used in this study, 5 (APB, ACM, OPD, MAA, VB4) had binding energies to Phe within the top quartile of calculated energies, indicating relatively low variance from monomer to monomer. Therefore, only using a high binding energy as a metric for monomer choice in MIP fabrication does not significantly slim our number of monomer choices. We therefore turn to evaluating theoretically calculated selectivity's to make greater distinction between molecules. Since selectivity (S) can be calculated as $S \propto exp(\Delta \mathrm{E}/\mathrm{k_b}T)$, where k_B and T are Boltzmann constant and temperature respectively, we calculate the binding energy difference ΔE between monomer/target and monomer/interferent as a metric to rank our monomer selection. Selectivity calculations indicate that clearly OPD, MAA, and 4VB on average have the highest potential of being selective against multiple interferants with a similar chemical structure to Phe including tyrosine (Tyr), valine (Val), leucine (Leu), isoleucine (Ile), and dopamine (DA) (**Figure 4-12g**). Such results also confirm that even though monomer PYR was also used in literature to prepare Phe MIP, the PYR MIPs suffer from bad selectivity against most chemically similar molecules. By evaluating 5 less commonly used monomers which include 1,2-ethanediol (12E), acrylic acid (ACA), phenol (PHN), 2-vinylpyridine (2VP), 2-aminophenol (2AM), we demonstrate that multiple new monomers perform better selectivity for Phe against chemically similar molecules (i.e., three other amino acid: Leu, Ile, and Val) than multiple more commonly used monomers (e.g., PYR and APB) (**Figures A7** and **A8**, **Appendix A**), indicating the powerful capability of the QuantumDock for exploring new MIP design. It should be also noted that QuantumDock is fully capable of exploring unknown monomers along with those that have been previously reported. To demonstrate this, we have simulated two further classes of unknown monomers that can be used in MIP fabrication (**Figures A7–A9**, **Appendix A**): The first being 3 monomers (methacrylamide, vinyl acetate, and 1-vinylimidazole) that have never been used to make a MIP; The second set of molecules are generated using Generative Examination Networks (GEN),[57] a popular neural network capable of generating simplified molecular input line entry system (SMILES) strings (text based encodings of molecules).[57] QuantumDock can interpret these novel SMILES strings, generate their 3D conformations, and test their selectivity against our previously listed interferants. The combination of a generative algorithm with QuantumDock shows the algorithms full potential of being able to generate, and screen through countless monomers for MIP development. Screening through a larger number of monomers opens up the possibility of finding novel monomers with higher selectivity and sensitivity. Interestingly enough, the novel topology of molecules generated via the GEN neural network shows much higher selectivities than the typical monomers used in MIP fabrication (**Figures A8 and A9**, **Appendix A**).

Furthermore, calculations in which the monomer template ratio was modified showed a much more efficient means of increasing both monomer template binding energies and binding energy differences (**Figure 4-12h,i**). Increasing the number of monomers in the monomer template ratio allowed more binding sites on the Phe template to be accessed, increasing the binding energy and binding energy difference of the target-monomer complex. This increase seems to have diminishing returns once binding sites become saturated, the binding energy of the target-monomer complex stops increasing as rapidly. Finally, we calculate the binding energies between Phe and various potential cross-linkers for use of study (**Figure 4-12j**). It is well established that cross-linkers with low binding energies to the target molecule have the best potential for MIP fabrication.[58] Cross-linkers which bind poorly to the target molecule are less likely to nonspecifically bind to it in the polymerization process, and in effect more likely to contribute to the rigidity of the final polymer structure as intended. We therefore chose divenylbenze (DVB) as our cross-linker of choice. Its low binding energy to Phe can be attributed to it not having any hydrogen bond donor or acceptor atoms, making it an optimal candidate.

4.2.3 Experimental Validation of QuantumDock Using Solution-Synthesized MIP NPs

To experimentally validate the QuantumDock-based computationally optimized MIP, a series of MIP NPs were synthesized and characterized by the binding/adsorption amount toward target and interferent molecules. All MIP NPs were prepared in a solution containing Phe, monomer and cross-linker molecules of choice under 60 °C with azobisisobutyronitrile as the initiator (**Figure 4-13a**). Methanol was added into water (4:1 (v/v)) as a solvent to maximize the binding energy (Figure S10, Supporting Information). Non-imprinted polymer nanoparticles (NIP NPs) were fabricated following the same procedure with the exclusion of the Phe template molecule. The resultant MIP NPs have a size of ≈50 nm according to the scanning electron microscopy (SEM) image (**Figure 4-13b**). Energy dispersive X-ray (EDX) analysis of the MIP NPs before and after target extraction showed a sharp

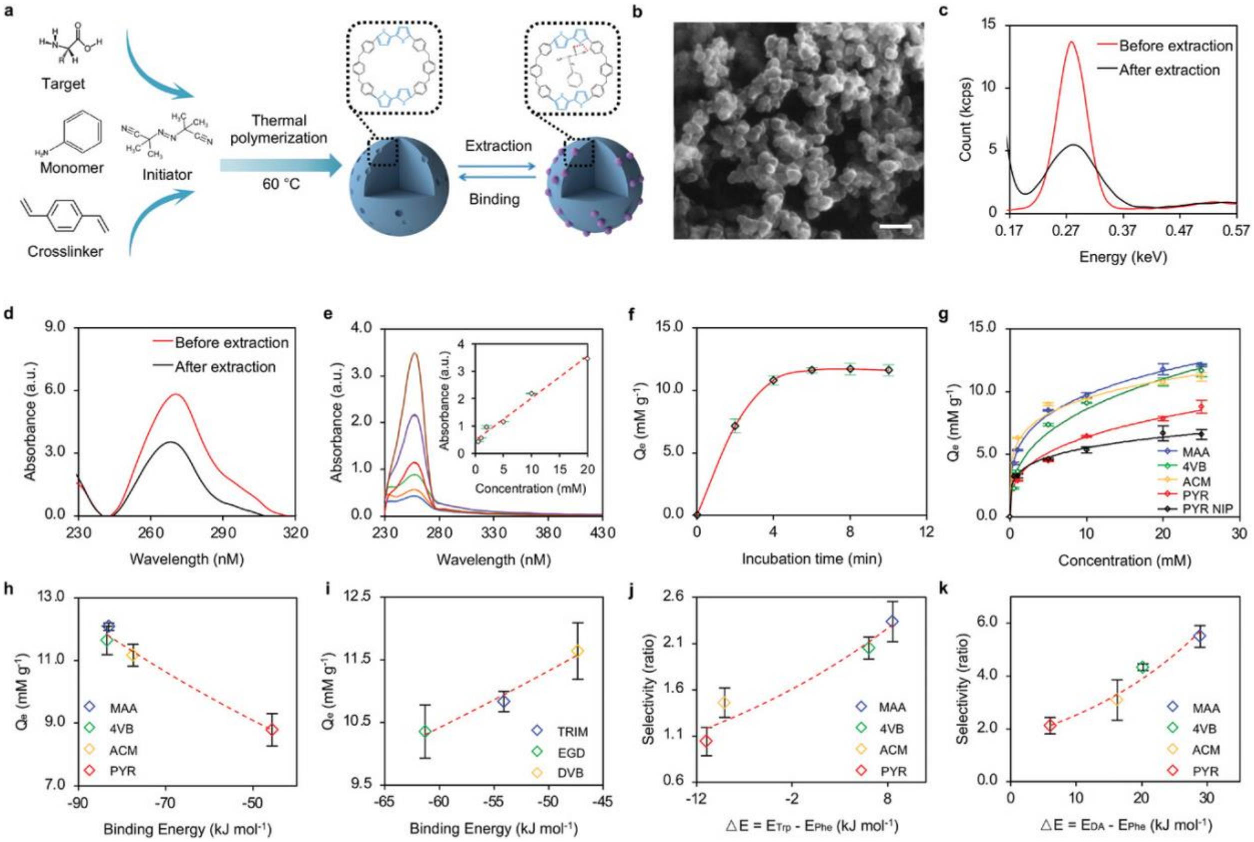

Figure 4-13: Experimental validation of QuantumDock-optimized Phe MIP using solution-synthesized NPs. a) Solution synthesis process of Phe MIP NPs. b) Scanning electron microscopy (SEM) image of Phe-PYR MIP NPs. Scale bar, 200 nm. c) Energy-dispersive X-ray spectroscopy results of carbon elements in the Phe-PYR MIP NPs before and after target extraction. d) Ultraviolet–visible spectroscopy (UV–vis) absorbance of Phe-PYR MIP NPs before and after template extraction. e) UV–vis absorbance of Phe-PYR MIP NPs after incubation of 500 µM–20 mM Phe. Insets, calibration plots with a linear fit. f) The maximum adsorption amount (Q_e) of Phe-PYR MIP NPs over incubation time. g) Q_e of Phe/monomer MIP NPs upon incubation in 500 µM–20 mM Phe. h) The relationship between Q_e of the Phe MIP NPs and calculated Phe-monomer binding energies. i) The relationship between Q_e of the Phe MIP NPs and calculated Phe-cross-linker binding energies. j,k) Selectivity of Phe MIP NPs based on different monomers over interferents DA j) and Trp k). All error bars represent the s.d. from three measurements.

decrease at the carbon alpha emission lines after Phe extraction (**Figure 4-13c**), suggesting the successful extraction of Phe molecules. Such target extraction was further validated by conducting ultraviolet–visible spectroscopy (UV–vis) before and after extraction on a sample containing MIP NPs. The absorbance peak at ≈270 nm wavelength was consistent with Phe's UV-absorption maxima decreases after target extraction (**Figure 4-13d**). It should be noted that the peak is however still present as there will be some Phe molecules trapped inside the polymer matrix after extraction.

Isotherm experiments were conducted to investigate the binding dynamics of Phe to various MIP NPs fabricated with different monomers. A linear relationship was identified between the absorbance peak height at ≈270 nm and the Phe concentration in the range between 500 µM and 20 mM (**Figure 4-13e**). The maximal absorption of each MIP NPs Q_e was calculated as $Q_e = (C_0 - C_t)/(m/V)$ where m/V is the MIP NP density, C_0 is the initial target molecule solution concentration, and C_t is the concentration recorded after incubating MIP NPs in solution. An incubation time of at least 6 min was determined to be optimal as Q_e tended to maximize at this time, indicating the system had reached thermodynamic equilibrium (**Figure 4-13f**). Q_e results show a distinction between each monomer with MAA being highest on average and PYR the lowest next to its NIP counterpart (**Figure 4-13g**). These results are in agreement with the DFT calculations of the binding energy between monomers and Phe (**Figure 4-13h**), indicating that when a target molecule binds stronger to a MIP binding site, more of said target molecules will bind to the MIP. This effect can be used to increase the MIP's sensitivity by binding more of the target even at low concentrations, hence increasing the resulting sensor signal response. Further, we have successfully validated that cross-linkers with low binding energy to template molecules lead to higher Q_e (**Figure 4-13i**).

Further studies were carried out to probe the MIPs capability to selectively bind to Phe over other interfering molecules. Selectivity $S = Q_e^{Tar}/Q_e^{Int}$ is measured as the amount of target molecules a MIP particle can absorb (Q_e^{Tar}) divided by the amount of interferant molecules the MIP is capable of absorbing (Q_e^{Int}). This selectivity metric directly indicates a MIPs capability to preferentially bind its imprinted target molecule over any potentially coexisting interferant. To our knowledge no such study has probed into the correlation using this measured selectivity nor any theoretical description of selectivity. As illustrated in **Figure 4-13j,k**, using DA and Trp as the exemplar interferents (**Figure A11**, **Appendix A**), our selectivity results of the Phe MIP NPs verified the previously described theoretical derivation of selectivity which states that selectivity is exponentially proportional to the binding energy difference. This result is especially interesting as it shows optimizing selectivity computational can quickly yield significant improvements in a MIPs selectivity, hence drastically increasing a biosensors performance. It should be noted that the binding energy difference calculated by the intermediate binding states could lead to large prediction error (**Figure A12**, **Appendix A**). Therefore, QuantumDock's capability to reproducibly find the most stable ground state binding energies is critical for selectivity prediction.

4.2.4 Electrochemical Graphene Sensor Development toward Continuous Sweat Phe Monitoring

Applying the QuantumDock-optimized MIPs to wearable biosensors, we developed a flexible electrochemical biosensor using the Phe MIP as the bio-receptor to specifically capture free Phe molecule in the sweat (**Figure 4-14a**). Considering the low concentration of Phe in human sweat (µM level), flexible laser-engraved graphene (LEG) on a polyimide substrate was chosen as the electrode material to increase the sensor sensitivity and skin conformability as it has a large surface area, high electrochemical catalytic activity, high mechanical flexibility, and can be mass-producible at a large scale (**Figures A13** and **A14**, **Appendix A**).[33, 59] To prepare the biosensor, the Phe MIP

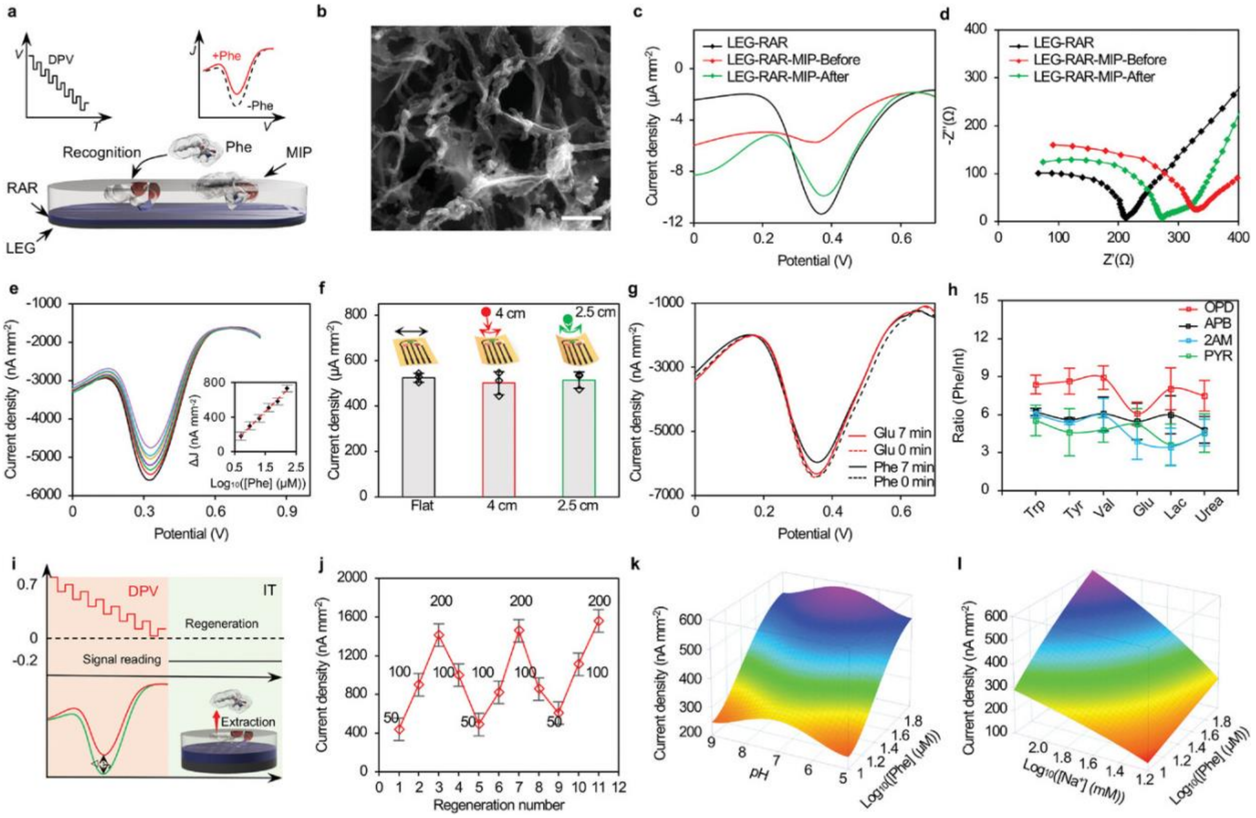

Figure 4-14: Characterization of electrochemical graphene-based Phe sensor. a) The mechanism of the electrochemical Phe MIP sensor based on the laser-engraved graphene (LEG) and the redox-active reporter (RAR). b) SEM image of an LEG-RAR-MIP electrode. Scale bar, 1 µm. c,d) Differential pulse voltammetry (DPV) c) and electrochemical impedance spectroscopy (EIS) d) results of an LEG-RAR electrode, an LEG-RAR-MIP electrode before target extraction, and an LEG-RAR-MIP electrode after target extraction. Z, impedance; Z', resistance; Z'', reactance. e, DPV voltammograms and the corresponding calibration curves of Phe detection using the LEG-RAR-MIP sensors. f) DPV peak height of current density of the Phe sensor under mechanical deformation. Error bars represent the s.d. from three sensors. g) DPV voltammograms of an LEG-RAR-MIP Phe sensor before and after incubation in Phe and Leu. h) The target (Phe) to interference signal ratios of the LEG-RAR-OPD, LEG-RAR-APB, and LEG-RAR-PRY MIP sensors. i) Calibration strategies of the wearable LEG-MIP sensors involving a two-step DPV-scan calibration for automatic in situ Phe analysis. j) In situ continuous sensing and regeneration of an LEG–RAR–MIP Phe sensor in Phe solutions. k,l) Color maps showing the dependence of the LEG-RAR-MIP Phe sensor response on pH k) and Na^+ l) concentrations. All error bars represent the s.d. from three sensors.

layer was directly electro-polymerized onto an LEG electrode followed by the target extraction. The selective recognition molecule into the imprinted polymeric layer can be further converted to a measurable electrochemical signal by incorporating a redox active reporter (RAR) layer between the Phe MIP film and the LEG electrode. The target adsorption reduces the exposure of the RAR (nickel hexacyanoferrate here) to the sample matrix and further block the electron transfer and thus leads to a decreased redox signal (**Figure 4-14a**). The SEM image of the Phe sensor clearly shows a highly porous 3D structure of the LEG covered uniformly by a polymeric MIP film and RAR NPs (**Figure 4-14b**).

The successful MIP electrochemical sensor preparation was characterized and validated using differential pulse voltammetry (DPV) (**Figure 4-14c**). The LEG-RAR displayed the highest reduction peak of RAR which decreased substantially after polymerization of the polymer film (LEG-RAR-MIP-before) due to the RAR blockage by the polymer; the extraction of the template molecule (Phe) led to the target selective cavities and increased exposure of the RAR site to the sample matrix, resulting in an increased reduction signal (**Figure 4-14c**). In addition, the MIP sensor preparation was further validated using open-circuit potential-electrochemical impedance spectroscopy (OCP-EIS): the electrode resistance in Nyquist plots decreased after the extraction of the template, suggesting the increased exposure for RAR to the sample matrix (**Figure 4-14d**).

For Phe quantification, DPV was used to measure the RAR's reduction peak of the LEG-RAR-MIP Phe sensor, where the decrease in the peak current correlated with an increase in Phe concentration. A log-linear relationship between the decreased peak current density height of the DPV voltammograms and Phe concentration (**Figure 4-14e**) was achieved with a sensitivity of 353.94 nA mm^{-2} per decade of concentration, when OPD was used as the monomer. The flexible LEG sensors demonstrated stable electrochemical performance under mechanical deformation (**Figure 4-14f**). Moreover, the sensor showed excellent selectivity toward other analytes with similar structures such as Leu: a substantially higher DPV reduction peak decrease was observed for Phe detection compared to that obtained after incubation with interferent Leu (**Figure 4-14g**). Overall, compared with APB and PYR MIP-based sensors, the OPD MIP-based sensors show improved selectivity for the detection of Phe over common physiological-level interferents (**Figure 4-14h**;

Figure A15, **Appendix A**), consistent with the QuantumDock's computational results on ΔE (**Figure 4-12g**).

To enable automatic Phe detection in human sweat toward non-invasive wearable sensing, we utilized here an in-situ calibration strategy involving two-step DPV scans: the first scan was performed to determine the background signal before target recognition while the second scan was performed after incubation to determine the reduction signal change; in situ regeneration was realized by applying constant current to the MIP electrode to repel the bound Phe molecules (**Figure 4-14i**). Continuous and repetitive Phe detection between low concentration and high concentration can thus be realized automatically (**Figure 4-14j**). Considering that the variations of individual's sweat composition could affect the in situ Phe measurement, we characterized the dependence of pH or solution conductivity (Na^+) on the response of the Phe sensor, as illustrated in **Figure 4-14k,l**. Considering that both pH and Na^+ have substantial influence on the Phe sensor reading, it is important to simultaneously monitor pH and Na^+ levels for in situ accurate sweat analysis.

4.2.5 Development of the Fully-Integrated Wearable and Flexible Phe Sensor Patch

To enable the continuous Phe monitoring, a wireless wearable sensor patch was developed based on our previously established platform[33] that contains two carbachol-loaded LEG iontophoresis electrodes for prolonged localized on-demand sweat induction, a laser-engraved microfluidic module for sweat sampling, and a sensor array consisting of a QuantumDock-optimized LEG-OPD MIP Phe sensor (**Figure 4-15a–c**; **Figure A16**, **Appendix A**). The integrated system can perform on-demand iontophoresis, multimodal electrochemical sensing, and wireless communication (**Figure 4-15d**; **Figure A17**,**Appendix A**). Electrochemical ion-selective pH and Na^+ sensors are intergraded into the wearable sensor patch to realize accurate wearable Phe analysis in sweat monitoring via real-time sensor calibration in real time (**Figure 4-15e,f**). The accuracy of the wearable Phe sensor patch for analyzing raw human sweat was verified using the gold standard gas chromatography-mass spectrometry (GC-MS): a very high correlation between the results from sensors and from GC-MS was observed (**Figure 4-15g**). The sensor patch is able to autonomously induce sweat through iontophoresis (to deliver carbachol below the skin) at rest without the need for vigorous exercise; a microfluidic module was used to efficiently sample the fresh sweat generated from the sweat gland due to the nicotinic effects of carbachol to facilitate the real-time sweat analysis (**Figure 4-15h**; **Figure A18**).

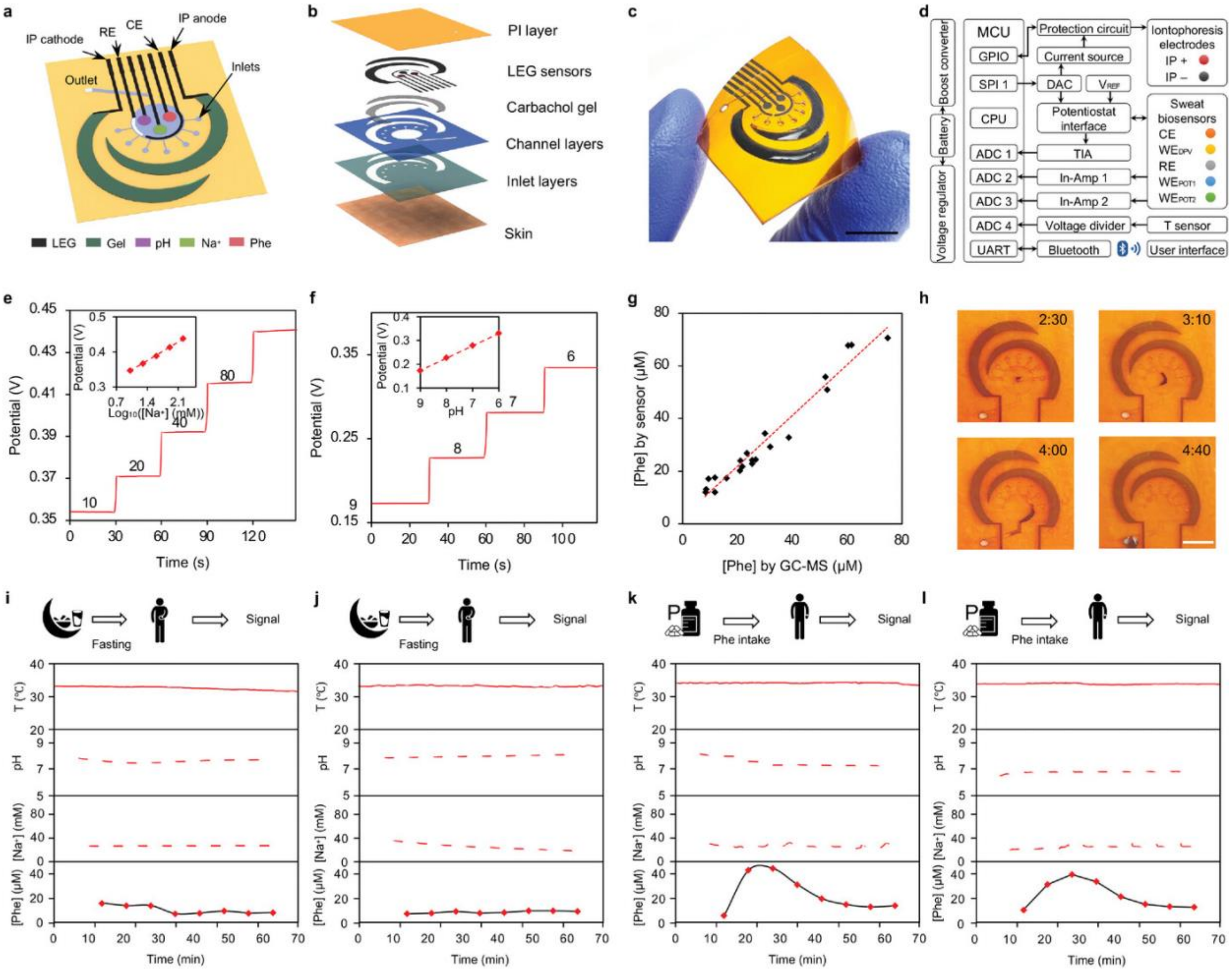

Figure 4-15: Design and in vivo evaluation of the fully-integrated wearable flexible MIP-based Phe sensor. a,b) Schematic a) and layer assembly b) of the wearable microfluidic Phe sensor patch for autonomous sweat induction, sampling, and biosensing. CE, counter electrode; RE, reference electrode; IP, iontophoresis. d) Block diagram of electronic system of the wearable Phe sensor. CPU, central processing unit; POT, potentiometry; In-Amp, instrumentation amplifier; MCU, microcontroller; TIA, trans-impedance amplifier; WE, working electrode. e,f) Calibration plots obtained using the wearable system from the Na^+ e) and pH f) sensors. g) Validation of Phe sensors for raw sweat samples (*n* = 21) analysis against gas chromatography–mass spectrometry (GC-MS). h) On-body evaluation of the microfluidic patch for efficient sweat induction and sampling at rest. Timestamps represent the period (min) after a 5 min iontophoresis session. Black dye was used in the reservoir to facilitate the direct visualization of sweat flow in the microfluidics. Scale bar, 5 mm. i,j) Autonomous Phe monitoring of two healthy subjects using the wearable sensors at a fasting state. k,l) Autonomous Phe monitoring of two healthy subjects using the wearable sensors after Phe intake. For i–l) a 5 min iontophoresis was performed in the beginning of the trial followed by multiplexed data recording. Temperature, pH, Na^+ was recorded simultaneously for signal calibration.

Clinical on-body evaluation of the wearable system toward personalized nutritional monitoring was performed via sensing of sweat Phe in human subjects at rest with and without Phe supplement intake.

The DPV signal from the Phe sensor worn on the subjects' wrist was wirelessly transmitted along with temperature, pH and Na^+ sensor readings to the interface that automatically performed calibration for the accurate quantification of sweat Phe (**Figure 4-15i–l**; **Figure A19**). As expected, rapidly rising Phe levels in sweat were observed from all two subjects after Phe supplement intake while the Phe levels remained stable during the fasting studies. This represents the first demonstration of continuous non-invasive wearable sweat Phe sensing in human subjects. Such a good capability indicates the great potential for non-invasive Phe monitoring using the wearable sensor and opens the door for PKU management through personalized sensor-guided dietary intervention.

4.3 Conclusion

We demonstrated a computational framework – QuantumDock – for optimizing MIP performance toward a wide range of wearable biosensing applications. Through DFT-based probing of intermolecular interactions between monomers and the targets/interferents, we were able to develop MIP-based sensors with enhanced selectivity, a crucial factor for in situ wearable biomarker analysis. Through the screening a number of molecules, we demonstrated that QuantumDock also has the potential to explore a wide range of commonly used and unknown monomers for designing better MIPs. We successfully validated the QuantumDock-based MIP design and optimization using solution-synthesized MIP NPs. We further show the potential for generative artificial intelligence in materials design by using GEN to generate novel monomers with significantly higher theoretical selectivities than commonly used MIP monomers. Based on the QuantumDock-optimized MIP, we also developed a laser-engraved graphene-based wearable electrochemical Phe sensor capable of autonomous sweat extraction, sampling, and sensing without the need for vigorous exercise. The first wearable non-invasive Phe monitoring in human subjects revealed the high potential of such technology for personalized nutritional and healthcare applications. As QuantumDock is a universal sensor optimization approach that can be easily adapted toward other important biomarkers in human body fluids, we envision that it will enable the demonstration of high-performance MIP sensors for the analysis of a wide range of biomarker and facilitate the realization of practical wearable healthcare applications.

BIBLIOGRAPHY

[1] T. R. Ray, J. Choi, A. J. Bandodkar, S. Krishnan, P. Gutruf, L. Tian, R. Ghaffari, J. A. Rogers, *Chem. Rev.* **2019**, *119*, 5461.

[2] C. Xu, Y. Yang, W. Gao, *Matter* **2020**, *2*, 1414.

[3] M. L. Hammock, A. Chortos, B. C.-K. Tee, J. B.-H. Tok, Z. Bao, *Adv. Mater.* **2013**, *25*, 5997.

[4] Y. Luo, M. R. Abidian, J.-H. Ahn, D. Akinwande, A. M. Andrews, M. Antonietti, Z. Bao, M. Berggren, C. A. Berkey, C. J. Bettinger, J. Chen, P. Chen, W. Cheng, X. Cheng, S.-J. Choi, A. Chortos, C. Dagdeviren, R. H. Dauskardt, C. Di, M. D. Dickey, X. Duan, A. Facchetti, Z. Fan, Y. Fang, J. Feng, X. Feng, H. Gao, W. Gao, X. Gong, C. F. Guo, X. Guo, M. C. Hartel, Z. He, J. S. Ho, Y. Hu, Q. Huang, Y. Huang, F. Huo, M. M. Hussain, A. Javey, U. Jeong, C. Jiang, X. Jiang, J. Kang, D. Karnaushenko, A. Khademhosseini, D.-H. Kim, I.-D. Kim, D. Kireev, L. Kong, C. Lee, N.-E. Lee, P. S. Lee, T.-W. Lee, F. Li, J. Li, C. Liang, C. T. Lim, Y. Lin, D. J. Lipomi, J. Liu, K. Liu, N. Liu, R. Liu, Y. Liu, Y. Liu, Z. Liu, Z. Liu, X. J. Loh, N. Lu, Z. Lv, S. Magdassi, G. G. Malliaras, N. Matsuhisa, A. Nathan, S. Niu, J. Pan, C. Pang, Q. Pei, H. Peng, D. Qi, H. Ren, J. A. Rogers, A. Rowe, O. G. Schmidt, T. Sekitani, D.-G. Seo, G. Shen, X. Sheng, Q. Shi, T. Someya, Y. Song, E. Stavrinidou, M. Su, X. Sun, K. Takei, X.-M. Tao, B. C. K. Tee, A. V.-Y. Thean, T. Q. Trung, C. Wan, H. Wang, J. Wang, M. Wang, S. Wang, T. Wang, Z. L. Wang, P. S. Weiss, H. Wen, S. Xu, T. Xu, H. Yan, X. Yan, H. Yang, L. Yang, S. Yang, L. Yin, C. Yu, G. Yu, J. Yu, S.-H. Yu, X. Yu, E. Zamburg, H. Zhang, X. Zhang, X. Zhang, X. Zhang, Y. Zhang, Y. Zhang, S. Zhao, X. Zhao, Y. Zheng, Y.-Q. Zheng, Z. Zheng, T. Zhou, B. Zhu, M. Zhu, R. Zhu, Y. Zhu, Y. Zhu, G. Zou, X. Chen, *ACS Nano* **2023**, *17*, 211.

[5] E. Shirzaei Sani, C. Xu, C. Wang, Y. Song, J. Min, J. Tu, S. A. Solomon, J. Li, J. L. Banks, D. G. Armstrong, W. Gao, *Sci. Adv.* **2023**, *9*, eadf7388.

[6] M. Sang, K. Kang, Y. Zhang, H. Zhang, K. Kim, M. Cho, J. Shin, J. Hong, T. Kim, S. K. Lee, W. Yeo, J. W. Lee, T. Lee, B. Xu, K. J. Yu, *Adv. Mater.* **2022**, *34*, 2105865.

[7] K. Meng, X. Xiao, W. Wei, G. Chen, A. Nashalian, S. Shen, X. Xiao, J. Chen, *Adv. Mater.* **2022**, *34*, 2109357.

[8] X. Liang, M. Zhu, H. Li, J. Dou, M. Jian, K. Xia, S. Li, Y. Zhang, *Adv. Funct. Mater.* **2022**, *32*, 2200162.

[9] K. Chun, S. Seo, C. Han, *Adv. Mater.* **2022**, *34*, 2110082.

[10] Y. Yang, W. Gao, *Chem. Soc. Rev.* **2019**, *48*, 1465.

[11] J. Kim, A. S. Campbell, B. E.-F. de Ávila, J. Wang, *Nat. Biotechnol.* **2019**, *37*, 389.

[12] M. Bariya, H. Y. Y. Nyein, A. Javey, *Nat. Electron.* **2018**, *1*, 160.

[13] J. Heikenfeld, A. Jajack, B. Feldman, S. W. Granger, S. Gaitonde, G. Begtrup, B. A. Katchman, *Nat. Biotechnol.* **2019**, *37*, 407.

[14] A. J. Bandodkar, W. J. Jeang, R. Ghaffari, J. A. Rogers, *Ann. Rev. Anal. Chem.* **2019**, *12*, 1.

[15] J. R. Sempionatto, J. A. Lasalde-Ramírez, K. Mahato, J. Wang, W. Gao, *Nat. Rev. Chem.* **2022**, *6*, 899.

[16] J. Xu, Y. Fang, J. Chen, *Biosensors* **2021**, *11*, 245.

[17] H. C. Ates, P. Q. Nguyen, L. Gonzalez-Macia, E. Morales-Narváez, F. Güder, J. J. Collins, C. Dincer, *Nat. Rev. Mater.* **2022**, *7*, 887.

[18] H. Shen, H. Lei, M. Gu, S. Miao, Z. Gao, X. Sun, L. Sun, G. Chen, H. Huang, L. Chen, Z. Wen, *Adv. Funct. Mater.* **2022**, *32*, 2204525.

[19] L. Wang, J. Lu, Q. Li, L. Li, E. He, Y. Jiao, T. Ye, Y. Zhang, *Adv. Funct. Mater.* **2022**, *32*, 2200922.

[20] H. Zhao, X. Zhang, Y. Qin, Y. Xia, X. Xu, X. Sun, D. Yu, S. M. Mugo, D. Wang, Q. Zhang, *Adv. Funct. Mater.* **2023**, *33*, 2212083.

[21] X. Yang, J. Yi, T. Wang, Y. Feng, J. Wang, J. Yu, F. Zhang, Z. Jiang, Z. Lv, H. Li, T. Huang, D. Si, X. Wang, R. Cao, X. Chen, *Adv. Mater.* **2022**, *34*, 2201768.

[22] Y. Tang, S. Gan, L. Zhong, Z. Sun, L. Xu, C. Liao, K. Lin, X. Cui, D. He, Y. Ma, W. Wang, L. Niu, *Adv. Funct. Mater.* **2022**, *32*, 2107653.

[23] J. Min, J. Tu, C. Xu, H. Lukas, S. Shin, Y. Yang, S. A. Solomon, D. Mukasa, W. Gao, *Chem. Rev.* **2023**, *123*, 5049.

[24] W. Gao, S. Emaminejad, H. Y. Y. Nyein, S. Challa, K. Chen, A. Peck, H. M. Fahad, H. Ota, H. Shiraki, D. Kiriya, D. H. Lien, G. A. Brooks, R. W. Davis, A. Javey, *Nature* **2016**, *529*, 509.

[25] S. Emaminejad, W. Gao, E. Wu, Z. A. Davies, H. Yin Yin Nyein, S. Challa, S. P. Ryan, H. M. Fahad, K. Chen, Z. Shahpar, S. Talebi, C. Milla, A. Javey, R. W. Davis, *Proc. Natl. Acad. Sci. USA* **2017**, *114*, 4625.

[26] Y. Yu, J. Nassar, C. Xu, J. Min, Y. Yang, A. Dai, R. Doshi, A. Huang, Y. Song, R. Gehlhar, A. D. Ames, W. Gao, *Sci. Robot.* **2020**, *5*, eaaz7946.

[27] J. R. Sempionatto, M. Lin, L. Yin, E. De la paz, K. Pei, T. Sonsa-ard, A. N. de Loyola Silva, A. A. Khorshed, F. Zhang, N. Tostado, S. Xu, J. Wang, *Nat. Biomed. Eng.* **2021**, *5*, 737.

[28] H. Lee, T. K. Choi, Y. B. Lee, H. R. Cho, R. Ghaffari, L. Wang, H. J. Choi, T. D. Chung, N. Lu, T. Hyeon, S. H. Choi, D.-H. Kim, *Nat. Nanotech.* **2016**, *11*, 566.

[29] X. Xuan, C. Pérez-Ràfols, C. Chen, M. Cuartero, G. A. Crespo, *ACS Sens.* **2021**, *6*, 2763.

[30] H. Y. Y. Nyein, M. Bariya, B. Tran, C. H. Ahn, B. J. Brown, W. Ji, N. Davis, A. Javey, *Nat Commun* **2021**, *12*, 1823.

[31] J. R. Sempionatto, A. A. Khorshed, A. Ahmed, A. N. De Loyola e Silva, A. Barfidokht, L. Yin, K. Y. Goud, M. A. Mohamed, E. Bailey, J. May, C. Aebischer, C. Chatelle, J. Wang, *ACS Sens.* **2020**, *5*, 1804.

[32] A. J. Bandodkar, P. Gutruf, J. Choi, K. Lee, Y. Sekine, J. T. Reeder, W. J. Jeang, A. J. Aranyosi, S. P. Lee, J. B. Model, R. Ghaffari, C.-J. Su, J. P. Leshock, T. Ray, A. Verrillo, K. Thomas, V. Krishnamurthi, S. Han, J. Kim, S. Krishnan, T. Hang, J. A. Rogers, *Sci. Adv.* **2019**, *5*, eaav3294.

[33] Y. Yang, Y. Song, X. Bo, J. Min, O. S. Pak, L. Zhu, M. Wang, J. Tu, A. Kogan, H. Zhang, T. K. Hsiai, Z. Li, W. Gao, *Nat. Biotechnol.* **2020**, *38*, 217.

[34] R. M. Torrente-Rodríguez, J. Tu, Y. Yang, J. Min, M. Wang, Y. Song, Y. Yu, C. Xu, C. Ye, W. W. IsHak, W. Gao, *Matter* **2020**, *2*, 921.

[35] M. Wang, Y. Yang, J. Min, Y. Song, J. Tu, D. Mukasa, C. Ye, C. Xu, N. Heflin, J. S. McCune, T. K. Hsiai, Z. Li, W. Gao, *Nat. Biomed. Eng.* **2022**, *6*, 1225.

[36] T. R. Ray, M. Ivanovic, P. M. Curtis, D. Franklin, K. Guventurk, W. J. Jeang, J. Chafetz, H. Gaertner, G. Young, S. Rebollo, J. B. Model, S. P. Lee, J. Ciraldo, J. T. Reeder, A. Hourlier-Fargette, A. J. Bandodkar, J. Choi, A. J. Aranyosi, R. Ghaffari, S. A. McColley, S. Haymond, J. A. Rogers, *Sci. Transl. Med.* **2021**, *13*, eabd8109.

[37] X. He, T. Xu, Z. Gu, W. Gao, L.-P. Xu, T. Pan, X. Zhang, *Anal. Chem.* **2019**, *91*, 4296.

[38] X. Pei, M. Sun, J. Wang, J. Bai, X. Bo, M. Zhou, *Small* **2022**, *18*, 2205061.

[39] M. Sun, X. Pei, T. Xin, J. Liu, C. Ma, M. Cao, M. Zhou, *Anal. Chem.* **2022**, *94*, 1890.

[40] X. He, C. Fan, Y. Luo, T. Xu, X. Zhang, *npj Flex Electron* **2022**, *6*, 60.

[41] J. Tu, R. M. Torrente-Rodríguez, M. Wang, W. Gao, *Adv. Funct. Mater.* **2020**, *30*, 1906713.

[42] O. Parlak, S. T. Keene, A. Marais, V. F. Curto, A. Salleo, *Sci Adv* **2018**, *4*, eaar2904.

[43] R. M. Torrente-Rodríguez, H. Lukas, J. Tu, J. Min, Y. Yang, C. Xu, H. B. Rossiter, W. Gao, *Matter* **2020**, *3*, 1981.

[44] B. Wang, C. Zhao, Z. Wang, K.-A. Yang, X. Cheng, W. Liu, W. Yu, S. Lin, Y. Zhao, K. M. Cheung, H. Lin, H. Hojaiji, P. S. Weiss, M. N. Stojanović, A. J. Tomiyama, A. M. Andrews, S. Emaminejad, *Sci. Adv.* **2022**, *8*, eabk0967.

[45] J. J. BelBruno, *Chem. Rev.* **2019**, *119*, 94.

[46] O. S. Ahmad, T. S. Bedwell, C. Esen, A. Garcia-Cruz, S. A. Piletsky, *Trends Biotech.* **2019**, *37*, 294.

[47] W. Tang, L. Yin, J. R. Sempionatto, J. Moon, H. Teymourian, J. Wang, *Adv. Mater.* **2021**, *33*, 2008465.

[48] J. O. Mahony, K. Nolan, M. R. Smyth, B. Mizaikoff, *Anal. Chim. Acta* **2005**, *534*, 31.

[49] J. Yao, X. Li, W. Qin, *Anal. Chim. Acta* **2008**, *610*, 282.

[50] T. Cowen, K. Karim, S. Piletsky, *Anal. Chim. Acta* **2016**, *936*, 62.

[51] M. Tabandeh, S. Ghassamipour, H. Aqababa, M. Tabatabaei, M. Hasheminejad, *J. Chromatogr. B* **2012**, *898*, 24.

[52] J. D. Fernstrom, M. H. Fernstrom, *J. Nutr.* **2007**, *137*, 1539S.

[53] R. A. Williams, C. D. S. Mamotte, J. R. Burnett, *Clin. Biochem. Rev.* **2008**, *29*, 31.

[54] N. Blau, F. J. van Spronsen, H. L. Levy, *Lancet* **2010**, *376*, 1417.

[55] J. Tirado-Rives, W. L. Jorgensen, *J. Chem. Theory Comput.* **2008**, *4,* 297.

[56] M. Azenha, P. Kathirvel, P. Nogueira, A. Fernando-Silva, *Biosens. Bioelectron.* **2008**, *23,* 1843.

[57] R. Van Deursen, P. Ertl, I. V. Tetko, G. Godin, *J. Cheminform.* **2020**, *12*, 22.

[58] R. van Deursen, P. Ertl, I. V. Tetko, G. Godin, *J. Cheminform.* **2020**, *12*, 22.

[59] T. Muhammad, Z. Nur, E. V. Piletska, O. Yimit, S. A. Piletsky, *Analyst* **2012**, *137*, 2623.

[60] M. Wang, Y. Yang, W. Gao, *Trends Chem.* **2021**, *3,* 969.

APPENDIX A

Selectivity thermodynamic derivation Computational MIP design has historically been based around the calculation of a binding energy E which indicates how strongly a target molecule will bind to a potential monomer. With strong binding energies, stable target-monomer complex can for in the pre-polymerization solution and remain bound through the polymerization process. After subsequent elution of the target from the polymer matrix a well-defined imprinted site remains with a high affinity for target molecules in solution. This model however leaves out consideration on how to make a MIP more selective which, to date, no group has explicitly proposed a theoretical basis for, nor experimental validation. Selective binding has been studied with ideal gasses, particularly with selective isotope binding[29]. The theoretical basis of this binding event treats two molecules, indexed i, as ideal gasses competing to bind to an absorbing material. Hence the molecules have a chemical potential:

$$\mu_i^{free} = k_b T ln\left(n_i \lambda_i / q_i^{int}\right)$$

and an absorbed chemical potential:

$$\mu_i^{abs} = E_i^0 + k_b T ln\left(\rho_i \lambda_i / q_i^{int}\right)$$

where E_i 0 denotes ground state energy of molecule i in the presence of the absorbing material, q_i int the internal partition function, λ_i the de Broglie wavelength, ni the density of free particles, and ρi the density of absorbed molecules[10–13]. Given ample time to reach thermodynamic equilibrium (i.e. μ_i $free$ = μ_i $bound$) the ratio of absorbed i molecules to free molecules is

$$\frac{\rho_i}{n_i} = \lambda_i^{-2} \exp\left(E_i^0 / k_b T\right).$$

Taking note that

$$\lambda_i = \sqrt{2\pi\hbar^2 / m_i k_b T}$$

selectivity’s functional form clearly becomes

$$S = \frac{\rho_1}{\rho_2} / \frac{n_1}{n_2} = \frac{m_2}{m_1} \exp\left([E_2^0 - E_1^0]/\, k_b T\right) = \frac{m_2}{m_1} \exp\left(\Delta E / k_b T\right)$$

QuantumDock-enabled Phe MIP optimization QuantumDock uses the Orca software for the bulk of its calculations[14]. The docking procedure relies on semiempirical calculations in which we identify potential binding sites (namely hydrogen bond donor or acceptor atoms) and place our monomer/crosslinker within proximity of this site. Configurations with hydrogen bonds will present lower energies due to attractive nature of the bond. As such, single point energies are calculated using the semiempirical PM3 method. This method has the advantage of being relatively more accurate than other semiempirical calculations, but still has the capability to calculate energies quickly (normally with the order of seconds per geometry). This enables the probing of hundreds of geometries without the need for more expensive DFT methods. As previously noted however, semiempirical calculations have poor accuracy compared to experiments (Supplementary Fig. 3), hence necessitating more expensive DFT calculations. The same binding energy calculation at the level of theory of DFT drastically increases the time to complete a calculation, taking anywhere from 5–100+ hours depending on the number of atoms being simulated. To limit the total computational time only the 20 most stable configurations from the previous docking step are probed further using geometry optimization at the DFT level of theory. We utilize the B3LYP function with a 6-31**++ basis set and D3BJ dispersion corrections as it strikes the perfect balance between computational cost and notable accuracy. Final binding energies were calculated using the standard formula

$$E_{Binding} = E_{Complex} - (E_{Tar/Int} + \sum E_{Mono/Crosslinker}).$$

Intermediate geometries found in this step clearly indicate the problem QuantumDock solves. Namely that biomolecules have multiple binding site for strong hydrogen bond interactions, but one tends to be the strongest, i.e. the ground state energy (Supplementary Fig. 1). This is especially made evident by looking at molecularly electrostatic potential calculations, which are traditionally used to indicate where highly charged areas are on a molecule, hence locations where hydrogen bond formation is likely (Supplementary Fig. 2). Results quantify the complex nature of biomolecules with each biomolecule having multiple highly charged areas. Monomers tend to bind to a particular functional group on biomolecules, but this exact functional group and pose between two molecules is only determined with certainty after conducting an exhaustive docking procedure.

Using the QuantumDock framework we can calculate accurate ground state binding energies between various targets/interferences and potential monomers (Supplementary Fig. 4). Energies calculated using the QuantumDock method show high reproducibility with final binding energies being found repeatedly within less than 0.1 kJ mol-1, which can be attributed to the underlying precision of the ORCA software (Supplementary Fig. 5). This indicates QuantumDock finds the same binding geometry to be the most stable repeatedly, which builds our confidence that this is indeed the true ground state, hence enabling us to calculate reliable binding energies between many biomolecules and monomers of interest. QuantumDock's capabilities can be easily extended to solvation calculations, in which the binding energy between two molecules is calculated in a solvent solution rather than vacuum (Supplementary Fig. 8). A clear trend seen from these calculations shows that binding energies tend to increase in strength with decreasing dielectric constant of the solvent used, hence motivating our choice of methanol for our polymerization solvent. Stronger binding energies in the pre-polymerized solution enable a more stable target-monomer complex which has a higher likelihood of surviving the polymerization process and making a well-defined imprinted site in the subsequent MIP.

Methods Materials and reagents:

Potassium ferricyanide (CAS No. 13746-66-2) and nickel(II) acetate tetrahydrate (CAS No. 6018-89-9) were purchased from Acros Organics. Trisodium citrate dihydrate (CAS No. 6132-04-3), phenylalanine (CAS No. 63-91-2), tryptophan (CAS No. 73-223), leucine (CAS No. 61-90-5), alanine (CAS No. 56-41-7), isoleucine (CAS No. 73-32-5), methionine (CAS No. 63-68-3), valine(CAS No. 72-18-4), acetonitrile (CAS No. 75-05-8), 3aminophenylboronic acid (CAS No. 30418-59-8), aniline (CAS No. 62-53-3), pyrrole (CAS No. 109-97-7), acrylamide (CAS No. 79-06-1), methacrylic acid (CAS No. 79-41-4), 4-vinylbenzoic acid (CAS No. 1075-49-6), o-phenylenediamine (CAS No. 95-54-5), 1,2-ethanediol (12E, CAS NO. 107-21-1), acrylic acid (ACA, CAS NO. 79-10-7), phenol (PHN, CAS NO. 203-632-7), 2vinylpyridine (2VP, CAS NO. 100-69-6), and 2-aminophenol (2AM, CAS NO. 100-69-6) were purchased from Sigma-Aldrich. L-tyrosine (CAS No. 60-18-4) and iron(III) chloride (CAS No. 7705-08-0) were purchased from Alfa Aesar. Acetic acid (CAS No. 64-19-7), methanol (CAS No. 67-56-1), and sodium chloride (CAS No. 7647-14-5) were purchased from Thermo Fisher Scientific. Medical adhesives were purchased from 3 M and Adhesives Research. Polyimide (PI) films (75 µm thick) were purchased from DuPont. PET films (12 µm thick) were purchased from McMaster-Carr. Synthesis of the NiHCF particles. Nickel(II) acetate tetrahydrate (37.25 mg, 149.75 µmol) and trisodium citrate dihydrate (66 mg, 224.5 µmol) were dissolved in 5 mL of water and was injected (20.0 mL min-1) into 5 mL of potassium hexacyanoferrate(III) (32.75 mg, 99.25 µmol) aqueous solution. The reaction was carried out under room temperature (22 ºC) for 24 h and then centrifuged at 10000 revolutions per minute (rpm) for 10 minutes with centrifuge (Eppendorf Centrifuge 5424). The supernatant was discarded, and the precipitated nanoparticles were rinsed with water (4x30 mL). Subsequently, they were redispersed in water (Vortex mixer) and the centrifugation step was repeated at least three times. The resulting orange solution in water was kept under 4 °C for further use. Fabrication and preparation of the laser-engraved graphene (LEG) sensors: The LEG electrodes were fabricated following our previous report on a PI film with a 50 W CO2 laser cutter (Universal Laser System).[1] The optimized parameters for the graphene electrodes and electronic connections were power 8%, speed 15%, and points per inch (PPI) 1,000 in raster mode with three time scan. The reference electrode, Ag was electrodeposited onto the LEG directly with electrochemical workstation (CHI 840D) with multi-current steps at −0.01 mA for 150 s, −0.02 mA for 50 s, −0.05 mA for 50 s, −0.08 mA for 50 s and −0.1 mA for 200 s using a plating solution containing 0.25 M silver nitrate, 0.75 M sodium thiosulfate and 0.5 M sodium bisulfite; 0.1 M FeCl3 in 0.1 M HCl solution was further dropped on the Ag surface for 30 s and washed the solution with water; then 1.5 µL reference cocktail prepared by dissolving 79.1 mg of polyvinyl butyral and 50 mg of NaCl in 1 ml of methanol was dropped on the Ag/AgCl electrode and dried overnight. The Na+ working electrode was prepared as follows: Na+-selective membrane cocktail was first prepared by dissolving 1 mg of Na ionophore X, 0.55 mg sodium tetrakis[3,5bis(trifluoromethyl)phenyl]borate, 33 mg polyvinyl chloride and 65.45 mg bis(2-ethylhexyl) sebacate into 660 µL of tetrahydrofuran; 0.6 µL cocktail was drop-casted onto the LEG electrode and dried overnight. To obtained Na+ sensor was conditioned overnight in 100 mM NaCl before use. The pH sensor was fabricated by electro-polymerization of 0.1 M aniline in 0.1 M HCl aqueous solution through 100 segments of cyclic voltammetry (-0.2 to 1 V at a scan rate of 50 mV s-1). To prepare the Phe MIP sensor, 1 µL of the NiHCF particle dispersion was firstly drop casted onto the surface of LEG electrode, and dried under 90 °C for 5 h, then, the Phe selective MIP membrane is synthesized by electro-polymerization. The polymerization solution was prepared by dissolving 5 mM Phe molecular as template, 20 mM of different monomers in 95% of 0.01 M phosphate-buffered saline (PBS) (pH 6.5) and 5% acetonitrile. The Phe imprinted polymer was electrochemically polymerized on the NiHCF modified LEG electrode with CV deposition using the prepared polymerization solutions. The Phe template molecules were extracted by soaking the electrode into an acetic acid/methanol mixture (7:3 v/v) for 1 h. Subsequently, the LEG-NiHCFMIP was rinsed with distilled water and conditioned in air and room temperature (22 °C) overnight. Subsequently, the LEG-NiHCF-MIP was immersed into a phosphate buffer solution for repetitive CV scans (0 to 0.8 V with a scan rate of 50 mV s-1) until a stable response was obtained. MIP nanoparticles (NPs) synthesis and characterization. MIP NPs were fabricated and characterized with ultraviolet–visible spectroscopy (UV-vis) (Thermo Scientific NanoDrop) to experimentally confirm our computational results. All MIP NPs were fabricated using a standardized experimental procedure described as follows (except the use of different monomer/crosslinker for a specific type of MIP NPs). The target molecule Phe was added along with the monomer of choice (pyrrole, methylacrylic acid, acrylamide, or 4-vinylbenzoic acid) in 10 mL 1:4 deionized-water:methanol (v:v) and mixed until completely dissolved. 40 mM of crosslinker (divinylbenzene, butyl methacrylate, or ethylene glycol dimethylacrylate) was then added and mixed until dissolved. 25 mM of initiator (azobisisobutyronitrile) was then added to solution and the container is purged with nitrogen for 10 minutes at low pressure to avoid decarboxylation. The polymerization was then started by water bath at 60 °C for 5 hours. Extraction of the template then took place by adding 5 mL acetic acid:methanal (7:3 v/v) and stirring overnight. The following day the particle solution was then washed with water 3 times at 7000 rpm for 2 minutes at a time, then washed one more time with methanol at 7000 rpm for 2 minutes and dried at 30 °C until dry. The dried particles were then crushed by a probe sonicator (CGOLDENWALL) to a fine powder (around 100 nm in diameter) for subsequent testing. Materials characterization. The morphology of materials was characterized by field-emission scanning electron microscopy (SEM, Nova 600). Energy-dispersive X-ray spectroscopy (EDS) analyses were performed using a JEOL JEM-ARM300CF S/STEM system (300 keV). Characterization of the LEG sensor performance. A set of electrochemical sensors were characterized in solutions of target analytes. All the in vitro sensor characterizations were performed through CHI 840D. The response of pH sensor was characterized with open circuit potential measurements in the standard McIlvaine’s buffer solutions with different pH value. The response of the Na+ sensor was characterized with open circuit potential measurements in the solutions containing varied Na+ levels. DPV analysis was performed for all the LEG-NiHCF-MIP PHE sensor characterizations in 0.01 M PBS (pH 6.5) or in raw sweat. The negative DPV condition were as follows: 0.8 to 0 V; incremental potential, 0.01 V; pulse amplitude, 0.05 V; pulse width, 0.05 s; pulse period, 0.5 s; and sensitivity, 1 × 10−5 A V−1. For in situ sweat analyte measurement, background and signal curves were recorded before and after incubation; the signal current was obtained as the difference of the peak amplitudes between the post-incubation signal and the background current curves. Fabrication and characterization of microfluidic channels. The microfluidic module was fabricated using a 50 W CO2 laser cutter (Universal Laser System).[1] Briefly, layers of doublesided and single-sided medical adhesives (3M) were patterned with channels, inlets, the iontophoresis gel outlines and reservoirs. For all microfluidic layers, the iontophoresis gel outlines were patterned to enable the current flow from the top PI electrode layer. The bottom layer, which 10 mL 1:4 deionized-water:methanol (v:v) and mixed until completely dissolved. 40 mM of crosslinker (divinylbenzene, butyl methacrylate, or ethylene glycol dimethylacrylate) was then added and mixed until dissolved. 25 mM of initiator (azobisisobutyronitrile) was then added to solution and the container is purged with nitrogen for 10 minutes at low pressure to avoid decarboxylation. The polymerization was then started by water bath at 60 ºC for 5 hours. Extraction of the template then took place by adding 5 mL acetic acid:methanal (7:3 v/v) and stirring overnight. The following day the particle solution was then washed with water 3 times at 7000 rpm for 2 minutes at a time, then washed one more time with methanol at 7000 rpm for 2 minutes and dried at 30 ºC until dry. The dried particles were then crushed by a probe sonicator (CGOLDENWALL) to a fine powder (around 100 nm in diameter) for subsequent testing. Materials characterization. The morphology of materials was characterized by field-emission scanning electron microscopy (SEM, Nova 600). Energy-dispersive X-ray spectroscopy (EDS) analyses were performed using a JEOL JEM-ARM300CF S/STEM system (300 keV). Characterization of the LEG sensor performance. A set of electrochemical sensors were characterized in solutions of target analytes. All the in vitro sensor characterizations were performed through CHI 840D. The response of pH sensor was characterized with open circuit potential measurements in the standard Mcllvaine's buffer solutions with different pH value. The response of the Na+ sensor was characterized with open circuit potential measurements in the solutions containing varied Na+ levels. DPV analysis was performed for all the LEG-NiHCF-MIP PHE sensor characterizations in 0.01 M PBS (pH 6.5) or in raw sweat. The negative DPV condition were as follows: 0.8 to 0 V; incremental potential, 0.01 V; pulse amplitude, 0.05 V; pulse width, 0.05 s; pulse period, 0.5 s; and sensitivity, 1 × 10−5 A V−1. For in situ sweat analyte measurement, background and signal curves were recorded before and after incubation; the signal current was obtained as the difference of the peak amplitudes between the post-incubation signal and the background current curves. Fabrication and characterization of microfluidic channels. The microfluidic module was fabricated using a 50 W CO2 laser cutter (Universal Laser System).[1] Briefly, layers of doublesided and single-sided medical adhesives (3M) were patterned with channels, inlets, the iontophoresis gel outlines and reservoirs. For all microfluidic layers, the iontophoresis gel outlines were patterned to enable the current flow from the top PI electrode layer. The bottom layer, which the digital-to-analogue converter (DAC) (DAC8552, Texas Instruments) over a serial peripheral interface to set the control voltage of the current source. The current source output is checked by a comparator (TS391, STMicroelectronics), and the microcontroller is interrupted through its general-purpose input/output pin at output failure. The protection circuit consists of a current limiter (MMBF5457, ON Semiconductor) and analogue switches (MAX4715, Maxim Integrated; ADG5401, Analog Devices). The microcontroller's general-purpose input/output is also used to enable or disable the iontophoresis circuit. For the optimized design, a 100-μA current (~2.6 μA mm−2) was applied for on-body iontophoresis sweat induction using the flexible microfluidic patch. Sweat sensing. The sweat sensing circuitry can perform DPV, as well as potentiometric and temperature measurements. A potentiostat circuit is constructed by a control amplifier and a transimpedance amplifier (AD8606, Analog Devices). A series voltage reference (ISL60002, Renesas Electronics) and a DAC (DAC8552, Texas Instruments) is used to generate a dynamic potential bias across the reference and working electrode. Two instrumentation amplifiers (INA333, Texas Instruments) are used for potentiometric measurements, and a voltage divider is used for the resistive temperature sensor. All analogue voltage signals are acquired by the microcontroller's built-in analogue-to-digital converter (ADC) channels, processed and then transmitted over Bluetooth to a user device. Human subject recruitment. The validation and evaluation of the sweat sensor were performed using human subjects in compliance with all the ethical regulations under protocols (ID: 19-0892) that were approved by the institutional review board at California Institute of Technology (Caltech). The participating subjects (aged over 18 years) were recruited from Caltech campus through advertisement. All subjects gave written informed consent before study participation. For wearable sensor evaluation, healthy subjects with a body mass index (BMI) of 18.5– 24.9 kg m−2 with fasting serum glucose <100 mg dl−1 were recruited. GC–MS analysis for sensor validation. GC–MS analysis of the PHE in the collected sweat samples was performed using EZ:Faast kit from Phenomenex, which enables sample preparation, derivatization and GC–MS analysis of free AAs. A Varian Saturn 2000 was used for the GC–MS runs. One microlitre of prepared sample solution was injected for GC in helium carrier gas at 1.0 ml min−1 constant flow with a pulse pressure of 20 pounds per square inch for 0.2 min, with the oven programmed from 110 °C to 320 °C at 32 °C min−1. The mass chromatography was set with source at 240 °C, quad at 180 °C and auxiliary at 310 °C with a scan range of 45–450 m/z at a sampling rate of 3.5 scans s−1. Selected ion monitoring was used, which records the ion current at selected masses that are characteristic of the certain AA in an expected retention time. The internal standard (IS; norvaline) was added during the sample derivatization process to account for potential evaporation-induced increase in peak detection; the IS norvaline peak height is recorded at its ion number 158 at 1.65 min. The PHE peak height recorded from raw data spectrum was calibrated with respect to the IS in the same run: normalized PHE peak height = PHE peak height/ IS peak height. With normalized peak heights of different levels of PHE standards, calibration plots were constructed. System evaluation with PHE supplement intake. For on-body test, the subjects reported to the lab after fasting overnight. The subjects' arms were cleaned with alcohol swabs and gauze before the sensor patches were placed on the body. The subjects were provided PHE supplement (1 g each) for the intake study. In contrast, the control study was performed on the subjects without any supplementary intake. Five-minute iontophoresis was applied on the subjects. During the on-body trial, the data from the sensor patches were wirelessly sent to the user interface via Bluetooth. When the subjects started sweating, the sensor system continuously acquired and transmitted pH, sodium and temperature sensor data. Every minute, the electronic system initiated a transient voltage bias between the reference and working electrodes. When the bias triggered a current above an experimentally determined threshold, the system would start a CV cleaning cycle and then the first DPV scan as the initial background without target incubation. The DPV scan was repeated 7 min later as the post-incubation curve. Between the two scans, pH and sodium sensor data were continuously recorded while the temperature was continuously recorded throughout the whole testing. Right after the post-incubation DPV, another cycle started with an IT cleaning/regeneration step, followed by an initial background DPV scan. The collected pH, sodium and DPV data were wirelessly transmitted to a user device via Bluetooth in real time, where the molecular data were extracted, calibrated and converted to concentration levels.

Statistical Analysis.

For UV-vis-based molecular absorption (Fig. 3e and Supplementary Fig. 9), maximum adsorption amount (Qe) (Fig. 3f–i), and selectivity study (Fig. 3j,k and Supplementary Fig. 9), all the error bars represent the s.d calculated from three measurements. The fitting curves in Supplementary Figs. 9 and 10 represent trendlines obtained via linear oven programmed from 110 °C to 320 °C at 32 °C min^{-1}.

The mass chromatography was set with source at 240 °C, quad at 180 °C and auxiliary at 310 °C with a scan range of 45–450 m/z at a sampling rate of 3.5 scans s−1. Selected ion monitoring was used, which records the ion current at selected masses that are characteristic of the certain AA in an expected retention time. The internal standard (IS; norvaline) was added during the sample derivatization process to account for potential evaporation-induced increase in peak detection; the IS norvaline peak height is recorded at its ion number 158 at 1.65 min. The PHE peak height recorded from raw data spectrum was calibrated with respect to the IS in the same run: normalized PHE peak height = PHE peak height/ IS peak height. With normalized peak heights of different levels of PHE standards, calibration plots were constructed. System evaluation with PHE supplement intake. For on-body test, the subjects reported to the lab after fasting overnight. The subjects' arms were cleaned with alcohol swabs and gauze before the sensor patches were placed on the body. The subjects were provided PHE supplement (1 g each) for the intake study. In contrast, the control study was performed on the subjects without any supplementary intake. Five-minute iontophoresis was applied on the subjects. During the on-body trial, the data from the sensor patches were wirelessly sent to the user interface via Bluetooth. When the subjects started sweating, the sensor system continuously acquired and transmitted pH, sodium and temperature sensor data. Every minute, the electronic system initiated a transient voltage bias between the reference and working electrodes. When the bias triggered a current above an experimentally determined threshold, the system would start a CV cleaning cycle and then the first DPV scan as the initial background without target incubation. The DPV scan was repeated 7 min later as the post-incubation curve. Between the two scans, pH and sodium sensor data were continuously recorded while the temperature was continuously recorded throughout the whole testing. Right after the post-incubation DPV, another cycle started with an IT cleaning/regeneration step, followed by an initial background DPV scan. The collected pH, sodium and DPV data were wirelessly transmitted to a user device via Bluetooth in real time, where the molecular data were extracted, calibrated and converted to concentration levels. Statistical Analysis. For UV-vis-based molecular absorption (Fig. 3e and Supplementary Fig. 9), maximum adsorption amount (Qe) (Fig. 3f–i), and selectivity study (Fig. 3j,k and Supplementary Fig. 9), all the error bars represent the s.d calculated from three measurements. The fitting curves in Supplementary Figs. 9 and 10 represent trendlines obtained via linear

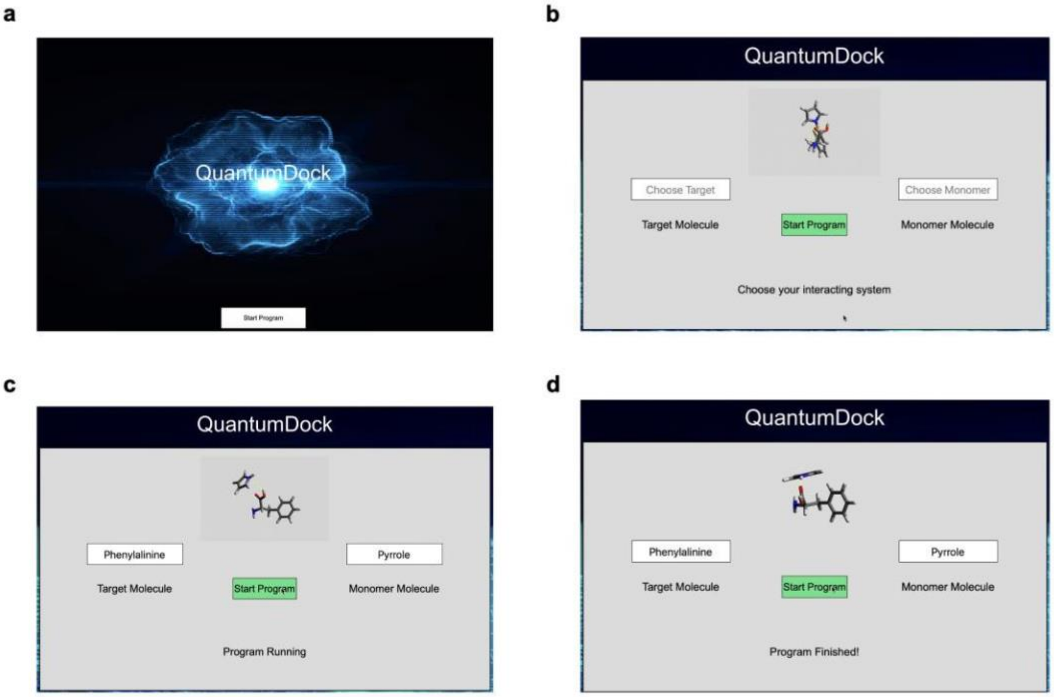

Figure A-1: The graphical user interface (GUI) of the QuantumDock.

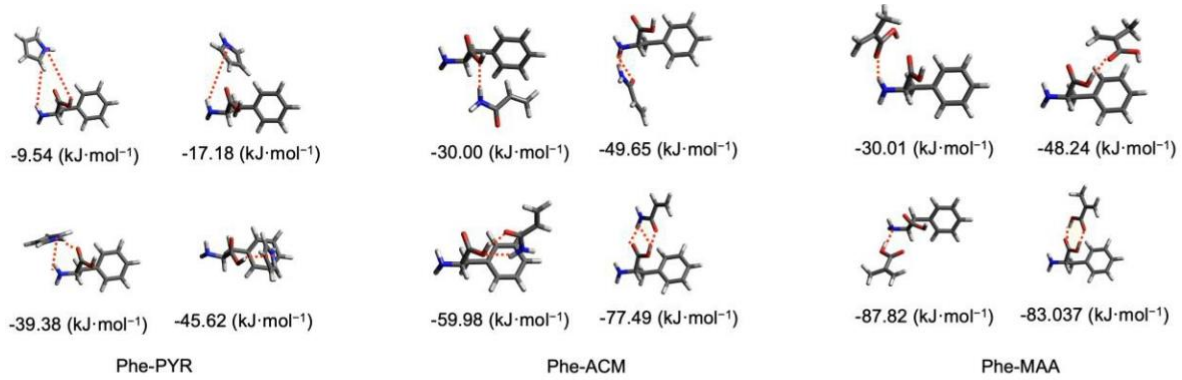

Figure A-2: The hydrogen bonds and calculated Phe-monomer binding energy

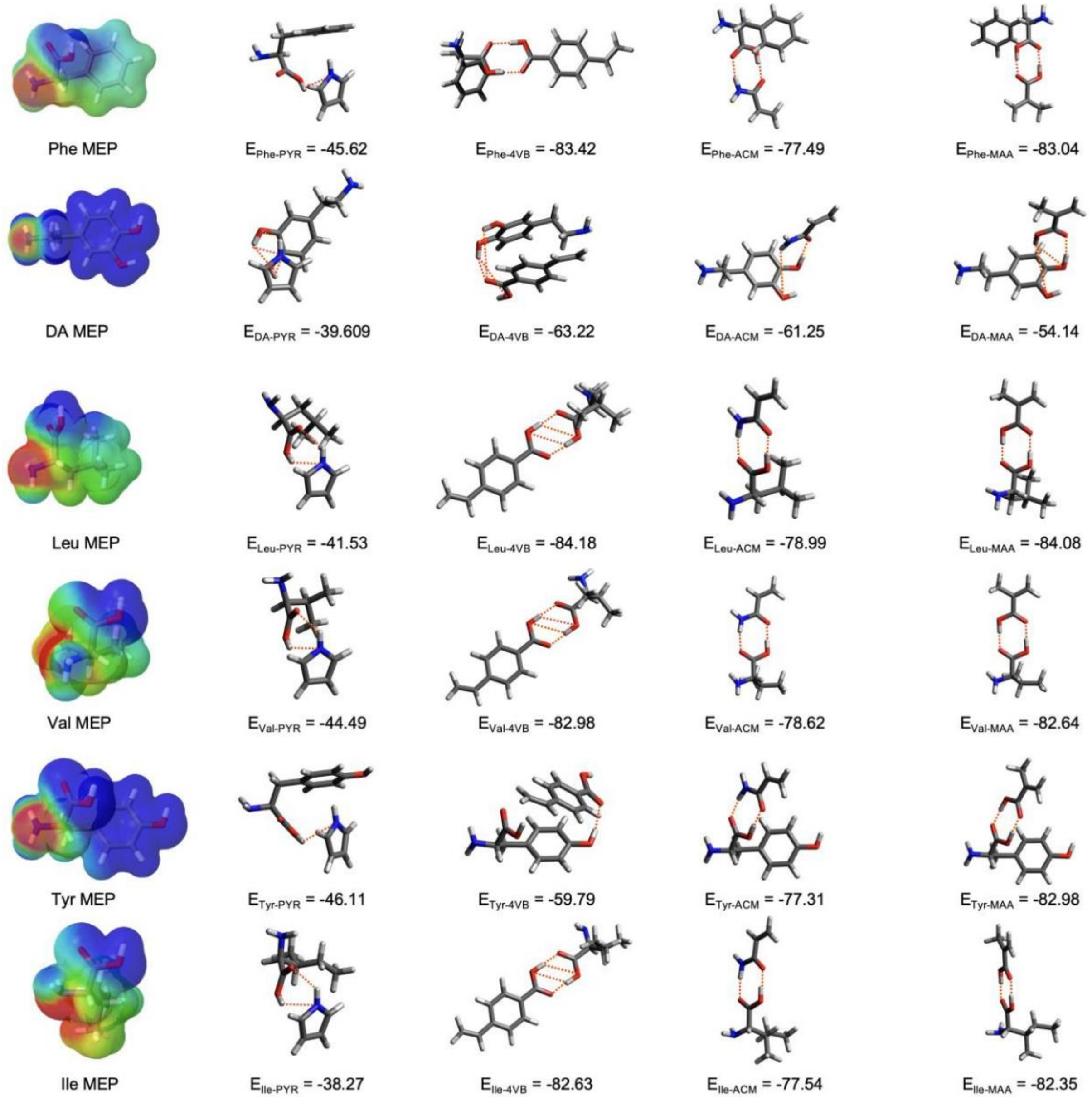

Figure A-3: Molecular electrostatic potential (MEP) calculations of 7 targets/interference molecules. Unit, kJ·mol^{-1}.

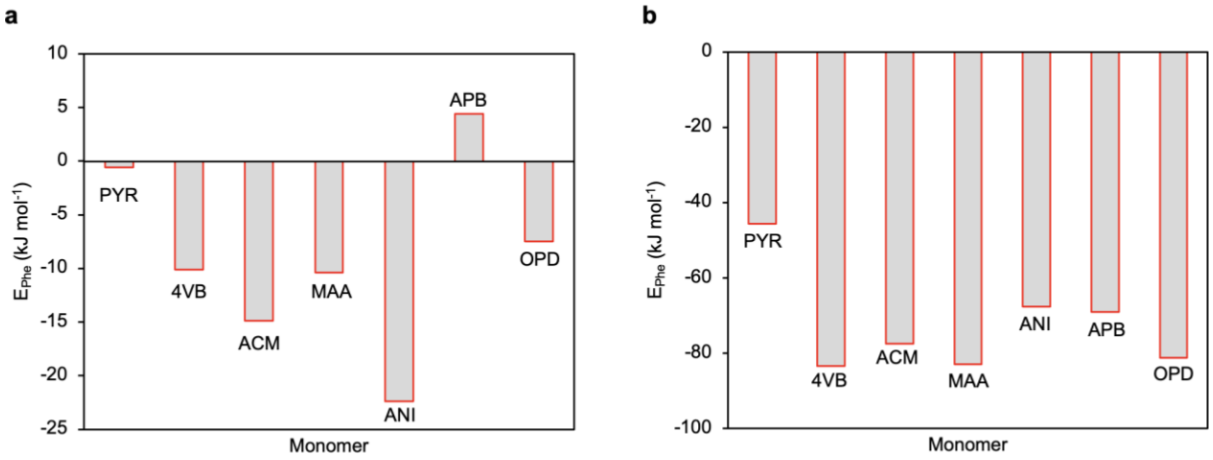

Figure A-4: Binding energies between 7 monomers and Phe using semiempirical theory and DFT.

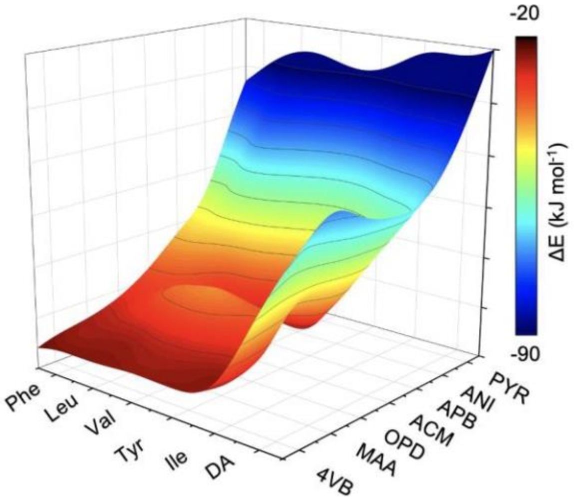

Figure A-5: DFT-calculated binding energy of Phe-monomer and interferent- monomer.

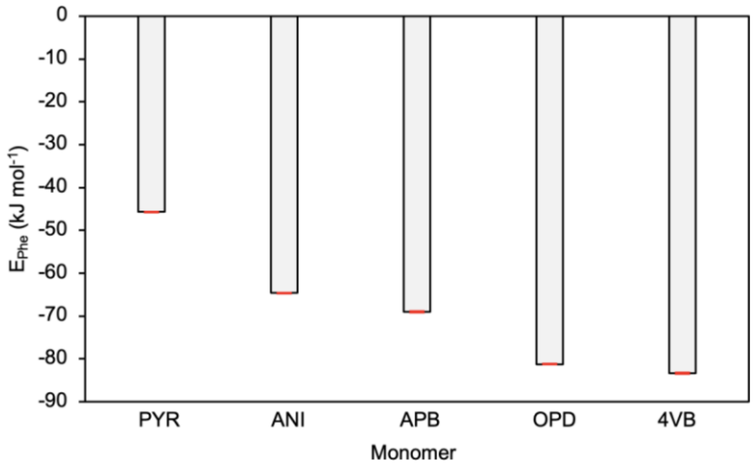

Figure A-6: Reproducibility of the QuantumDock framework. All error bars represent the s.d. from three trials.

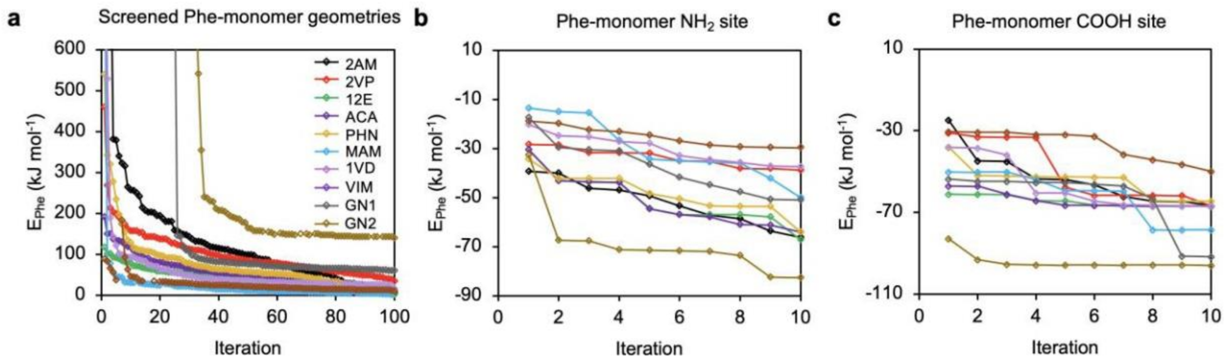

Figure A-7: QuantumDock-based computational Phe MIP optimization using less commonly used monomers. a, Semiempirical energy calculations based on 100 docked monomer-Phe complexes for each monomer. 2AM, 2-aminophenol; 2VP, 2-vinylpyridine; 12E, 1,2-ethanediol; ACA, acrylic acid; PHN, phenol; MAM, methacrylamide; 1VD, vinyl acetate; VIM, 1-vinylimidazole; GN1 and GN2, two molecules generated by the Generative Examination Networks (GEN) as shown in **Supplementary Fig. 9**. **b,c**, DFT energy calculations on the most stable screened molecules based on Phe-monomer NH2 site (**b**) and Phe-monomer COOH site (**c**).

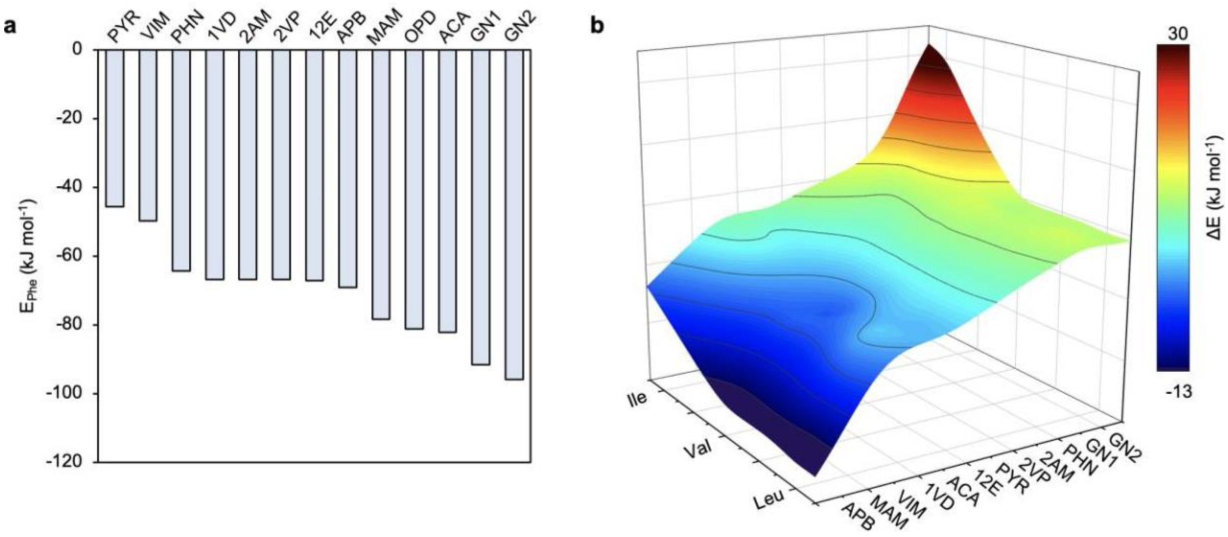

Figure A-8: QuantumDock-calculated binding energy and binding energy differences. a, DFT-calculated binding energy of Phe-monomer. **b,** Colored mapping of the binding energy differences between Phe-monomer and interference-monomer complexes. Three other amino acids including Leu, Ile, and Val were used as the interference molecules.

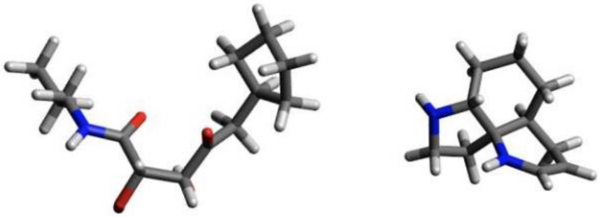

GN1: $C_{13}O_4NH_{23}$ GN2: $C_{11}N_2H_{18}$

Figure A-9: **GN1 and GN2, two molecules generated by the GEN.**

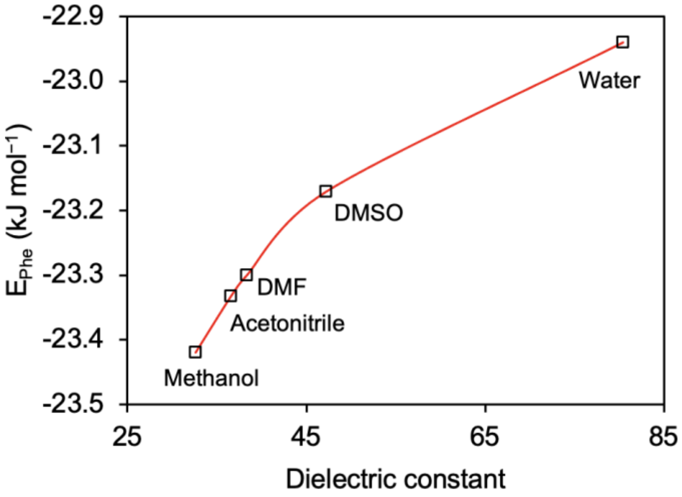

Figure A-10: Phe-PYR binding energies calculated in varying solvents. DMF, dimethylformamide; DMSO, dimethyl sulfoxide.

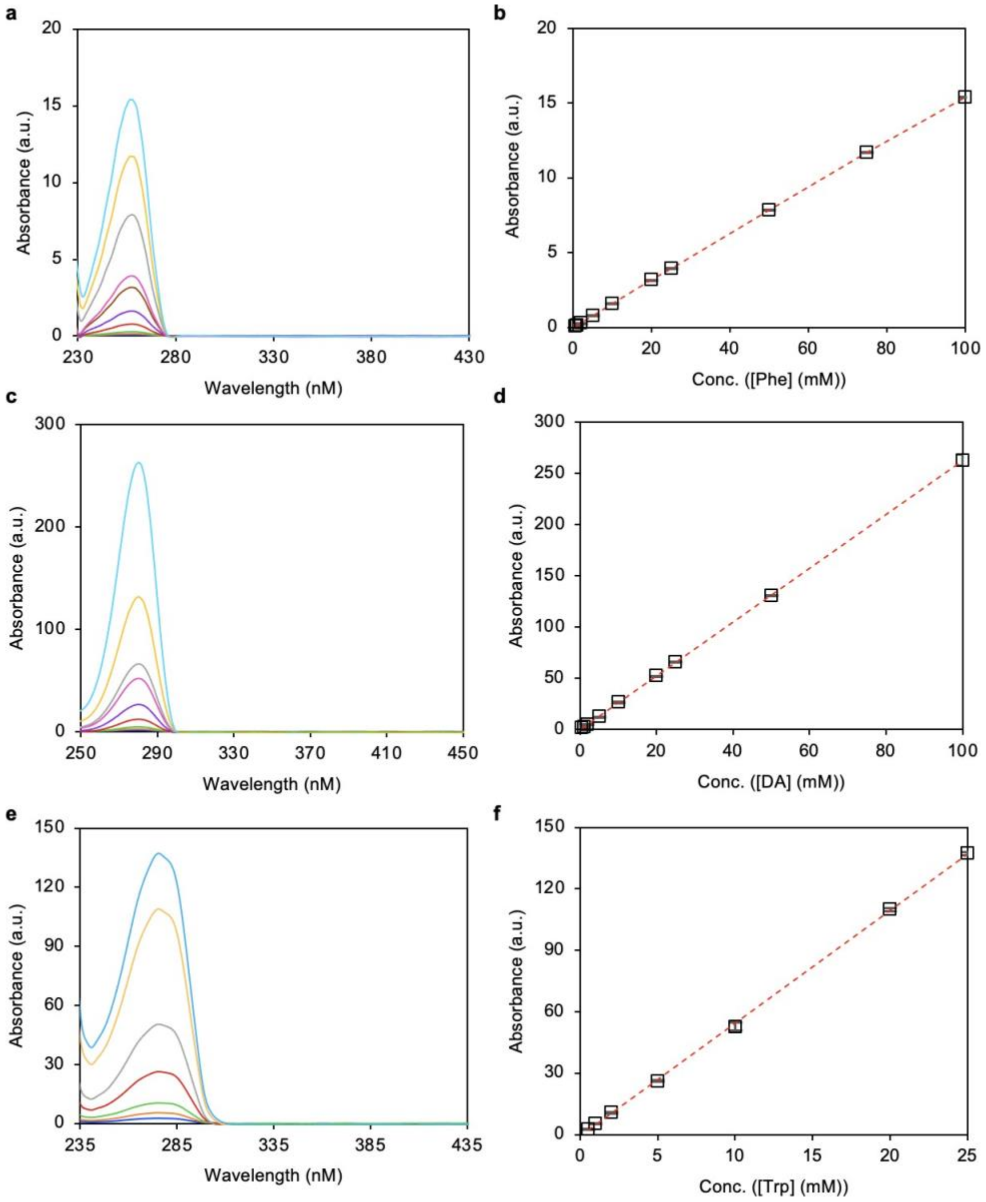

Figure A-11: Calibrations of the studied target and interferent molecules in solutions with varied concentrations using UV-Vis. All error bars represent the s.d. from three measurements.

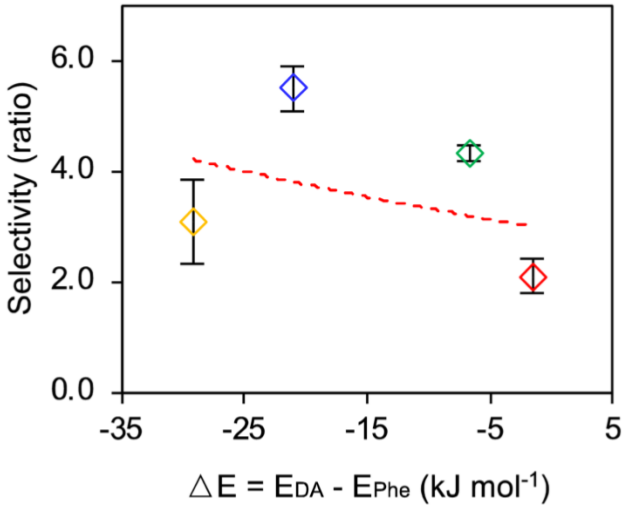

Figure A-12: Selectivity of Phe MIP NPs based on different monomers over interferent DA based on intermediate state. All error bars represent the s.d. from three measurements.

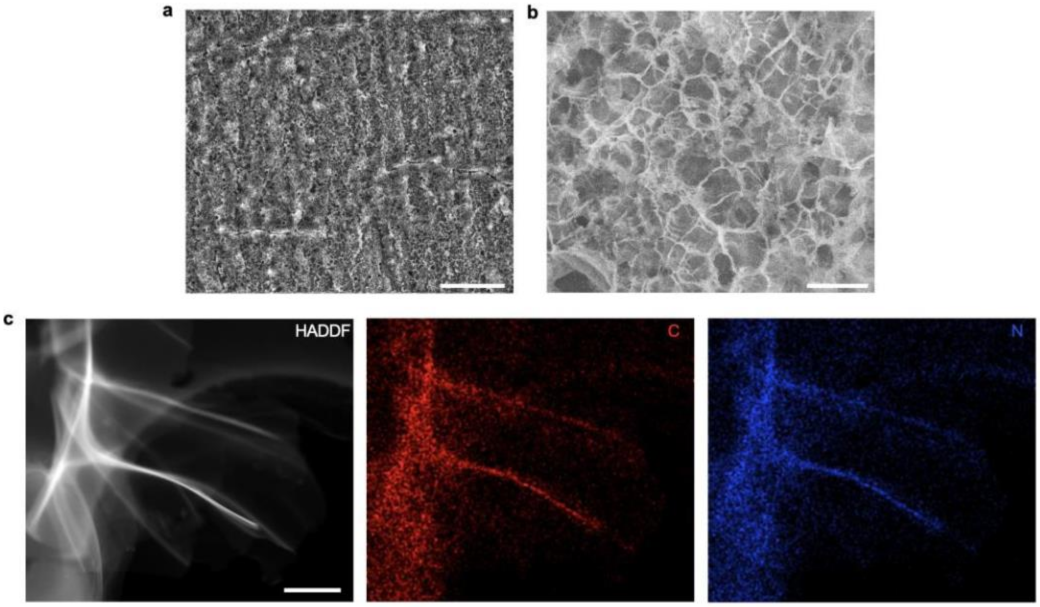

Figure A-13: Microscopic characterization of the laser-engraved graphene (LEG). a,b, Scanning electron microscope (SEM) images of the LEG. Scale bars, 200 and 10 µm for **a** and **b**, respectively. **c,** High-angle annular dark-field scanning transmission electron microscopy (HAADF-STEM) and element mapping images of the LEG. Scale bar, 1 µm.

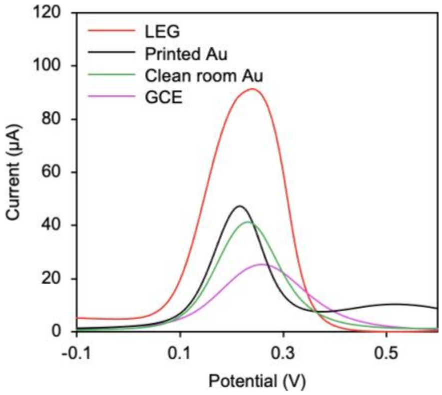

Figure A-14: Electrochemical characterization of the LEG electrode. Differential pulse voltammetry (DPV) of an LEG electrode, a glassy carbon electrode (GCE), a inkjet-printed Au electrode, and a cleanroom evaporated Au electrode in a solution containing 5 mM $[Fe(CN)6]^{3-}$ and 0.2 M KCl.

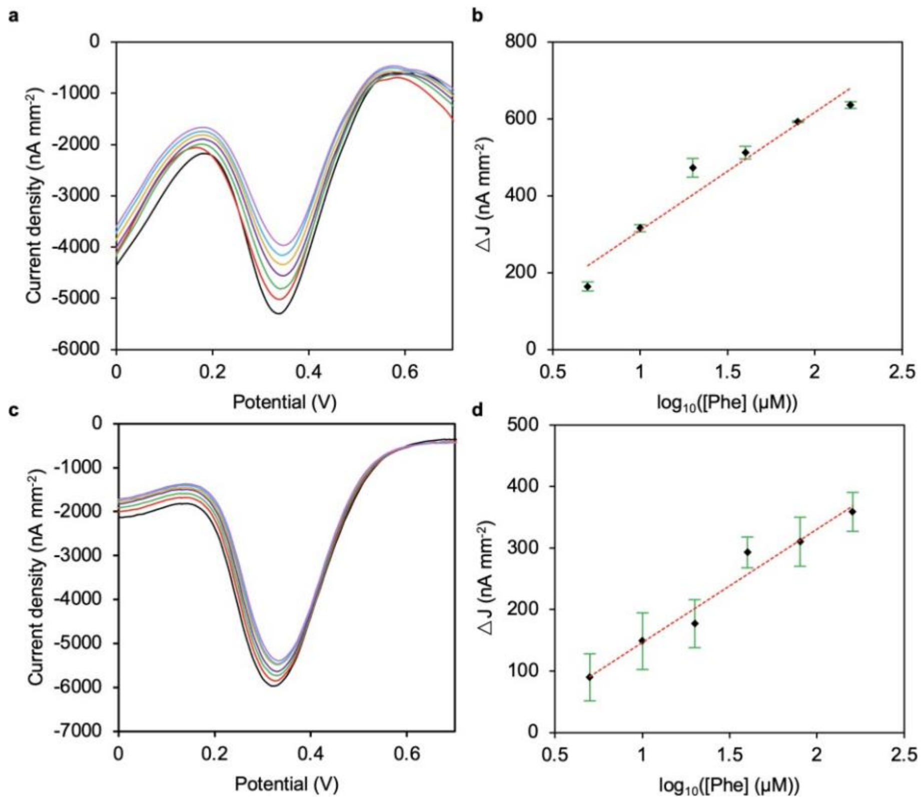

Figure A-15: Calibrations of the electrochemical Phe sensors prepared with APB and PYR. a,b, DPV voltammograms (**a**) and the corresponding calibration curves (**b**) of Phe detection using APB as the monomer. **c,d,** DPV voltammograms (**c**) and the corresponding calibration curves (**d**) of Phe detection using PYR as the monomer. ΔJ, peak height difference of the current density. All error bars represent the s.d. from three sensors.

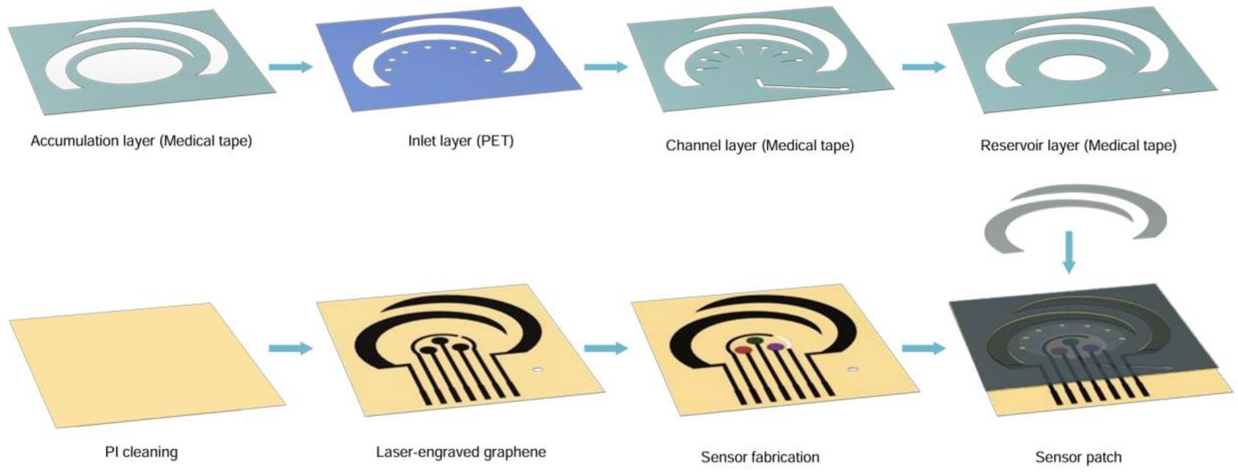

Figure A-16: **Fabrication process of the multifunctional flexible wearable sensor patch.**

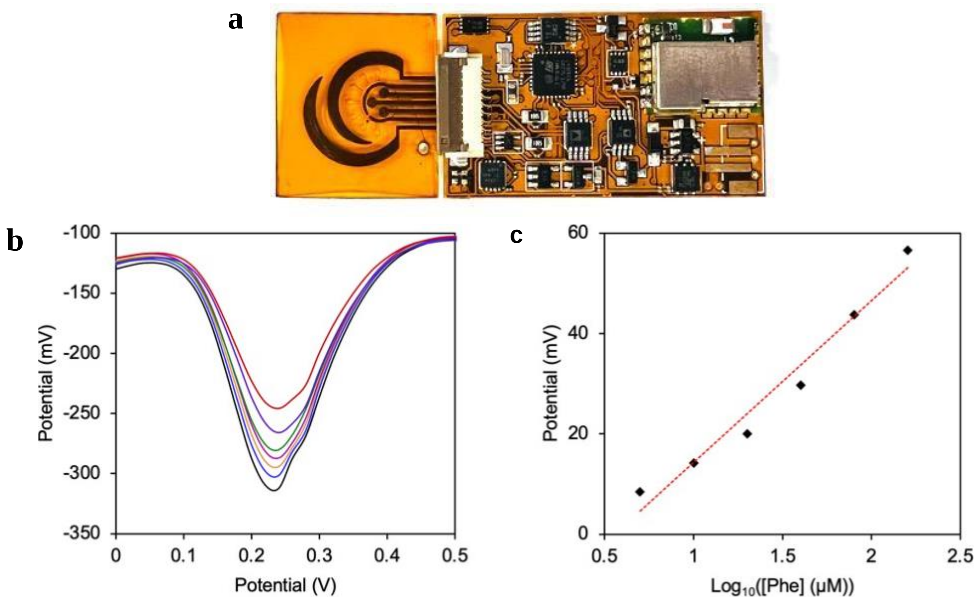

Figure A-17: The fully integrated wireless wearable system. a, Image of the wearable system. The wearable sensor consisting of a flexible, disposable microfluidic sensor patch and a flexible printed circuit board. **b,c,** Calibration plot for Phe analysis using the integrated system.

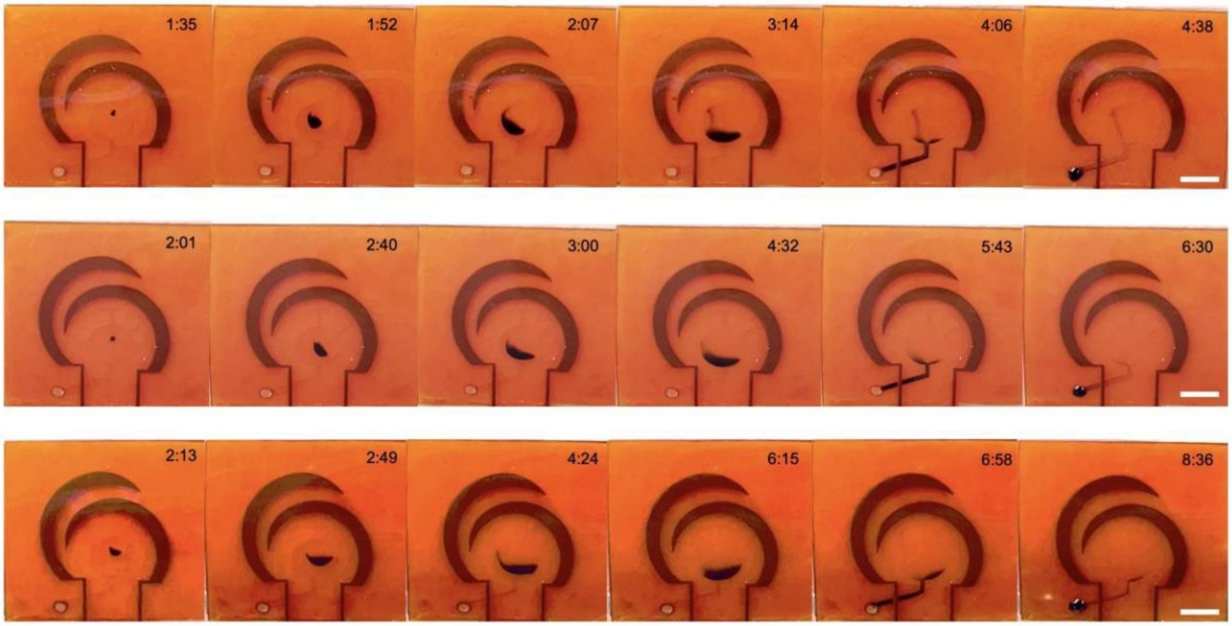

Figure A-18: On-body evaluation of the microfluidic flexible sensor patches for carbagel based iontophoretic sweat stimulation and sampling at rest. Timestamps represent the period (min) after a 5-min iontophoresis session. Black dye was used in the reservoir to facilitate the direct visualization of sweat flow in the microfluidics. Scale bars, 3 mm.

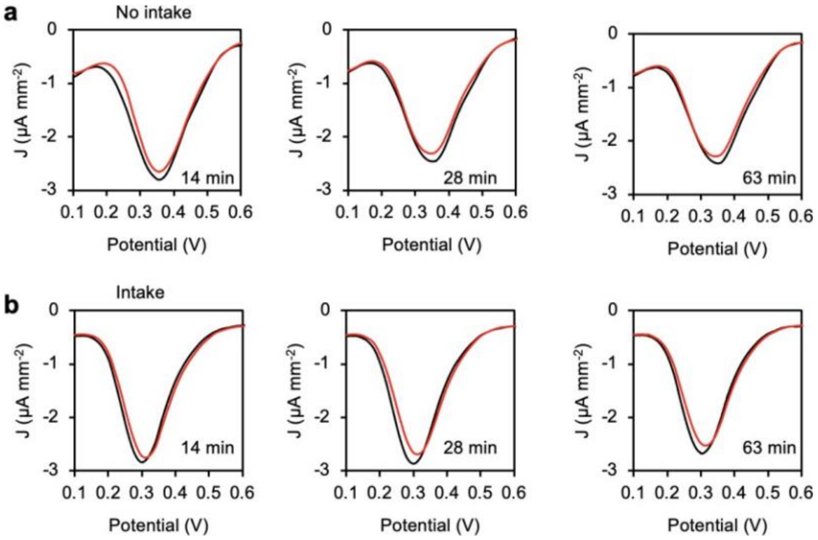

Figure A-19: **DPV signal recorded during the on-body Phe monitoring in a healthy subject without intake (a) and after intake (b) at 14, 28, and 63 minutes.**

Supplementary Table 1. **Comparison of the QuantumDock with transitional semiempirical and density functional theory approaches for MIP design.** BSSE, basis set superposition error; gCP, geometric counterpoise correction.

Approach	Sensitivity	Selectivity	Crosslinker optimization	Molecular docking	Molecules validated	Performance discussions
Semiempirical[15–24]	Yes	No	No	No	0[15–18] 1[19–22] 3[23,24]	Significantly outdated
Density Functional Theory[25–31]	Yes	No	No	No	0[25–29] 3[30,31]	Poor accuracy on crosslinkers Poor accuracy on large systems (no BSSE or outdated)
QuantumDock	Yes	Yes	Yes	Yes	19	Modern dispersion corrections (D3) Modern BSSE correction (gCP) Rigorous docking (Low systematic error)

APPENDIX A BIBLIOGRAPHY

[1] M. Wang, Y. Yang, J. Min, Y. Song, J. Tu, D. Mukasa, C. Ye, C. Xu, N. Heflin, J. S. McCune, T. K. Hsiai, Z. Li, W. Gao, Nat. Biomed. Eng. 2022, 6, 1225.

[2] S. A. FitzGerald, D. Mukasa, K. H. Rigdon, N. Zhang, B. R. Barnett, J. Phys. Chem. C 2019, 123, 30427.

[3] M. Liu, L. Zhang, M. A. Little, V. Kapil, M. Ceriotti, S. Yang, L. Ding, D. L. Holden, R. Balderas-Xicohténcatl, D. He, R. Clowes, S. Y. Chong, G. Schütz, L. Chen, M. Hirscher, A. I. Cooper, Science 2019, 366, 613.

[4] H. Wang, M. Wang, X. Liang, J. Yuan, H. Yang, S. Wang, Y. Ren, H. Wu, F. Pan, Z. Jiang, Chem. Soc. Rev. 2021, 50, 5468.

[5] J. Y. Kim, H. Oh, H. R. Moon, Adv. Mater. 2019, 31, 1805293.

[6] M. Lozada-Hidalgo, S. Zhang, S. Hu, A. Esfandiar, I. V. Grigorieva, A. K. Geim, Nat. Commun. 2017, 8, 15215.

[7] I. Weinrauch, I. Savchenko, D. Denysenko, S. M. Souliou, H.-H. Kim, M. Le Tacon, L. L. Daemen, Y. Cheng, A. Mavrandonakis, A. J. Ramirez-Cuesta, D. Volkmer, G. Schütz, M. Hirscher, T. Heine, Nat. Commun. 2017, 8, 14496.

[8] S. K. Ujjain, A. Bagusetty, Y. Matsuda, H. Tanaka, P. Ahuja, C. de Tomas, M. Sakai, F. Vallejos-Burgos, R. Futamura, I. Suarez-Martinez, M. Matsukata, A. Kodama, G. Garberoglio, Y. Gogotsi, J. Karl Johnson, K. Kaneko, Nat. Commun. 2021, 12, 546.

[9] L. Bondorf, J. L. Fiorio, V. Bon, L. Zhang, M. Maliuta, S. Ehrling, I. Senkovska, J. D. Evans, J.-O. Joswig, S. Kaskel, T. Heine, M. Hirscher, Sci. Adv. 2022, 8, eabn7035.

[10] F. J. Sevilla, L. Olivares-Quiroz, Eur. J. Phys. 2012, 33, 709.

[11] Q. Wang, S. R. Challa, D. S. Sholl, J. K. Johnson, Phys. Rev. Lett. 1999, 82, 956.

[12] R. A. Trasca, M. K. Kostov, M. W. Cole, Phys. Rev. B 2003, 67, 035410.

[13] J. J. M. Beenakker, V. D. Borman, S. Yu. Krylov, Chem. Phys. Lett. 1995, 232, 379.

[14] F. Neese, WIREs Comput. Mol. Sci. 2012, 2, 73.

[15] H. Krishnan, K. M. S. Islam, Z. Hamzah, M. N. Ahmad, AIP Conf. Proc. 2017, 1891, 020083. [16] D. C. Apodaca, R. B. Pernites, R. Ponnapati, F. R. Del Mundo, R. C. Advincula, Macromolecules 2011, 44, 6669.

[17] D. C. Apodaca, R. B. Pernites, R. R. Ponnapati, F. R. Del Mundo, R. C. Advincula, ACS Appl. Mater. Interfaces 2011, 3, 191.

[18] B. D. B. Tiu, R. B. Pernites, S. B. Tiu, R. C. Advincula, Colloids Surf. Physicochem. Eng. Asp. 2016, 495, 149.

[19] F. Ahmadi, E. Karamian, Iran. J. Pharm. Res. IJPR 2014, 13, 417.

[20] K. Bartold, Z. Iskierko, P. Borowicz, K. Noworyta, C.-Y. Lin, J. Kalecki, P. S. Sharma, H.Y. Lin, W. Kutner, Biosens. Bioelectron. 2022, 208, 114203.

[21] S. Khan, S. Hussain, A. Wong, M. V. Foguel, L. Moreira Gonçalves, M. I. Pividori Gurgo, M. del P. Taboada Sotomayor, React. Funct. Polym. 2018, 122, 175.

[22] K. Farrington, E. Magner, F. Regan, Anal. Chim. Acta 2006, 566, 60.

[23] M. B. Gholivand, M. Khodadadian, F. Ahmadi, Anal. Chim. Acta 2010, 658, 225.

[24] L. Marestoni, A. Wong, G. Feliciano, M. R. R. Marchi, C. Tarley, M. Sotomayor, J. Braz. Chem. Soc. 2015, 00, 1.

[25] T. D. K. Wungu, S. E. Marsha, Widayani, Suprijadi, IOP Conf. Ser. Mater. Sci. Eng. 2017, 214, 012004.

[26] Y. Li, X. Li, C. Dong, J. Qi, X. Han, Carbon 2010, 48, 3427.

[27] S. Pardeshi, R. Dhodapkar, A. Kumar, Spectrochim. Acta. A. Mol. Biomol. Spectrosc. 2013, 116, 562.

[28] S. Riahi, F. Edris-Tabrizi, M. Javanbakht, M. R. Ganjali, P. Norouzi, J. Mol. Model. 2009, 15, 829.

[29] Q. Li, B. Ling, L. Jiang, L. Ye, Chem. Eng. J. 2018, 350, 217.

[30] W. Dong, M. Yan, M. Zhang, Z. Liu, Y. Li, Anal. Chim. Acta 2005, 542, 186.

[31] Y. Diñeiro, M. I. Menéndez, M. C. Blanco-López, M. J. Lobo-Castañón, A. J. MirandaOrdieres, P. Tuñón-Blanco, Biosens. Bioelectron. 2006, 22, 364.

Chapter 5: A Wearable Electrochemical Biosensor for the Monitoring of metabolites and Nutrients

Materials from this chapter adapted from "Wang, M.; Yang, Y.; Min, J.; Song, Y.; Tu, J.; Mukasa, D.; Ye, C.; Xu, C.; Heflin, N.; McCune, J. S.; Hsiai, T. K.; Li, Z.; Gao, W. A Wearable Electrochemical Biosensor for the Monitoring of Metabolites and Nutrients. Nature Biomedical Engineering 2022, 6, 1225–1235. https://doi.org/10.1038/s41551-022-00932-7"

5.1 Introduction

Circulating nutrients are essential indicators for overall health and body function[1]. Amino acids (AAs), sourced from dietary intake, gut microbiota synthesis, and influenced by personal lifestyles, are important biomarkers for a number of health conditions (**Fig. 5-1a**)[2]. Elevated branched-chain amino acids (BCAAs) including leucine (Leu), isoleucine (Ile), and valine (Val), are associated with obesity, insulin resistance, and the future risk of type 2 diabetes mellitus (T2DM), cardiovascular diseases (CVDs), and pancreatic cancer[3–5]. Deficiencies in AAs (e.g., arginine and cysteine) could hamper the immune system by reducing immune-cell activation[6]. Tryptophan (Trp), tyrosine (Tyr) and phenylalanine (Phe) are precursors of serotonin and catecholamine neurotransmitters (dopamine, norepinephrine, and epinephrine), respectively, and play an important role in the function of complex neural systems and mental health[7,8]. A number of metabolic fingerprints (including Leu, Phe, and vitamin D) are linked to COVID-19 severity[9,10]; health disparities in nutrition also correlate well with the alarming racial and ethnic disparities that are worsened by COVID-19 vulnerability and mortality[11]; moreover, organ and tissue dysfunction induced by SARS-CoV-2 could result in an increased incidence of cardiometabolic diseases[12].

Metabolic profiling and monitoring are a key approach to enabling precision nutrition and precision medicine[13]. Current gold standards in medical evaluation and metabolic testing heavily rely on blood analyses that are invasive and episodic, often requiring physical visits to medical facilities, labor-intensive sample processing and storage, and delicate instrumentation (e.g., gas chromatography-mass spectrometry (GC-MS))[14]. As the current COVID-19 pandemic remains uncontrolled around the world, there is a pressing need for developing wearable and telemedicine sensors to monitor an individual's health state and to enable timely intervention under home- and community-based settings[15–23]; it is also increasingly important to monitor a person's long-term cardiometabolic and nutritional health status after recovery from severe COVID-19 infection using wearables to capture early signs of potential endocrinological complications such as T2DM[12].

Sweat is an important body fluid containing a wealth of chemicals reflective of nutritional and metabolic conditions[24–27]. The progression from blood analyses to wearable sweat analyses could provide great potential for non-invasive, continuous monitoring of physiological biomarkers critical to human health[28-38]. However, currently reported wearable electrochemical sensors primarily focus on a limited number of analytes including electrolytes, glucose, and lactate, due to the lack of a suitable continuous monitoring strategy beyond ion-selective and enzymatic electrodes or direct oxidation of electroactive molecules[25–27,34-40]. Thus, most clinically relevant nutrients and metabolites in sweat are rarely explored and undetectable by existing wearable sensing technologies. Moreover, current wearable biosensors usually require vigorous exercise to access sweat; although a few recent reports use pilocarpine gel-based iontophoresis for sedentary sweat sampling[22,30,36], this approach suffers from short sweat periods and low sensing accuracy due to the mixing of sweat and gel fluid and the lack of dynamic sweat sampling.

Here we present a universal wearable biosensing strategy based on a judicious combination of the mass-producible laser-engraved graphene (LEG), electrochemically synthesized redox-active nanoreporters (RARs), molecularly imprinted polymer (MIP)-based 'artificial antibodies', as well as unique *in situ* regeneration and calibration technologies (**Fig. 5-1b**). Unlike bioaffinity sensors based on antibodies or classic MIPs which are generally one-time use and require multiple washing steps in order to transduce the bioaffinity interactions in standard ionic solutions[41,42], this approach enables the demonstration of sensitive, selective, and continuous monitoring of a wide range of trace-level biomarkers in biofluids including all nine essential AAs as well as vitamins, metabolites, and lipids commonly found in human sweat (**Appendix B Table 1**). Seamless integration of this unique approach with *in situ* signal processing and wireless communication leads to a powerful wearable sweat sensing technology 'NutriTrek' that is able to perform personalized and non-invasive metabolic and nutritional monitoring toward timely intervention (**Fig. 5-1b**). The incorporation of the carbachol iontophoresis-based sweat induction and efficient microfluidic-based surrounding sweat sampling enables prolonged autonomous and continuous molecular analysis with high temporal resolution and accuracy across activities, during physical exercise and at rest. Using five essential or conditionally essential AAs (i.e., Trp, Try, and three BCAAs (Leu, Ile, Val)) as exemplar nutrients, we corroborated the system in several human trials by enrolling both healthy subjects and patients toward personalized monitoring of central fatigue, standard dietary intakes, nutrition status, metabolic syndrome risks, and COVID-19 severity.

5.2 Design and overview of the autonomous wearable biosensor technology

The flexible and disposable sensor patch consists of two carbachol-loaded iontophoresis electrodes, a multi-inlet microfluidic module, a multiplexed MIP nutrient sensor array, a temperature sensor, and an electrolyte sensor (**Fig. 5-1c–f** and **Fig. B1**). All flexible electrode and sensor designs are based on the LEG which has large surface area, excellent electrochemical properties, and can be produced at a large scale directly on a polyimide substrate *via* CO_2 laser engraving (**Fig. B2**). The sensor patch can be easily attached to skin with conformal contact and interfaces with a miniaturized electronic module for on-demand iontophoresis control, *in situ* signal processing and wireless communication with the user interfaces through Bluetooth (**Fig. 5-1g** and **Figs. B3 and B4**). A custom mobile app 'NutriTrek' was developed to process, display, and store the dynamic metabolic information monitored by the wearable sensors (**Fig. 5-1h**). The wearable system was also integrated into a smartwatch with an electronic paper display (**Fig. 5-1i** and **Fig. B5**).

5.2.1 Biosensor design and evaluation for universal metabolic and nutritional analysis

Universal detection of AAs and other metabolites/nutrients with high sensitivity and selectivity was achieved through careful design of the selective binding MIP layer on the LEG. MIPs are chemically synthesized receptors formed by polymerizing functional monomer(s) with template molecules. Although MIP technology has been proposed for sensing, separation and diagnosis[42,43], it has not yet been demonstrated for continuous wearable sensing as classic MIP sensors require washing steps for sensor regeneration and the detection is generally performed in standard buffer or redox solutions. In our case, the functional monomer (e.g., pyrrole) and crosslinker (e.g., 3-Aminophenylboronic acid) initially form a complex with the target molecule; following polymerization, their functional groups are embedded in the polymeric structure on the LEG; subsequent extraction of the target molecules reveals binding sites on the LEG-MIP electrode that are complementary in size, shape, and charge to the target analyte (**Fig. B6**). Two detection strategies – direct and indirect – are designed based on the electrochemical properties of the target molecules (**Fig. 5-2**). Optimizations and characterizations of the LEG-MIP sensors are detailed in **Appendix B Note 1** and **Figs. B7–13**.

Figure 5-1: **a**, Circulating nutrients such as AAs are associated with various physiological and metabolic conditions. **b**, Schematic of the wearable 'NutriTrek' that enables metabolic monitoring through a synergistic fusion of LEG, RARs and artificial antibodies. **c**,**d**, Schematic (**c**) and layer assembly (**d**) of the microfluidic 'NutriTrek' patch for sweat induction, sampling and biosensing. T, temperature. **e**,**f**, Images of a flexible sensor patch (**e**) and a skin-interfaced wearable system (**f**). Scale bars, 5 mm (**e**) and 2 cm (**f**). **g**, Block diagram of electronic system of 'NutriTrek'. The modules outlined in red dashes are included in the smartwatch version. CPU, central processing unit; POT, potentiometry; In-Amp, instrumentation amplifier; MCU, microcontroller; TIA, trans-impedance amplifier; IP, iontophoresis; CE, counter-electrode; RE, reference electrode; WE, working electrode. **h**, Custom mobile application for real-time metabolic and nutritional tracking. **i**, 'NutriTrek' smartwatch with a disposable sensor patch and an electrophoretic display. Scale bars, 1 cm (top) and 5 cm (bottom).

For electroactive molecules in sweat, the oxidation of bound target molecules in the MIP template can be directly measured by differential pulse voltammetry (DPV) in which the peak current height correlates to analyte concentration (**Fig. 5-2a**). Considering that multiple electroactive molecules can be oxidized at similar potentials, this LEG-MIP approach addresses both sensitivity and selectivity issues. For example, Tyr and Trp, two AAs with close redox potentials (~0.7 V), could be detected selectively with this strategy (**Fig. 5-2b,c** and **Fig. B14**). Linear relationships between peak height current densities and target concentrations with sensitivities of 0.63 μA μM^{-1} cm^{-2} and 0.71 μA μM^{-1} cm^{-2} respectively for the LEG-MIP Tyr and Trp sensors were observed (**Fig. B15**). It is worth noting that choices of monomer/crosslinker/template ratios and incubation periods have substantial influences on sensor response while sample volume does not (**Fig. B10**). The Tyr and Trp sensors can be readily and repeatably regenerated *in situ* without any washing step with a high-voltage amperometry (IT) that oxidizes the bound targets at their redox potentials (**Fig. 5-2d**).

As the majority of metabolites and nutrients (e.g., BCAAs) are non-electroactive and cannot easily be oxidized under operational conditions, we herein utilize an indirect detection approach involving an RAR layer sandwiched between the LEG and MIP layers to enable rapid quantitation (**Fig. 5-2e**). The selective adsorption of the target molecules onto the imprinted polymeric layer decreases the exposure of the RAR to the sample matrix. Controlled-potential voltammetric techniques such as DPV or linear sweeping voltammetry (LSV) can be applied to measure the RAR's oxidization or reduction peak, where the decrease in peak height current density corresponds to an increase in analyte levels. For example, using Prussian Blue nanoparticles (PBNPs) as the RAR (**Fig. B11**), we developed a MIP-LEG Leu sensor with a log-linear relationship between the peak height decrease and Leu concentration and a sensitivity of 702 nA mm^{-2} per decade of concentration (**Fig. 5-2f**). We established this approach to quantify the physiologically relevant range of all nine essential AAs (i.e., Leu, Ile, Val, Trp, Phe, histidine (His), lysine (Lys), methionine (Met), and threonine (Thr)) (**Fig. 5-2g** and **Fig. B16**) as well as a number of vitamins, metabolites, and lipids (vitamins B$_6$, C, D$_3$, and E, glucose, uric acid, creatine, creatinine, and cholesterol) (**Fig. 5-2h** and **Fig. B17**). In addition to these nutrients and metabolites, this approach can be easily reconfigured to enable the monitoring of a broad spectrum of biomarkers ranging from hormones (e.g., cortisol) to drugs (e.g., immunosuppressive drug mycophenolic acid) (**Fig. B18** and **Appendix B Tables 2 and 3**). Most of these targets are undetectable continuously by any existing wearable technology. Considering that a total level of multiple nutrients (e.g., total BCAAs) is often an important health indicator, a multi-template MIP approach can be used to enable accurate and sensitive detection of the total concentration of multiple targets with a single sensor (**Fig. 5-2i,j**). These indirect LEG-RAR-MIP sensors can be regenerated *in situ* upon constant potential applied to the working electrode repels the bound target molecules from the MIP layer with prolonged re-usability (**Fig. 5-2k**). The LEG-MIP sensors show stable responses during repeatable use: The PBNPs-based RAR showed stable redox signals throughout 60 repetitive cyclic voltammetry (CV) scans (**Fig. 5-2l** and **Fig. B11**); minimal output changes were observed throughout a 42-day storage period (**Fig. B19a,b**); the sensors also showed no substantial relative signal shift when used continuously over 5 days (**Fig. B19c**). Compared to traditional MIP preparation processes, the electrodeposited MIP layer on the mass-producible LEG leads to high reproducibility in both selectivity, sensitivity, and device to device consistency (**Figs. B20** and **B21**). The choice of LEG as the MIP deposition substrate also showed advantages in sensor sensitivity as compared to classic electrodes such as glassy carbon electrode, printed carbon electrode, and Au electrode (**Fig. B22**). Other RARs such as the anthraquinone-2-carboxylic acid (AQCA) can also be used for indirect AA sensing with stable performance (negatively scanned DPV was used here to monitor AQCA reduction) (**Fig. 5-2m** and **Fig. B23**). As illustrated in **Fig. 5-2n**, the LEG-AQCA-MIP sensors could be directly regenerated in a raw human sweat sample, resolving a main bottleneck of wearable biosensing. The MIP-LEG AA sensors have excellent selectivity for other analytes in sweat (including AAs with similar structures) at physiologically relevant concentrations (**Fig. 5-2o**, **Fig. B24**, and **Appendix B Table 3**). The LEG-MIP technology showed a comparable sensitivity with the current gold standard laboratory-based GC-MS[44] (**Fig. B25**); the sensor measurements in raw human sweat samples have been validated against GC-MS (**Fig. 5-2p**, **Figs. B26** and B**27**).

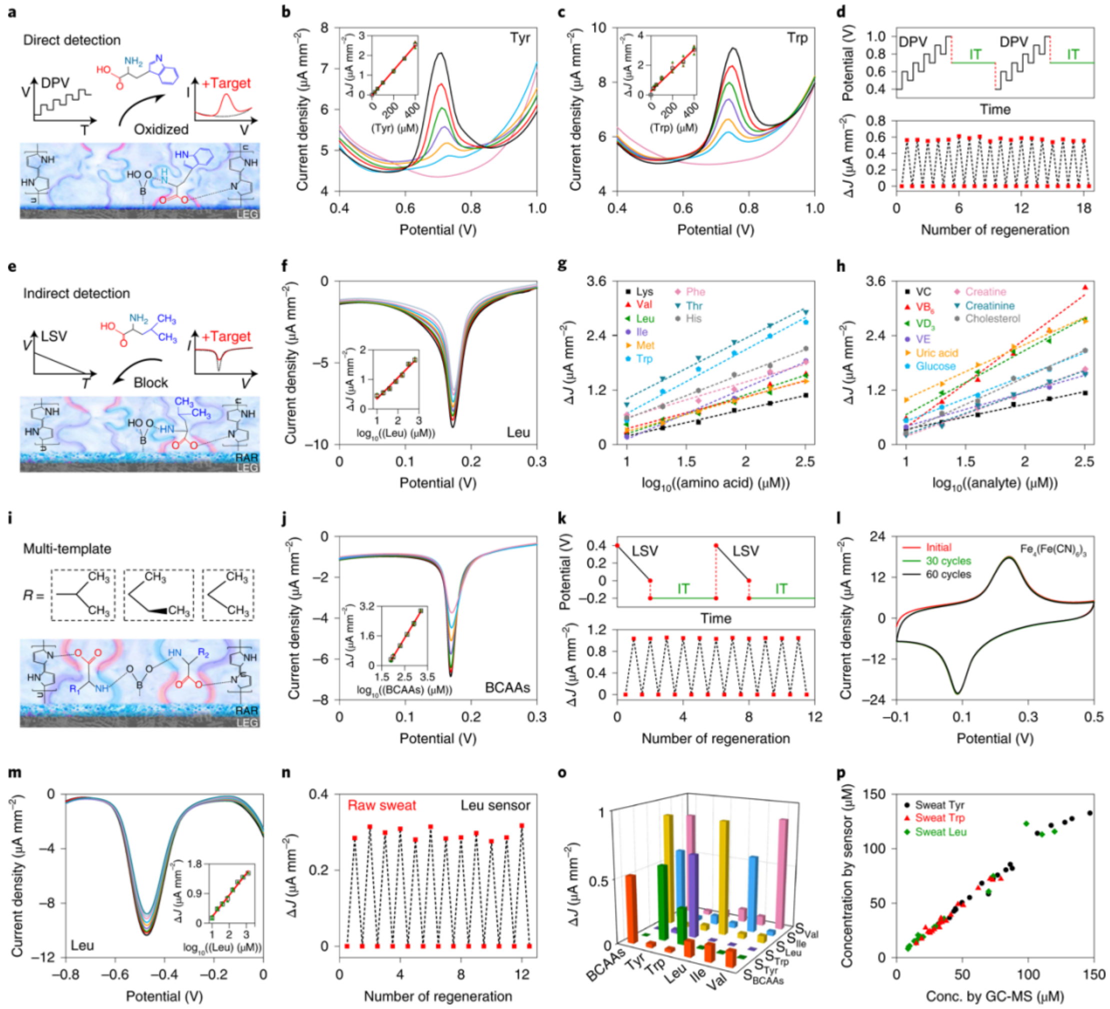

Figure 5-2: **a**, Direct detection of electroactive molecules using LEG–MIP sensors. **b**,**c**, DPV voltammograms of the LEG–MIP sensors for direct Tyr (**b**) and Trp (**c**) detection. Insets, calibration plots with a linear fit. Δ*J*, peak height current density. **d**, In situ continuous sensing and regeneration of an LEG–MIP Trp sensor in 50 µM Trp. **e**, Indirect molecular detection using LEG–RAR–MIP sensors. **f**, LSV voltammograms of indirect Leu detection with LEG–PBNP–MIP sensors. Inset, calibration plot with a linear fit. **g**,**h**, Indirect detection of all essential AAs (**g**) and multiple vitamins, lipids and metabolites (**h**) using LEG–PBNP–MIP sensors. Dashed lines represent linear-fit trendlines. VC, vitamin C; VB6, vitamin B6; VD3, vitamin D3; VE, vitamin E. **i**, Schematic of multi-MIP AA sensors. **j**, LSV voltammograms of an LEG multi-MIP sensor for BCAA quantification. Inset, calibration plot with a linear fit. **k**, In situ continuous sensing and regeneration of an LEG–PBNP–MIP Leu sensor in 50 µM Leu. **l**, Repetitive CV scans of an LEG–PBNP electrode in 0.1 M KCl. **m**, DPV voltammograms of indirect Leu detection with LEG–AQCA–MIP sensors. Inset, the calibration plot. **n**, In situ regeneration of an LEG–AQCA–MIP Leu sensor in a raw sweat sample. **o**, Selectivity of the Trp, Tyr, Leu, Ile, Val and BCAA sensors against other AAs. **p**, Validation of Tyr, Trp and Leu sensors for analysing raw exercise sweat samples (*n* = 20) against GC–MS. All error bars represent the standard deviation (s.d.) from three sensors.

5.2.2 Materials and reagents.

Uric acid, L-tyrosine, silver nitrate, iron chloride (III), dopamine hydrochloride, choline chloride, creatinine, pantothenic acid calcium salt, citrulline, pyridoxine, and lactic acid were purchased from Alfa Aesar. Sodium thiosulfate pentahydrate, sodium bisulfite, tryptophan, leucine, alanine, isoleucine, methionine, valine, lysine, thiamine hydrochloride, serine, sulfuric acid, hydrochloric acid, anthraquinone-2-carboxylic acid (AQCA), 3-Aminophenylboronic acid (APBA), aniline, o-phenylenediamine (o-PD), methylene blue (MB), thionine, 2-(N-morpholino)ethanesulfonic acid hydrate (MES), ethanolamine, N-(3-dimethyl-aminopropyl)-N'-ethylcarbodiimide (EDC), N-hydroxysulfosuccinimide sodium salt (sulfo-NHS), bovine serum albumin (BSA), tris(hydroxymethyl)aminomethane hydrochloride (Tris-HCl), streptavidin-peroxidase conjugate (strep-POD, Roche), and hydroquinone (HQ) were purchased from Sigma Aldrich. Carboxylic acid-modified-magnetic beads (Dynabeads®, M-270) were obtained from Invitrogen. Potassium ferricyanide (III), and potassium ferrocyanide (IV) was purchased from Acros Organics. Acetic acid, methanol, sodium acetate, sodium chloride, sodium dihydrogen phosphate, potassium chloride, potassium hydrogen phosphate, urea, L-ascorbic acid and dextrose (D-glucose) anhydrous, glycine, arginine, inositol, ornithine, aspartic acid, threonine, histidine, riboflavin, creatine, phenylalanine, nicotinic acid, folic acid, glutamic acid, and hydrogen peroxide (30% (w/v)) were purchased from Thermo Fisher Scientific. Insulin capture antibody and biotinylated detector antibody were purchased from R&D systems (Human/Canine/Porcine Insulin DuoSet ELISA). Screen printed carbon electrodes (SPCE) and magnetic holder were purchased from Metrohm DropSens. Medical adhesives were purchased from 3M and Adhesives Research. Polyimide (PI) films (75 μm thick) were purchased from DuPont. PET films (12 μm thick) were purchased from McMaster-Carr.

5.2.3 Fabrication and preparation of the LEG sensors

The LEG electrodes were fabricated on a polyimide film with a thickness of 75 μm (DuPont) with a 50 W CO_2 laser cutter (Universal Laser System). When engraving the PI with a CO_2 laser cutter, the absorbed laser energy is converted to local heat and thus leads to a high localized temperature (>2500 °C), chemical bonds in the PI network are broken and thermal reorganization of the carbon atoms occurs, resulting in sheets of graphene structures. The optimized parameters for the graphene electrodes and electronic connections were power 8%, speed 15%, points per inch (PPI) 1000 in raster mode with 3-time scan. For the active sensing area of the temperature sensor, the optimized parameters were power 3%, speed 18%, PPI 1000 in vector mode with 1-time scan. To prepare the reference electrode, Ag was first modified on the corresponding graphene electrode by multi-current electrodeposition with electrochemical workstation (CHI 832D) at -0.01 mA for 150 s, -0.02 mA for 50 s, -0.05 mA for 50 s, -0.08mA for 50 s, and -0.1 mA for 350 s using a plating solution containing 0.25 M silver nitrate, 0.75 M sodium thiosulfate and 0.5 M sodium bisulfite. 0.1 M $FeCl_3$ solution was further dropped on the Ag surface for 30 s to obtain the Ag/AgCl electrode, and then 3 µL PVB reference cocktail prepared by dissolving 79.1 mg of PVB, 50 mg of NaCl in 1 mL of methanol was dropped on the Ag/AgCl electrode and dried overnight. The Na^+ selective electrode was prepared as follows: 0.6 µL of Na^+ selective membrane cocktail prepared by dissolving 1 mg of Na ionophore X, 0.55 mg Na-TFPB, 33 mg PVC and 65.45 mg DOS into 660 µL of THF was drop-casted onto the graphene electrode and dried overnight. To obtain the desired stable Na^+ sensing performance for long-term continuous measurements, the obtained Na^+ sensor was conditioned overnight in 100 mM NaCl.

The fabrication process of the LEG-MIPs sensor array is illustrated in **Fig. B6**. All the MIP layers are synthesized by electro-polymerization. The polymerization solution was prepared by dissolving 5 mM template (e.g., target amino acid), 12.5 mM aminophenylboronic acid (APBA) and 37.5 mM pyrrole into 0.01 M phosphate buffer saline (PBS) (pH=6.5). For multi-MIP BCAA sensor, 5 mM of each target (i.e., Leu, Ile, and Val) was used. Prior to MIP deposition, the LEG was activated in 0.5 M H_2SO_4 with CV scans for 60 segments (-1.2–1 V with a scan rate of 500 mV s^{-1}). For the direct-detection LEG-MIP sensors, the target imprinted polymer was electrochemically synthesized on the LEG electrode with CV deposition (0–1 V for 10 cycles, 50 mV s^{-1}) using the prepared polymerization solution. The target molecules were extracted by soaking the electrode into an acetic acid/methanol mixture (7:3 v/v) for 1 hour. Subsequently, the resulting electrode was immersed into 0.01 M phosphate buffer saline (pH=6.5) for repetitive CV scans (0.4–1 V with a scan rate of 50 mV s^{-1}) until a stable response was obtained. For LEG-non-imprinted polymer (NIP), the electrode was prepared following the same procedure as LEG-MIP except that there was no template added in the polymerization solution.

For the indirect-detection MIP sensors, electrochemically synthesized redox-active nanoreporters (RARs) (e.g., Prussian Blue nanoparticles (PBNPs) or anthraquinone-2-carboxylic acid (AQCA)) was first modified on the LEG electrode. The PBNPs RAR on the LEG was prepared with cyclic voltammetry (20 cycles) (-0.2 to 0.6 V with a scan rate of 50 mV s^{-1}) in an aqueous solution containing 3 mM $FeCl_3$, 3 mM $K_3Fe(CN)_6$, 0.1 M HCl and 0.1 M KCl. A PBNP layer with appropriate redox signal is necessary to produce a good sensitivity for the final MIP sensors; to achieve this stable and suitable redox signal, the LEG-electrode was rinsed with distilled water after the initial PB deposition and the PB electrodeposition step was repeated for two more times until a stable 70 µA LSV peak in 0.1 M KCl solution was achieved. Subsequently, the LEG-PB was rinsed with distilled water and immersed into a solution containing 0.1 M HCl and 0.1 M KCl for repetitive CV scans (-0.2–0.6 V with a scan rate of 50 mV s^{-1}) until a stable response was obtained. To prepare the AQCA RAR on the LEG, the LEG electrode was first incubated in 50 µL PBS (pH=6.5) with 5 mM AQCA at 4 ºC overnight. Subsequently, the LEG-AQCA was rinsed with distilled water and immersed into a phosphate buffer solution for repetitive CV scans (-0.8–0 V with a scan rate of 50 mV s^{-1}) until a stable response was obtained. For the indirect-detection LEG-PB-MIP sensors, an additional PB activation process was conducted right after the template extraction (IT scan at 1 V in 0.5 M HCl for 600 s), followed by an LEG-PB-MIP sensor stabilization process in 0.1 M KCl (CV scans at -0.2–0.6 V with a scan rate of 50 mV s^{-1}). It should be noted that for the LEG-AQCA-MIP sensor, only 3 CV cycles polymerization was used to prepare the MIP layer, and the sensor was stabilized in 0.01 M phosphate buffer saline (PBS) (pH=6.5) (CV scans at -0.8–0 V with a scan rate of 50 mV s^{-1}).

The morphology of materials was characterized by scanning electron microscopy (SEM, Nova Nano SEM 450) and transmission electron microscope (TEM, Talos S-FEG FEI, USA). The Raman spectrum of the electrodes with different modification were recorded using a 532.8 nm laser with an inVia Reflex (Renishaw). Fourier transform infrared (FT-IR) spectra were measured using IR spectrometer (Nicolet 6700).

5.2.4 Characterization of the LEG sensor performance

A set of electrochemical sensors were characterized in solutions of target analytes. All the *in vitro* sensor characterizations were performed through CHI 832D. The response of the Na^+ sensor was characterized with open circuit potential measurements in the solutions containing varied Na^+ levels. DPV analysis was performed for all the direct-detection LEG-MIP sensor characterizations in 0.01 M PBS (pH 6.5) or in raw sweat. DPV conditions: range, 0.4–1 V; incremental potential, 0.01 V; pulse amplitude, 0.05 V; pulse width, 0.05 s; pulse period, 0.5 s; and sensitivity, 1×10^{-5} A V^{-1}. For *in vitro* indirect-detection of the target molecules based on the LEG-PB-MIP sensors, LSV analysis (0.4–0 V) was performed in 0.1 M KCl. The LSV conditions: range, 0.4–0 V; scan rate, 0.005 V s^{-1}; sample interval, 0.001 V; quiet time, 2 s, and sensitivity, 1×10^{-4} A V^{-1}. For *in vitro* indirect-detection of the target molecules based on the LEG-AQCA-MIP sensors, negative DPV analysis (0–-0.8 V) was performed in 0.01 M PBS. The negative DPV conditions: 0–-0.8 V; incremental potential, 0.01 V; pulse amplitude, 0.05 V; pulse width, 0.05 s; pulse period, 0.5 s; and sensitivity, 1×10^{-5} A V^{-1}. For *in situ* sweat analyte measurement, background and signal curves were recorded before and after incubation; the signal current was obtained as the difference of the peak amplitudes between the post-incubation signal and the background current curves (**Fig. 5-3a–d** and **Fig. B29**). The temperature sensor characterization was carried out on a ceramic hot plate (Thermo Fisher Scientific) (**Fig. B28**). The sensor response was recorded using a parameter analyzer (Keithley 4200A-SCS) and compared with the readings from an infrared thermometer (LASERGRIP 800; Etekcity).

To evaluate the performance of the various electrode substrates for MIP-based AA sensing, LEG, printed carbon electrode (PCE), Au electrode (AuE), and glassy carbon electrode (GCE) were chosen. The GCEs were purchased from CH Instruments. The PCEs were printed on the PI substrate using a Dimatix Materials Printer DMP-2850 (Fujifilm, Minato, Japan) with a commercial carbon ink from NovaCentrix. The AuEs were fabricated via E-beam evaporation: 20 nm of Cr and 100 nm of Au were deposited onto an O_2-plasma pretreated PET substrate. MIP films were prepared with CV deposition (0–1 V for 10 cycles, 50 mV s^{-1}).

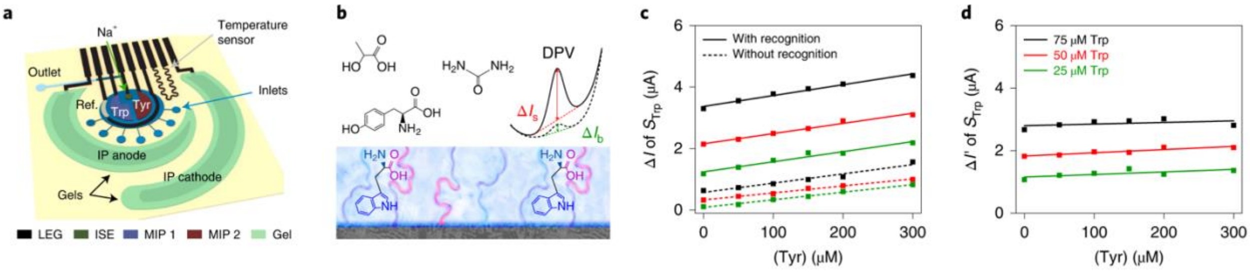

Figure 5-3: **a**, Illustration of a multi-functional wearable sensor patch. ISE, ion-selective electrode. **b**–**d**, The two-scan sensor calibration strategy enabling selective Trp sensing in situ in the presence of Tyr. Δ*I*, peak height current; Δ*I*′, peak height difference caused by target recognition. Solid and dashed curves in **c** and **d** represent linear-fit trendlines.

1.3 Conclusion

Circulating metabolic biomarkers, such as AAs and vitamins, have been associated with various health conditions, including diabetes and CVDs. Metabolic profiling using wearable sensors has become increasingly crucial in precision nutrition and precision medicine, especially in the era of the COVID-19 pandemic, as it provides not only insights into COVID-19 severity but also guidance to stay metabolically healthy to minimize the risk of potential COVID-19 infection. As the pandemic remains rampant throughout the world and regular medical services are at risk of shortage, there is an urgent need to develop and apply wearable sensors that can monitor health conditions via metabolic profiling to achieve at-home diagnosis and timely intervention via telemedicine. However, current wearable electrochemical sensors are limited to a narrow range of detection targets owing to lack of continuous sensing strategies beyond ion-selective and enzymatic electrodes. Though various bio-affinity-based sensors have been developed to detect a broader spectrum of targets using antibodies or MIPs, they generally require multiple washing steps or provide only one-time use; these limitations have hampered their useability in wearable devices. Moreover, the majority of wearable biosensors rely on vigorous exercise to access sweat and are not suitable for daily continuous use.

By integrating mass-producible LEG, electrochemically synthesized RARs and ‘artificial antibodies’, we have demonstrated a powerful universal wearable biosensing strategy that can achieve selective detection of a broad range of biomarkers (including all essential AAs, vitamins, metabolites, lipids, hormones and drugs) and reliable in situ regeneration. Furthermore, to enable continuous and on-demand metabolic and nutritional monitoring across the activities, we have integrated the LEG–MIP sensor array and iontophoresis-based sweat induction into a wireless wearable technology, with optimized multi-inlet microfluidic sudomotor axon reflex sweat sampling, in situ signal processing, calibration and wireless communication. Using this telemedicine technology, we have demonstrated the wearable and continuous monitoring of post-prandial AA responses to identify risks for metabolic syndrome. The high correlation between sweat and serum BCAAs suggests that this technology holds great promise for use in metabolic syndrome risk monitoring. The substantial difference in Leu between COVID-19-positive and COVID-19-negative blood samples indicates the potential of using this technology for at-home COVID-19 management. We envision that this wearable technology could play a crucial role in the realization of precision nutrition through continuous monitoring of circulating biomarkers and enabling personalized nutritional intervention. This technology could also be reconfigured to continuously monitor a variety of other biomarkers towards a wide range of personalized preventive, diagnostic and therapeutic applications.

BIBLIOGRAPHY

1. Trumbo, P., Schlicker, S., Yates, A. A. & Poos, M. Dietary reference intakes for energy, carbohydrate, fiber, fat, fatty acids, cholesterol, protein and amino acids. *J. Am. Diet. Assoc.* **102**, 1621–1630 (2002).

2. Wu, G. Amino acids: metabolism, functions, and nutrition. *Amino Acids* **37**, 1–17 (2009).

3. Lynch, C. J. & Adams, S. H. Branched-chain amino acids in metabolic signalling and insulin resistance. *Nat. Rev. Endocrinol.* **10**, 723–736 (2014).

4. Wang, T. J. et al. Metabolite profiles and the risk of developing diabetes. *Nat. Med.* **17**, 448–453 (2011).

5. Mayers, J. R. et al. Elevation of circulating branched-chain amino acids is an early event in human pancreatic adenocarcinoma development. *Nat. Med.* **20**, 1193–1198 (2014).

6. Kau, A. L., Ahern, P. P., Griffin, N. W., Goodman, A. L. & Gordon, J. I. Human nutrition, the gut microbiome and the immune system. *Nature* **474**, 327–336 (2011).

7. Fernstrom, J. D. & Wurtman, R. J. Brain serotonin content: physiological dependence on plasma tryptophan levels. *Science* **173**, 149–152 (1971).

8. Fernstrom, J. D. & Fernstrom, M. H. Tyrosine, phenylalanine, and catecholamine synthesis and function in the brain. *J. Nutr.* **137**, 1539S–1547S (2007).

9. Dierckx, T. *et al*. The metabolic fingerprint of COVID-19 severity. Preprint at *medRxiv* (2020) https://doi.org/10.1101/2020.11.09.20228221

10. Grant, W. B. et al. Evidence that vitamin D supplementation could reduce risk of influenza and COVID-19 infections and deaths. *Nutrients* **12**, 988–1006 (2020).

11. Belanger, M. J. et al. COVID-19 and disparities in nutrition and obesity. *N. Engl. J. Med.* **383**, e69 (2020).

12. Stefan, N., Birkenfeld, A. L. & Schulze, M. B. Global pandemics interconnected—obesity, impaired metabolic health and COVID-19. *Nat. Rev. Endocrinol.* **17**, 135–149 (2021).

13. Wishart, D. S. Emerging applications of metabolomics in drug discovery and precision medicine. *Nat. Rev. Drug Discov.* **15**, 473–484 (2016).

14. Dettmer, K., Aronov, P. A. & Hammock, B. D. Mass spectrometry-based metabolomics. *Mass Spectrom. Rev.* **26**, 51–78 (2007).

15. Ray, T. R. et al. Bio-integrated wearable systems: A comprehensive review. *Chem. Rev.* **119**, 5461–5533 (2019).

16. Hollander, J. E. & Carr, B. G. Virtually perfect? Telemedicine for COVID-19. *N. Engl. J. Med.* **382**, 1679–1681 (2020).

17. Niu, S. et al. A wireless body area sensor network based on stretchable passive tags. *Nat. Electron.* **2**, 361–368 (2019).

18. Meng, K. et al. A wireless textile-based sensor system for self-powered personalized health care. *Matter* **2**, 896–907 (2020).

19. Wang, C. et al. Monitoring of the central blood pressure waveform via a conformal ultrasonic device. *Nat. Biomed. Eng.* **2**, 687–695 (2018).

20. Ni, X. et al. Automated, multiparametric monitoring of respiratory biomarkers and vital signs in clinical and home settings for COVID-19 patients. *Proc. Natl Acad. Sci. USA* **118**, e2026610118 (2021).

21. Jeong, H. et al. Differential cardiopulmonary monitoring system for artifact-canceled physiological tracking of athletes, workers, and COVID-19 patients. *Sci. Adv.* **7**, eabg3092 (2021).

22. Sempionatto, J. R. et al. An epidermal patch for the simultaneous monitoring of haemodynamic and metabolic biomarkers. *Nat. Biomed. Eng.* **5**, 737–748 (2021).

23. Xu, C., Yang, Y. & Gao, W. Skin-interfaced sensors in digital medicine: from materials to applications. *Matter* **2**, 1414–1445 (2020).

24. Heikenfeld, J. et al. Accessing analytes in biofluids for peripheral biochemical monitoring. *Nat. Biotechnol.* **37**, 407–419 (2019).

25. Bariya, M., Nyein, H. Y. Y. & Javey, A. Wearable sweat sensors. *Nat. Electron.* **1**, 160–171 (2018).

26. Yang, Y. & Gao, W. Wearable and flexible electronics for continuous molecular monitoring. *Chem. Soc. Rev.* **48**, 1465–1491 (2019).

27. Kim, J., Campbell, A. S., de Ávila, B. E.-F. & Wang, J. Wearable biosensors for healthcare monitoring. *Nat. Biotechnol.* **37**, 389–406 (2019).

28. Gao, W. et al. Fully integrated wearable sensor arrays for multiplexed in situ perspiration analysis. *Nature* **529**, 509–514 (2016).

29. Bandodkar, A. J. et al. Battery-free, skin-interfaced microfluidic/electronic systems for simultaneous electrochemical, colorimetric, and volumetric analysis of sweat. *Sci. Adv.* **5**, eaav3294 (2019).

30. Emaminejad, S. et al. Autonomous sweat extraction and analysis applied to cystic fibrosis and glucose monitoring using a fully integrated wearable platform. *Proc. Natl Acad. Sci. USA* **114**, 4625–4630 (2017).

31. Torrente-Rodríguez, R. M. et al. Investigation of cortisol dynamics in human sweat using a graphene-based wireless mHealth System. *Matter* **2**, 921–937 (2020).

32. Koh, A. et al. A soft, wearable microfluidic device for the capture, storage, and colorimetric sensing of sweat. *Sci. Transl. Med.* **8**, 366ra165 (2016).

33. Ray, T. R. et al. Soft, skin-interfaced sweat stickers for cystic fibrosis diagnosis and management. *Sci. Transl. Med.* **13**, eabd8109 (2021).

34. Lee, H. et al. A graphene-based electrochemical device with thermoresponsive microneedles for diabetes monitoring and therapy. *Nat. Nanotech.* **11**, 566–572 (2016).

35. Lee, H. et al. Wearable/disposable sweat-based glucose monitoring device with multistage transdermal drug delivery module. *Sci. Adv.* **3**, e1601314 (2017).

36. Kim, J. et al. Noninvasive alcohol monitoring using a wearable tattoo-based iontophoretic-biosensing system. *ACS Sens.* **1**, 1011–1019 (2016).

37. Kim, J. et al. A skin-interfaced, miniaturized microfluidic analysis and delivery system for colorimetric measurements of nutrients in sweat and supply of vitamins through the skin. *Adv. Sci.* **9**, 2103331 (2022).

38. Sempionatto, J. R. et al. Wearable and mobile sensors for personalized nutrition. *ACS Sens.* **6**, 1745–1760 (2021).

39. Yang, Y. et al. A laser-engraved wearable sensor for sensitive detection of uric acid and tyrosine in sweat. *Nat. Biotechnol.* **38**, 217–224 (2020).

40. Yu, Y. et al. Biofuel-powered soft electronic skin with multiplexed and wireless sensing for human-machine interfaces. *Sci. Robot.* **5**, eaaz7946 (2020).

41. Wang, J. Electrochemical biosensors: towards point-of-care cancer diagnostics. *Biosens. Bioelectron.* **21**, 1887–1892 (2006).

42. Uzun, L. & Turner, A. P. Molecularly-imprinted polymer sensors: realising their potential. *Biosens. Bioelectron.* **76**, 131–144 (2016).

43. Parlak, O., Keene, S. T., Marais, A., Curto, V. F. & Salleo, A. Molecularly selective nanoporous membrane-based wearable organic electrochemical device for noninvasive cortisol sensing. *Sci. Adv.* **4**, eaar2904 (2018).

44. Kaspar, H., Dettmer, K., Gronwald, W. & Oefner, P. J. Automated GC–MS analysis of free amino acids in biological fluids. *J. Chromatogr. B* **870**, 222–232 (2008).

Appendix B

Supplementary Note 1 | Optimization and characterization of the LEG-MIP biosensors

Characterization of the MIP sensor preparation.

The preparation of the LEG-MIP sensors was characterized electrochemically with differential pulse voltammetry (DPV) in 0.1 M KCl solution containing 2.0 mM $K_4Fe(CN)_6/K_3Fe(CN)_6$ (1:1) (**Fig. B7a**). The LEG displayed a high oxidation peak owing to its large electrochemically active surface area. The redox peak substantially decreased after the MIP film deposition (co-polymerization of APBA and pyrrole in the presence of Trp here) due to the fact that the less conducting polymer layer blocked the LEG from the redox reporter solution. The template molecules were removed during template extraction step, leaving behind imprinted cavities that are complementary, both chemically and sterically to the template molecules. These cavities allow reporter ions to reach the electrolyte/electrode interface, resulting in a rise of the redox peak current.

Raman spectrum was also used to study the surface roughness of the LEG-MIP sensor during preparation process. Raman intensity is influenced by the scattering of the exciting light from the sample surface, and thus decreases with the increase of surface roughness. As shown in **Fig. B7b**, Raman intensity of C=C backbone stretching increased after polymerization (smooth surface), and then decreased after template extraction (rough surface), indicating the residual cavities on the surface resulted from the template extraction[1]. To further validate the successful preparation of the MIP layer, a non-imprinted polymer (NIP) film was prepared on the LEG as the control. The standard MIP template extraction procedure and further incubation in 50 µM Trp did not lead to substantial signal change of the LEG-NIP in the standard redox solution (**Fig. B7c**).

For the preparation of the LEG-RAR-MIP sensors, redox reporters such as Prussian blue (PB) and anthraquinone-2-carboxylic acid (AQCA) were deposited between the MIP and graphene layers. For the PB RAR, the preparation process was characterized electrochemically with linear sweep voltammetry (LSV) in 0.1 M KCl as illustrated in **Fig. B7d**. The LEG-PB displayed a high reduction peak of PB which decreased after deposition of the polymer film (co-polymerization of APBA and pyrrole in the presence of Leu here) due to the PB blockage by the polymer. The extraction of the template molecules (with CV sweeping in 0.1 M HCl and 0.1 M KCl) leads to the target selective cavities and increases the exposure of the PB film to the electrolyte solution, resulting an increased redox signal.

The Raman spectra of the LEG-PB-MIP Leu showed similar behavior as the LEG-MIP Trp sensor: Raman intensity of C=C backbone stretching increased after polymerization on LEG-PB, and then decreased after template extraction, the residual cavities were left on the surface resulted from the template extraction (**Fig. B7e**). To further validate the successful preparation of the MIP layer on the LEG-PB, a NIP film was prepared on the LEG-PB as the control. The standard MIP template extraction procedure and further incubation in 50 μM Leu did not lead to substantial signal change of the LEG-PB-NIP (**Fig. B7f**).

Electrochemical kinetics of the LEG-MIP electrodes.

The electrochemical kinetic process on the modified electrode plays an important role in understanding whether the reaction process at the modified electrode is controlled by adsorption and/or diffusion. Cyclic voltammetry (CV) was used to study the effect of scan rate on the peak current for both the direct and indirect detection LEG-MIP sensors (**Fig. B8**).

Since the electroactive target (e.g., Trp) can be directly oxidized at a given voltage, the LEG-MIP Trp sensor was evaluated in 0.01 M PBS containing 50 μM Trp (**Fig. B8a,b**). A linear dependence was obtained between the anodic peak current and scan rate, indicating that the oxidation of Trp on the direct detection MIP sensor is controlled by adsorption processes. On the other side, the redox peak of the RAR (e.g., PB) can be directly used to study the electrode kinetics in 0.1 M KCl (**Fig. B8c,d**). In this case, both anodic and cathodic peak currents showed proportional relationships to square root of the scan rate, suggesting that electrochemical redox reactions at LEG-PB-MIP Leu sensor were a diffusion- controlled process[2]. The relation between measured peak height current density J_{pa} (μA mm^{-2}) and scan rate v (mV s^{-1}) for direct and indirect detection MIP sensors are as follows:

LEG-MIP Trp sensors: $Jpa = 0.1718 + 0.006v$

LEG-PB MIP Leu sensors: $Jpa, anodic = -8.338 + 3.5031\sqrt{v}$

$Jpa, cathodic = 5.007 - 3.458\sqrt{v}$

The above results explain the reasons why the current signal has a linear relationship with the concentration of the target in direct detection, while it is log-linear with the target levels in indirect detection. To minimize the influence of oxidation reactions of common sweat interferants, the reduction peak of PB is chosen for further analyzing of in direct detection.

Theoretical and experimental optimization of MIP composition.

MIPs can either rely on covalent or non- covalent interactions. In the case of a wearable sensor which should be capable of regeneration for continuous monitoring, weak reversible non-covalent interactions are ideal. There are multiple of monomers which are capable of forming non-covalent bonds with amino acids (e.g., Trp and Leu), however we narrowed our search to electroactive monomers since sensor fabrication with such monomers requires only electropolymerization on the working electrode in the presence of the desired template molecules. In addition, electroactive monomers efficiently transduce binding events, thus improving detectability[3]. Thus, the formulations such as choices of monomers and monomer/template ratios have substantial influence on the sensitivity and the selectivity of the MIP sensor.

Taking the Trp sensor design as an example, we utilized density functional theory (DFT) calculations to quantify the binding energy between Trp and six commonly used electroactive monomers: aminophenylboronic acid (APBA), aniline, ethylenedioxythiophene (EDOT), phenylene, pyrrole, and thiophene (**Fig. B9a,b**). The calculations were carried out using the ORCA software[4]. The semiempirical Austin Model 1 (AM1) was used first to achieve a rough estimate of geometric optimal configurations. The higher level B3LPY functional with a 5-31(d,p) basis set was then used to calculate final geometric configurations and binding energies. Binding energies were calculated with the typical formula:

$$\Delta E = E_{Monomer}-E_{Template} - (E_{Template}+E_{Monomer})$$

The DFT simulated bonding energies of the monomer-target complexes were demonstrated in **Fig. B9b**. To maximize sensitivity of the MIP it is common to select the monomer which has the highest binding affinity to Trp. Further, it has been previously demonstrated that the co-polymerization of a monomer with high affinity and a monomer with low affinity (crosslinker) to the template can produce highly selective MIPs by mitigating non-selective binding[5]. APBA exhibits the highest interaction energy with the Trp, indicating that APBA is an ideal crosslinker or co-monomer for Trp MIP. The choice of pyrrole (which has lowest interaction energy) and APBA as the monomer and crosslinker could leads to MIPs with both high selectivity and high regeneration capability.

Our experimental data demonstrates that the choice of APBA/aniline also leads to high sensitivity (reflected by the current peak height of the LEG-MIP sensor in 50 μM Trp) compared to other individual monomers and other monomer/crosslinker combinations (**Fig. B9c**). The ratio of template, crosslinker, and monomer is another key parameter MIP quality. Based on the experimental data illustrated in **Fig. B9d**, the ratio of 1:2.5:7.5 (template/crosslinker/monomer) led to the optimal sensitivity for Trp detection.

Optimization of the LEG-MIP recognition *in vitro.*

To obtain the optimal sensor performance for rapid sample analysis, the influences of sample incubation time and volume were evaluated experimentally. As demonstrated in **Fig. B10a,b**, the current density of the peak height of the LEG-MIP Trp sensors increases rapidly with the increase of incubation time initially, and then gradually stabilizes after 5 min (with an optimal incubation time of 7 min), indicating the saturated adsorption for Trp. Unlike the incubation time, sample volumes (between 0.028–1.1 μL mm^{-2}) didn't show substantial influence on the sensor response as illustrated in **Fig. B10c,d**.

Characterization of the RARs for indirect MIP detection.

The microstructure and element composition of the LEG-RARs were characterized in **Fig. B11**. The LEG displayed an ultra-thin 3D flakes with few-layer features while the C and N elements obtained by laser pyrolysis of PI were evenly distributed in the flakes (**Fig. B11a**). PB RAR nanoparticles with a diameter of about 100 nm were successfully immobilized on the graphene surface as illustrated in **Fig. B11b,e**. The PB RAR maintained its microstructure after 60 cycles of electrochemical cycling (**Fig. B11c**). The successful modification and electrochemical stability of AQCA were also confirmed by FTIR and element mapping (**Fig. B11d,f**).

The high demand for electrochemical stability of wearable sensors in practical applications poses high requirements for RARs. Therefore, the performance of four RARs including PB, AQCA, MB, and thionine before and after repetitive LSV or DPV scans was investigated (**Fig. B12**). As summarized in **Fig. B12e**, PB and AQCA displayed best stability among these four.

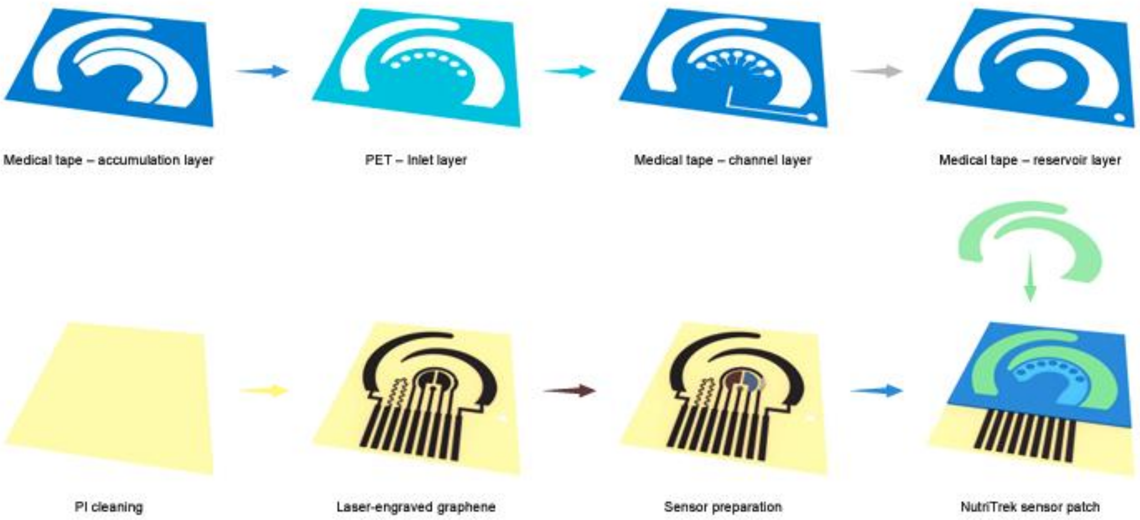

Figure B1: Fabrication process of the multifunctional flexible wearable sensor patch.

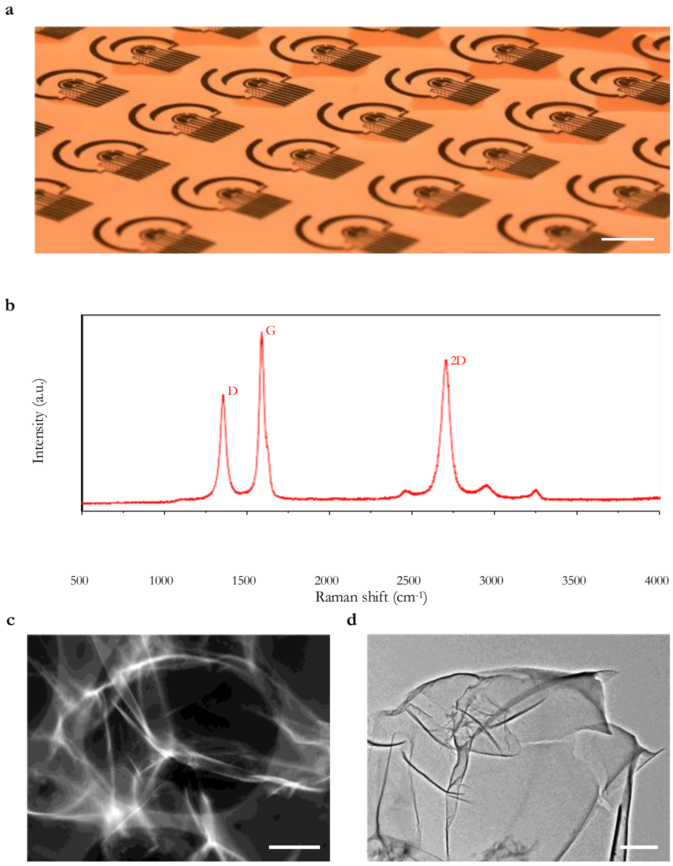

Figure B2: Characterization of the LEG. a, Optical image of a flexible LEG sensor patch array fabricated *via* low-cost and mass-producible CO2 laser engraving. Scale bar, 1 cm. **b,** Raman spectra of the LEG. **c,d,** High-angle annular dark-field scanning transmission electron microscopy (HAADF-STEM) (**c**) and bright-field transmission electron microscopy (TEM) image (**d**) of the LEG. Scale bars, 1 µm and 500 nm, respectively.

Figure B3: Integrated flexible NutriTrek prototype for personalized nutritional monitoring. **a**,**b**, Optical photos of a wearable NutriTrek prototype consisting of a flexible, disposable microfluidic sensor patch (**a**) for autonomous sweat stimulation and sweat analysis and a flexible printed circuit board (FPCB) (**b**) for *in situ* electrochemical control, signal processing, and wireless communication. Scale bars, 5 mm (**a**) and 1 cm (**b**). **c**,**d**, Optical photos of the integrated system on the body. Scale bars, 5 cm (**c**) and 1 cm (**d**). **e**, Optical photo of a flexible NutriTrek patch interfacing with the custom cell phone app for real-time data collection. Scale bar, 3 cm.

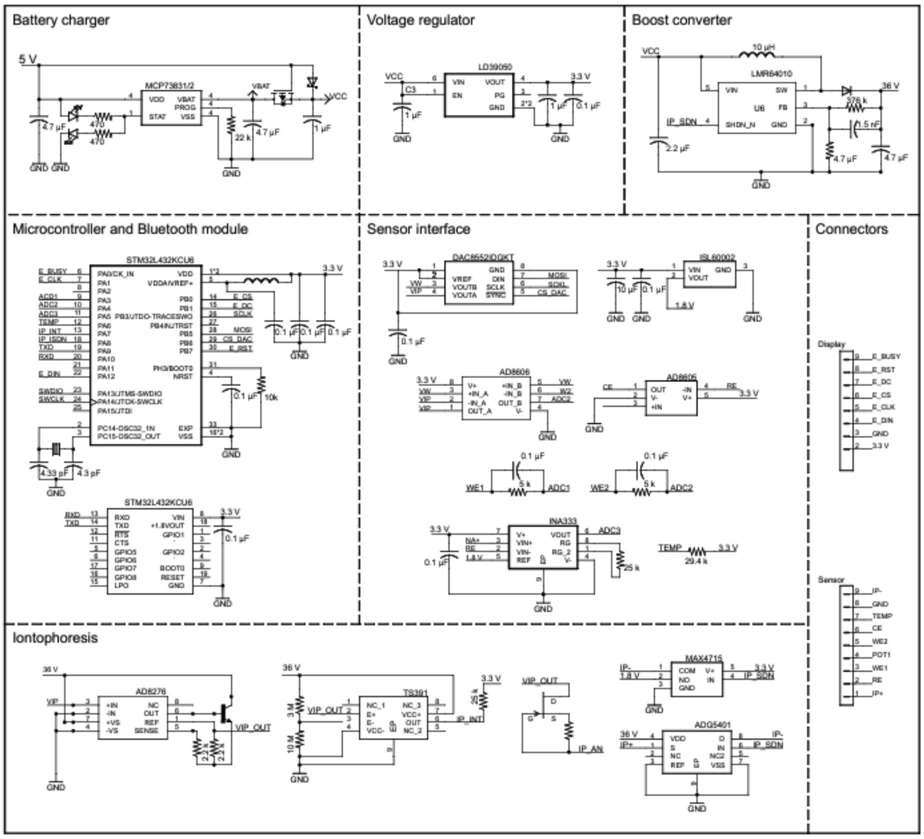

Figure B4: The detailed circuit diagram of the NutriTrek.

Figure B5: Fully integrated NutriTrek smartwatch for personalized nutritional monitoring. a,**b**, Top view (**a**) and bottom (**b**) view photos of a smartwatch PCB connected to the MIP sensor. Scale bars, 1 cm. **c**, Photo of an electrophoretic display-mounted smartwatch without a 3D printed case that displays the sensor reading in real-time. Scale bar, 5 mm. **d**,**e**, Photos of a fully assembled NutriTrek smartwatch. Scale bars, 1 cm (**d**) and 2 cm (**e**).

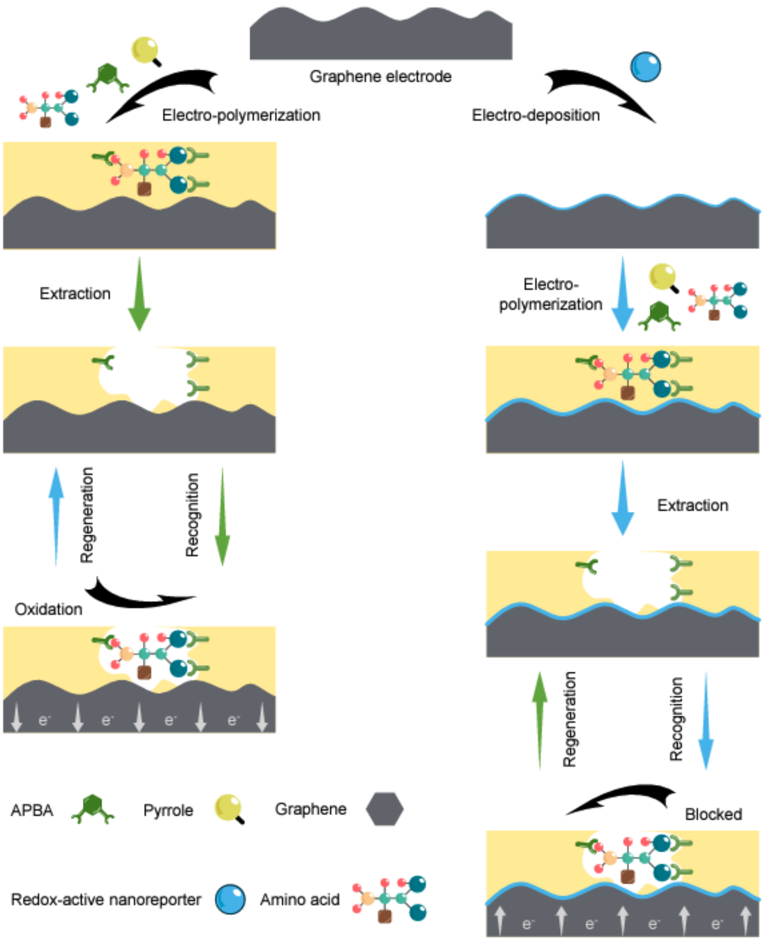

Figure B6: **Schematic of the preparation procedure and detection mechanism of the LEG- MIP AA sensors**. Left panel, electroactive AA sensor with direct detection mechanism; Right panel, AA sensor with indirect detection mechanism.

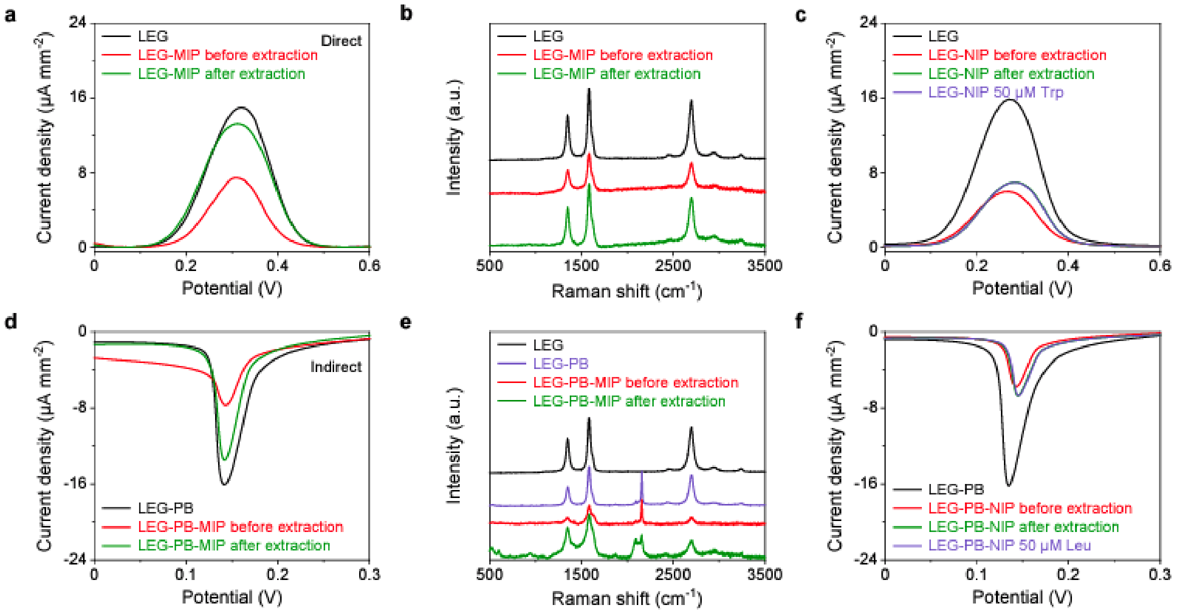

Figure B7: Characterization and validation of the MIP sensor preparation. a, DPV voltammograms of the LEG, the LEG-MIP before template (Trp) extraction, and the LEG-MIP after template (Trp) extraction in 0.1 M KCl solution containing 2.0 mM K4Fe(CN)6/K3Fe(CN)6 (1:1). **b**, Raman spectra of the LEG, the LEG-MIP before template (Trp) extraction, and the LEG-MIP after template (Trp) extraction. **c**, DPV voltammograms of the LEG, the LEG-non-imprinted polymer (NIP), the LEG-NIP after template extraction procedure, and the LEG-NIP after extraction procedure (followed by a 7-min incubation in 50 µM Trp) in 0.1 M KCl solution containing 2.0 mM K4Fe(CN)6/K3Fe(CN)6 (1:1). **d**, LSV voltammograms of the LEG, the LEG-PB-MIP before template (Leu) extraction, and the LEG-PB-MIP after template (Leu) extraction in 0.1 M KCl. **e**, Raman spectra of the LEG, the LEG-PB, the LEG-PB-MIP before template (Leu) extraction, and the LEG-PB-MIP after template (Leu) extraction. **f**, LSV voltammograms of the LEG, the LEG-PB-NIP, the LEG-PB-NIP after template extraction procedure, and the LEG-PB-NIP after template extraction procedure (followed by a 7-min incubation in 50 µM Leu) in 0.1 M KCl.

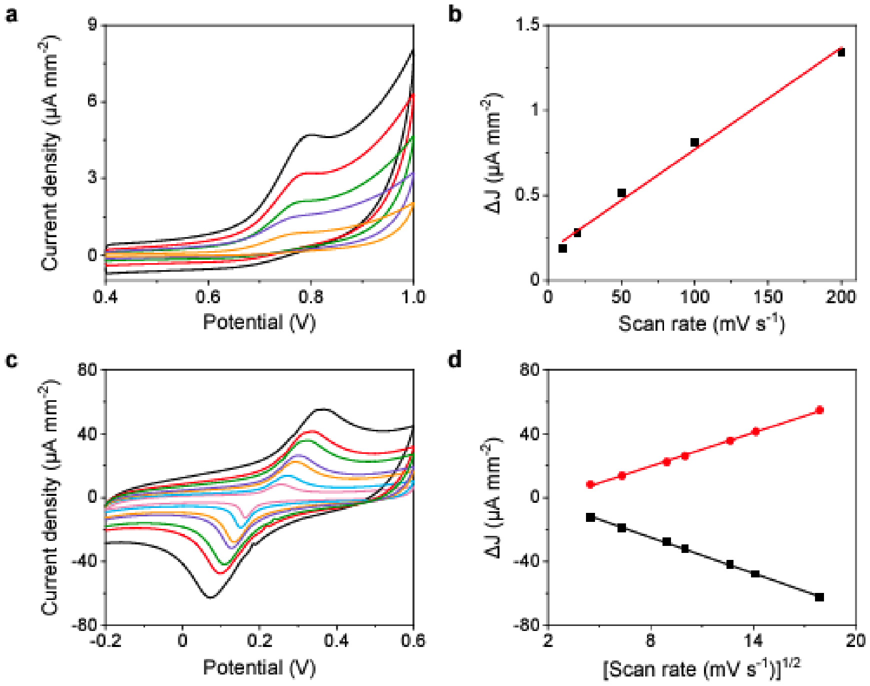

Figure B8: Characterization of the electrochemical kinetics of the LEG-MIP electrodes. **a**,**b**, Cyclic voltammograms (**a**) of an LEG-MIP Trp sensor at the scan rates from 10 to 200 mV s^{-1} in 50 µM Trp, and the corresponding plot (**b**) of anodic peak current densities versus scan rate. **c**,**d**, Cyclic voltammograms (**c**) of an LEG-PB-MIP Leu sensor in 0.1 M KCl at the scan rates from 10 to 300 mV s^{-1} and the corresponding plot (**d**) of anodic and cathodic peak current densities versus square-root of scan rate. Solid lines in **b**,**d** represent linear fit trendlines.

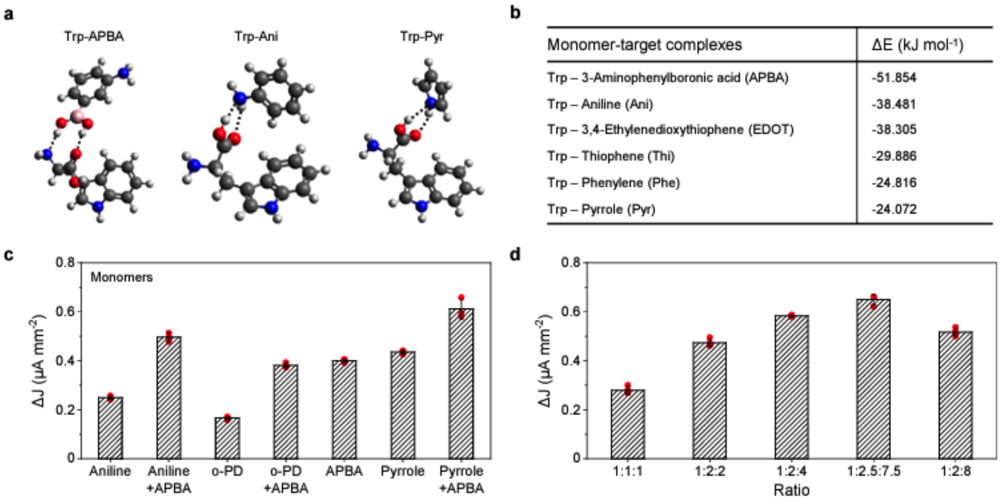

Monomer-target complexes	ΔE (kJ mol^{-1})
Trp – 3-Aminophenylboronic acid (APBA)	-51.854
Trp – Aniline (Ani)	-38.481
Trp – 3,4-Ethylenedioxythiophene (EDOT)	-38.305
Trp – Thiophene (Thi)	-29.886
Trp – Phenylene (Phe)	-24.816
Trp – Pyrrole (Pyr)	-24.072

Figure B9: Theoretical and experimental optimization of the MIP composition. a, Density functional theory (DFT)-optimized geometries of the monomer (Pyr)/target (Trp) bonding. **b**, DFT simulated bonding energies of the monomer-target complexes. **c**,**d**, Current density of the peak height (ΔJ) of the Trp MIP sensors based on different monomer/target combinations (**c**) and different target/crosslinker/monomer ratios (**d**) in 50 µM Trp. Ratios of target/(crosslinker)/monomer in **c**, 1:(2.5):7.5; APBA was used as the crosslinker for **c** and **d**. Error bars represent the s.d. from 3 sensors.

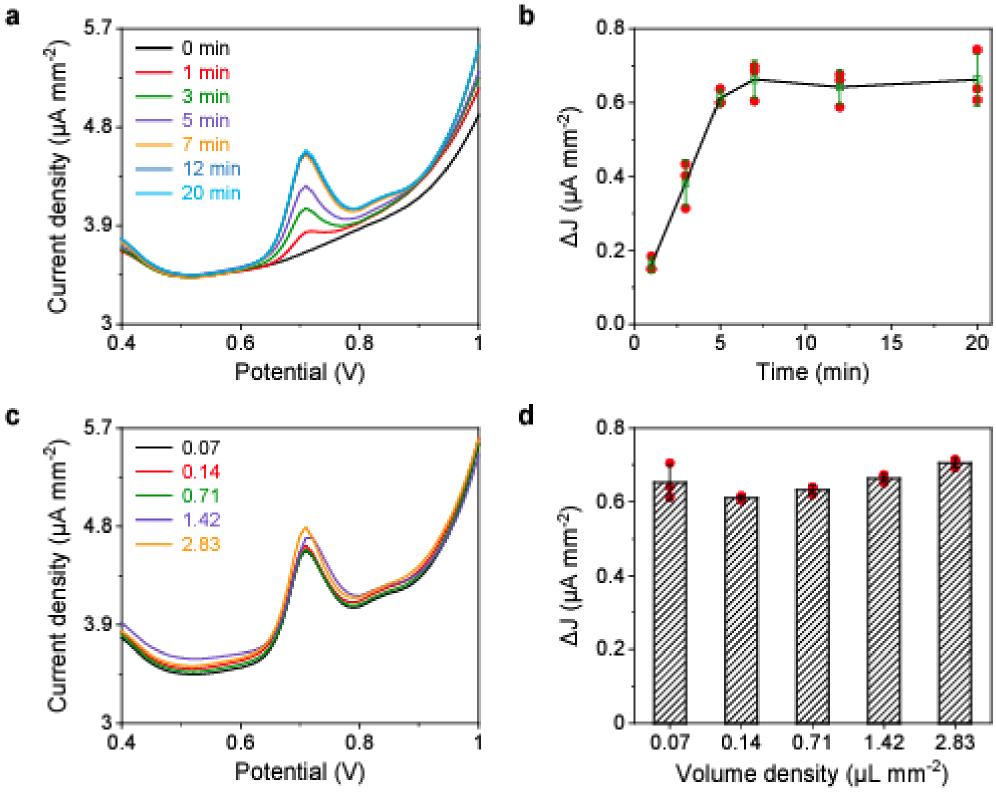

Figure B10: Evaluation of the effect of incubation time and sample volume on the LEG-MIP sensor performance. a,**b**, DPV voltammograms (**a**) and current density of the peak height (ΔJ) (**b**) of the Trp sensors in 50 µM Trp with varied 1–20 min incubation time. **c**,**d**, DPV voltammograms (**c**) and current density of the peak height (ΔJ) (**d**) of the Trp sensors in 50 µM Trp with varied sample volumes. Error bars in **b** and **d** represent the s.d. from 3 sensors.

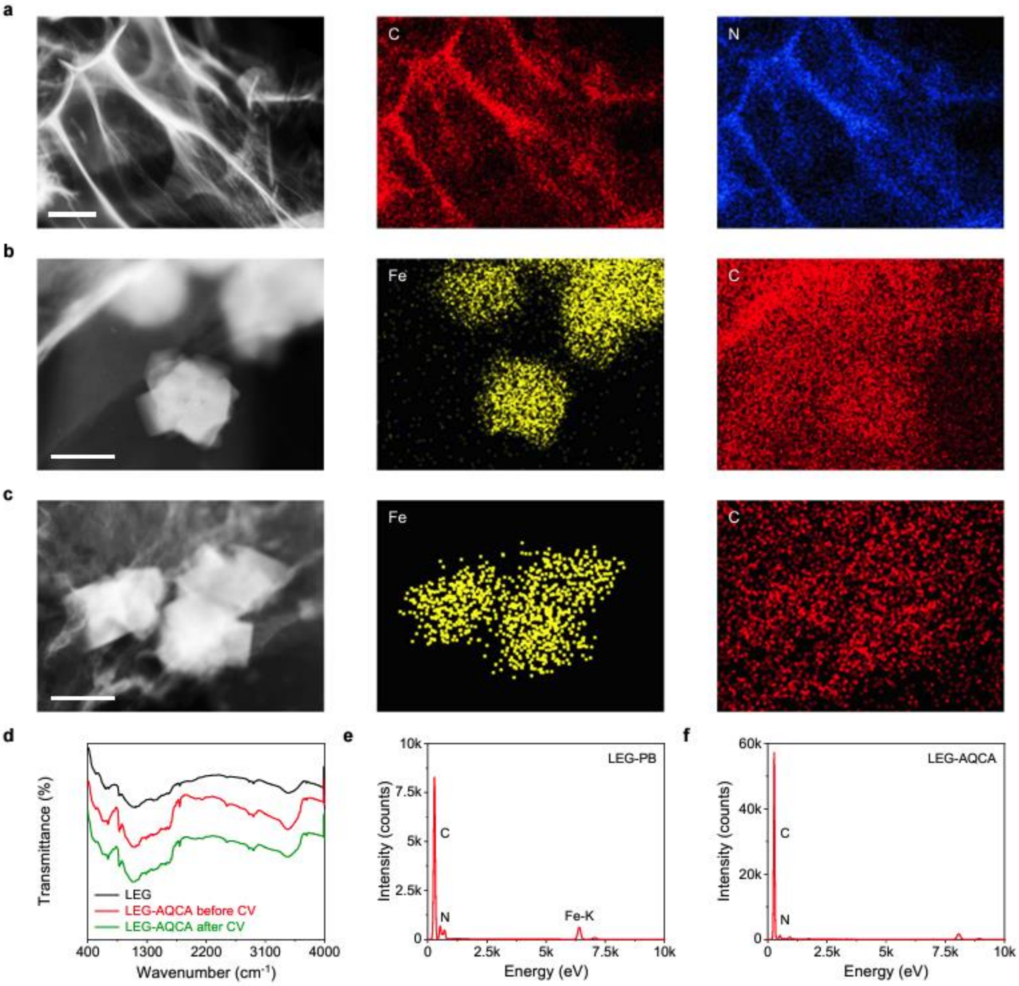

Figure B11: Microscopic characterization of the RARs on the LEG. a, HAADF-STEM and element mapping images of the LEG. Scale bar, 2 µm. **b**,**c**, HAADF-STEM element mapping images of the PB nanoparticles (as an RAR) on the LEG before (**b**) and after (**c**) 60 cyclic voltammetry (CV) cycles. Scale bars, 100 nm. **d**, Fourier-transform infrared spectroscopy (FTIR) of the LEG, the LEG-AQCA before and after 60 cycles of cyclic voltammetry (CV) scan. **e**,**f**, Energy dispersive X-ray (EDX) spectroscopy of the LEG-PB

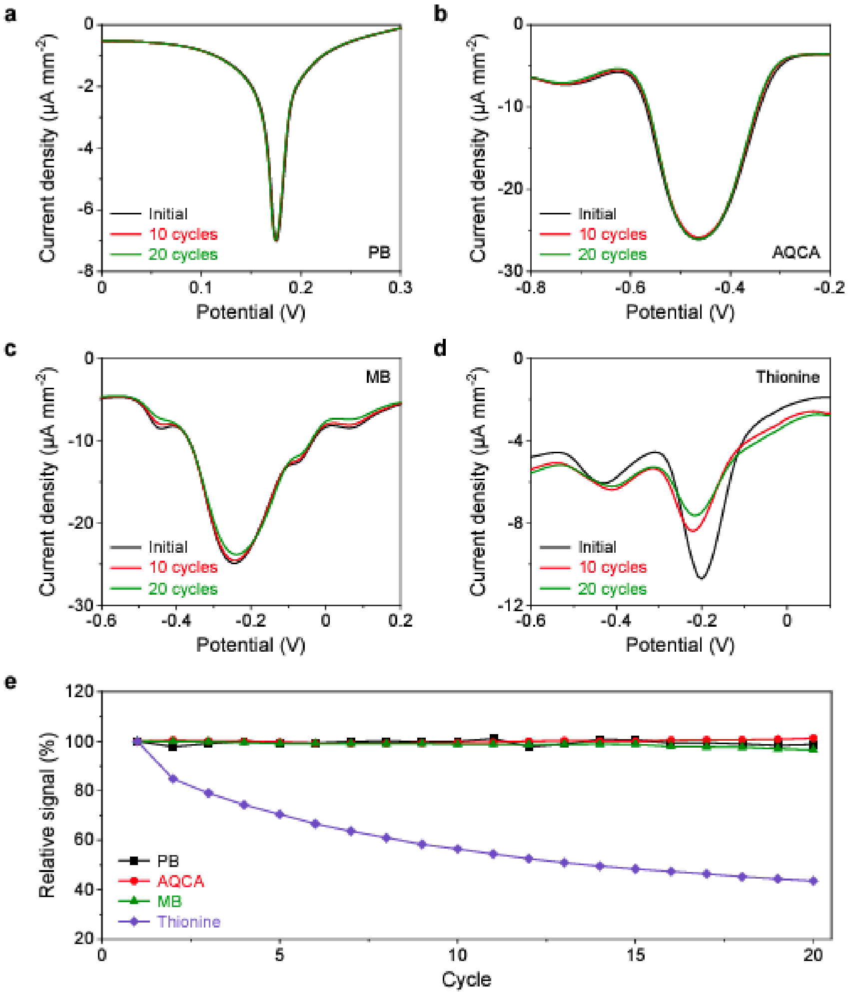

Figure B12: Electrochemical characterization of the RARs on the LEG. a, Repetitive LSVs of the PB modified LEG electrodes. **b**–**d**, Repetitive negative DPVs of the AQCA (**b**), MB (**c**), and thionine (**d**) modified LEG electrodes. **e**, Relative peak signal changes of PB, AQCA, MB, and thionine RAR-modified LEG electrode under repeating voltammetric scans. DPV conditions for **b**–**e**: scan range, -0.2—0.8 V, 0.2—0.6 V and 0.1—0.6 V, respectively, for AQCA, MB, and Thionine; scan rate, 5 mV s^{-1}; sample interval, 1 mV; quiet time, 2 s; sensitivity, 1×10^{-4} A V^{-1}.

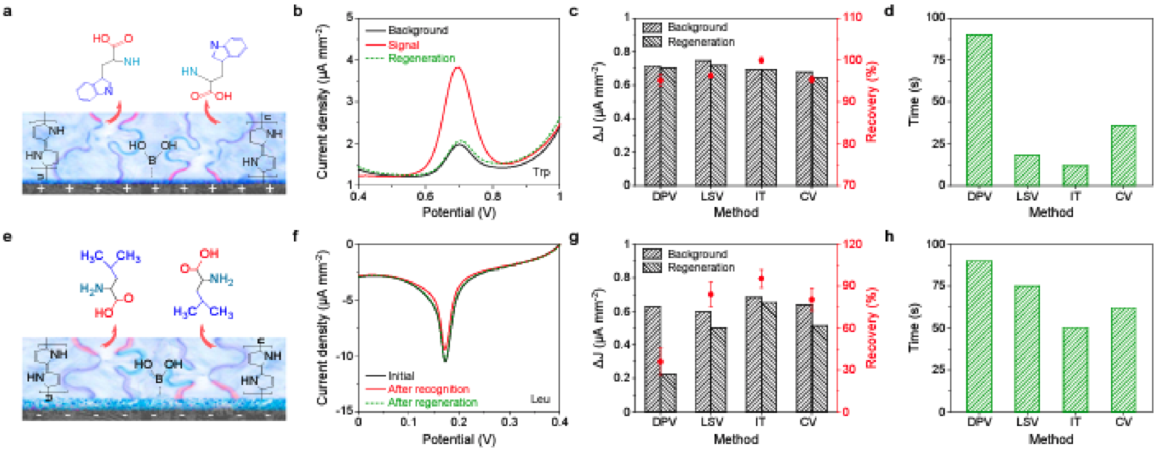

Figure B13: Characterizations of the LEG-MIP sensor regeneration. **a**, Schematic of the LEG-MIP sensor regeneration for direct electroactive molecule detection. **b**, DPV voltammograms of an LEG-MIP Trp sensor before and after regeneration in 50 μM Trp (IT under a fixed potential of 0.7 V for 12 s). **c**, Comparison of regeneration efficiency of the LEG-MIP Trp sensors using controlled voltammetry (i.e., DPV, LSV, IT, CV) after 12 s. **d**, Time consumption of the LEG-MIP Trp sensors to reach 100 % recovery. **e**, Schematic of the LEG-PB-MIP sensor regeneration for indirect detection. **f**, LSV voltammograms of an LEG- PB-MIP Leu sensor before and after regeneration in 50 μM Leu (IT under a fixed potential of -0.2 V for 50 s). **g**, Comparison of regeneration efficiency of the LEG-PB-MIP Leu sensors using controlled voltammetry (i.e., DPV, LSV, IT, CV) after 50 s. **h**, Time consumption of the LEG-PB-MIP Leu sensors to reach 80% signal change recovery. Error bars in **c** and **g** represent the s.d. from 3 sensors.

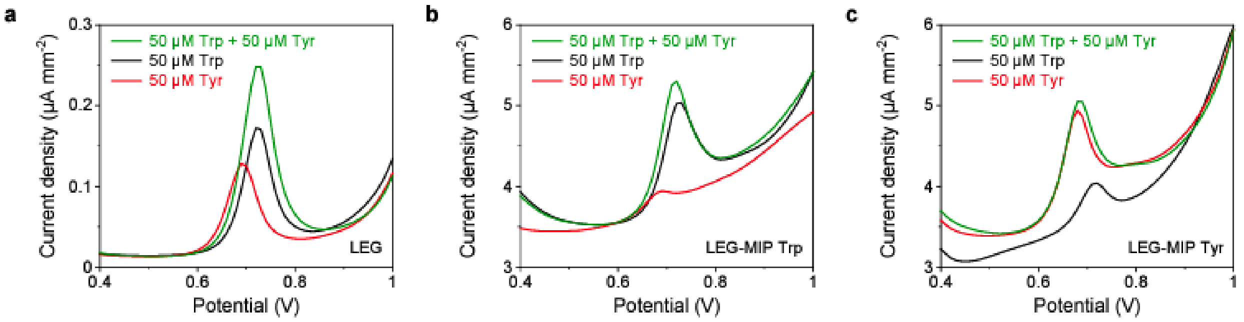

Figure B14: Selectivity studies of the LEG-MIP sensors for detecting two electroactive amino acids: Trp and Tyr. a–**c**, DPV voltammograms of a bare LEG electrode (**a**), an LEG-MIP Trp electrode (**b**), and an LEG-MIP Tyr electrode (**c**) in 50 µM Trp, 50 µM Tyr, and 50 µM Trp + 50 µM Tyr.

$$S = \frac{(B-J_2)-(B-J_1)}{Log_{10}C_2-Log_{10}C_1} * A$$

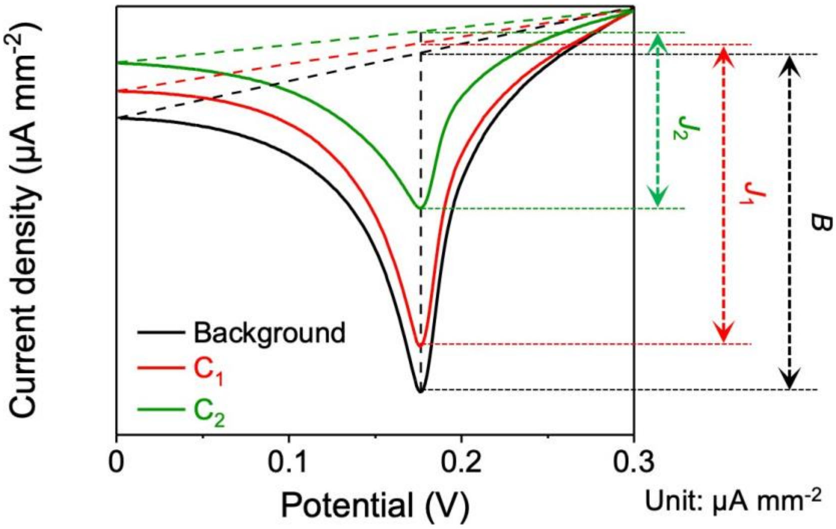

Figure B15: Schematic illustration of the sensitivity calculation of the LEG-RAR-MIP sensor. S, sensitivity of the sensor; B, background peak current height; A, the electrode area; J_1 and J_2: peak current height of the LSV obtained in the presence of the analyte with concentrations of C_1 and C_2, respectively.

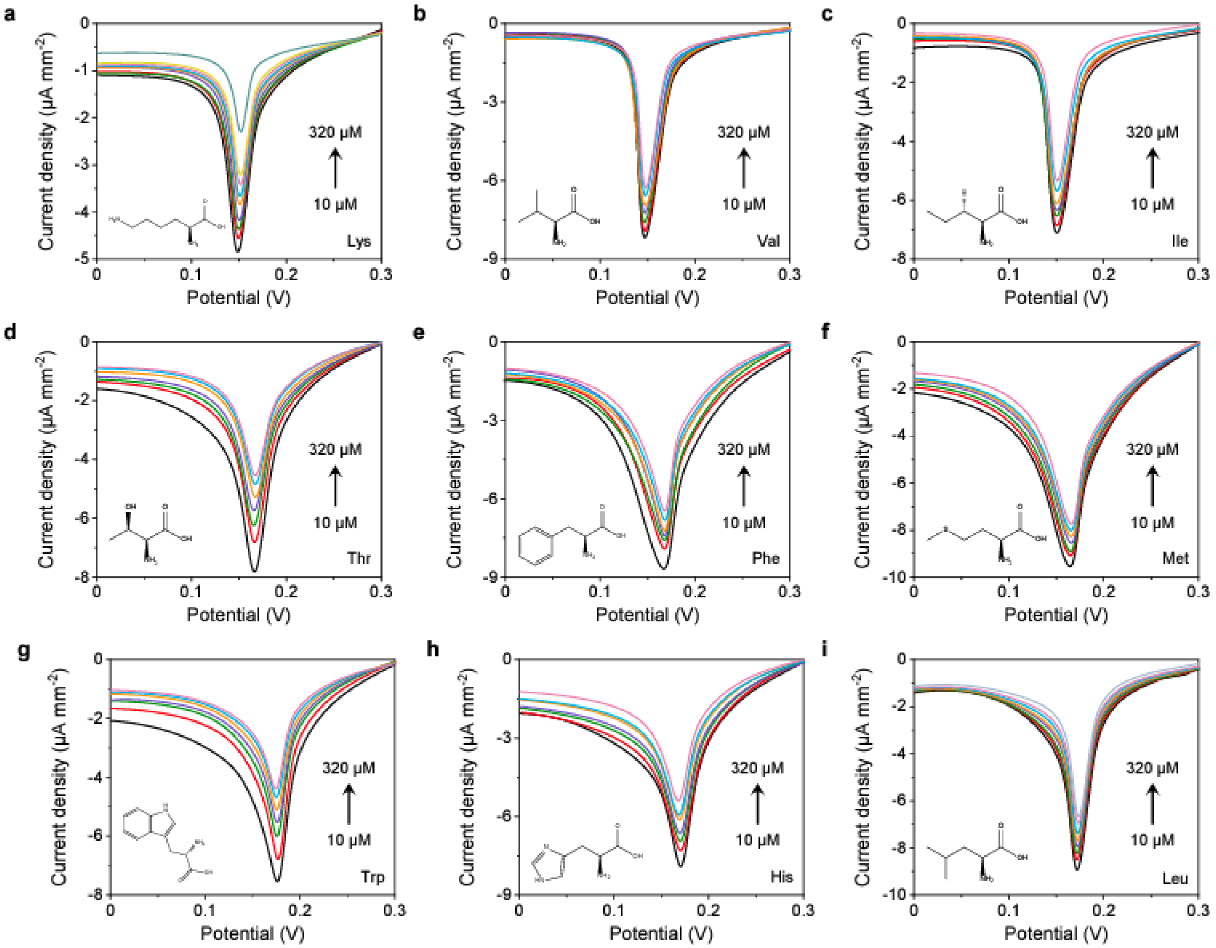

Figure B16: **LSV voltammograms of the LEG-PB-MIP sensors for indirect detection of all nine essential amino acids.**

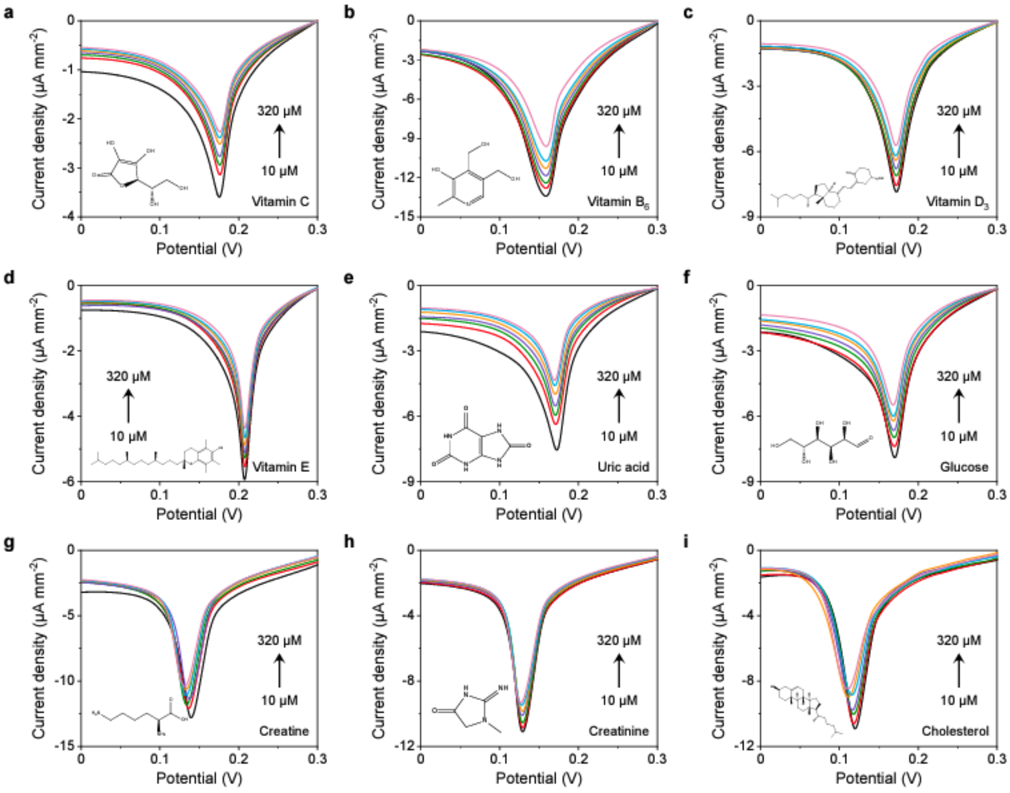

Figure B17: **LSV voltammograms of the LEG-PB-MIP sensors for indirect detection of multiple vitamins, metabolites, and lipids.**

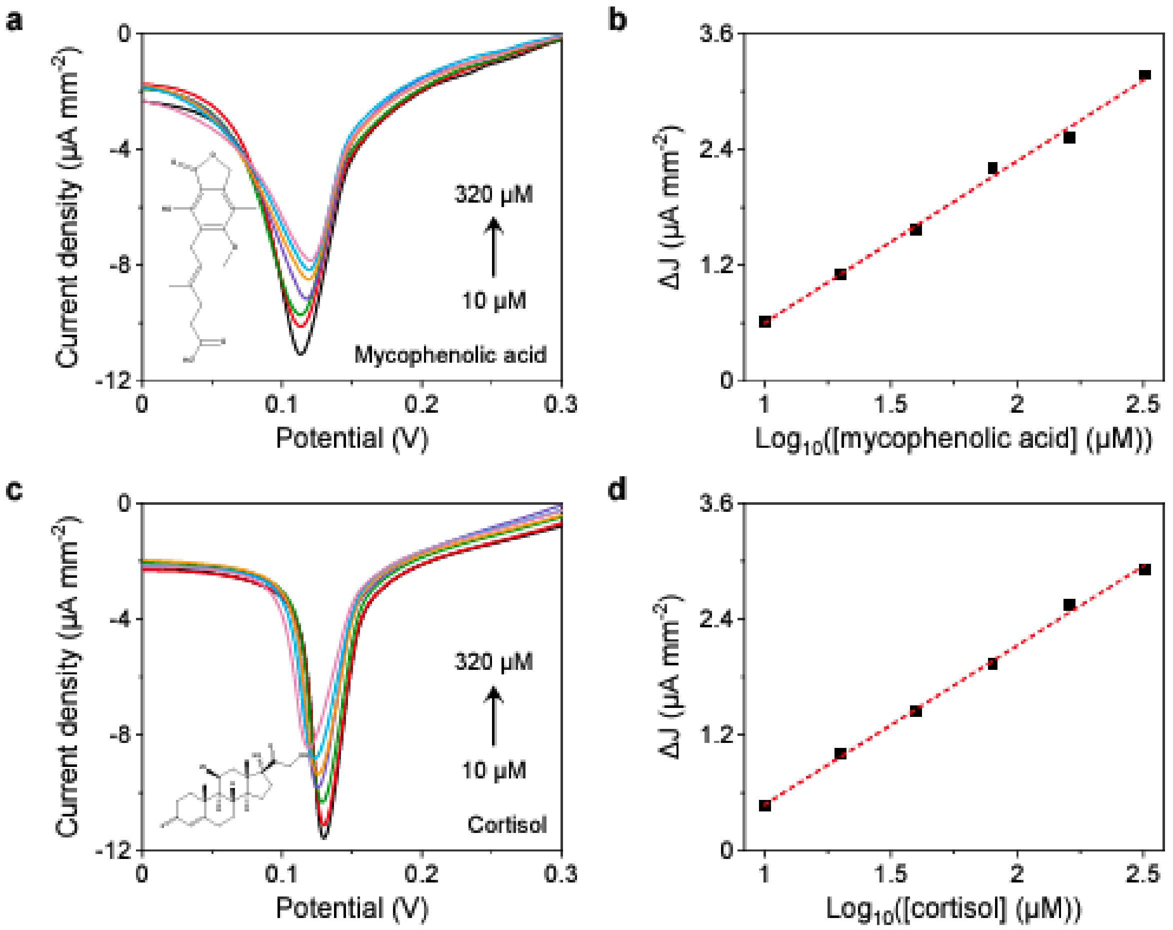

Figure B18: LSV voltammograms and the corresponding calibration curves of the LEG-PB-MIP sensor for indirect detection of cortisol and mycophenolic acid. Dashed lines in **b**,**d** represent linear fit trendlines.

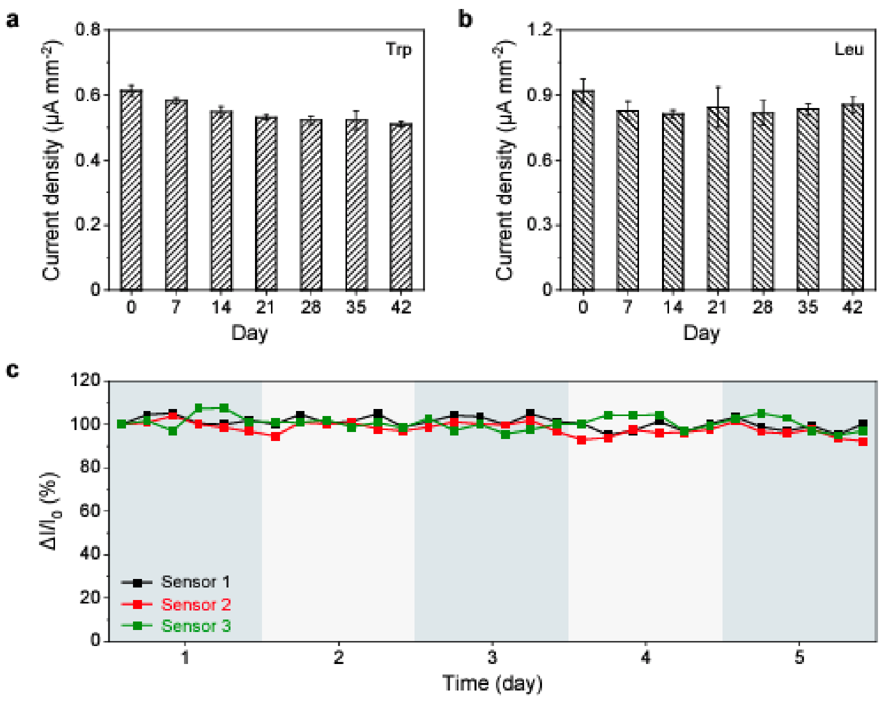

Figure B19: Characterization of the long-term storage stability of the LEG-MIP sensors. **a**,**b**, Current density of the peak height (ΔJ) of the LEG-MIP Trp sensors for detecting 50 µM Trp (**a**) and the LEG-PB-MIP Leu sensors for detecting 50 µM Leu (**b**) over a 6-week storage period. Error bars represent the s.d. from 3 sensors. **c**, Long term stability of the LEG-MIP for continuous use. Three different LEG-MIP Trp sensors were tested in parallel every hour for six consecutive hours a day over five consecutive days.

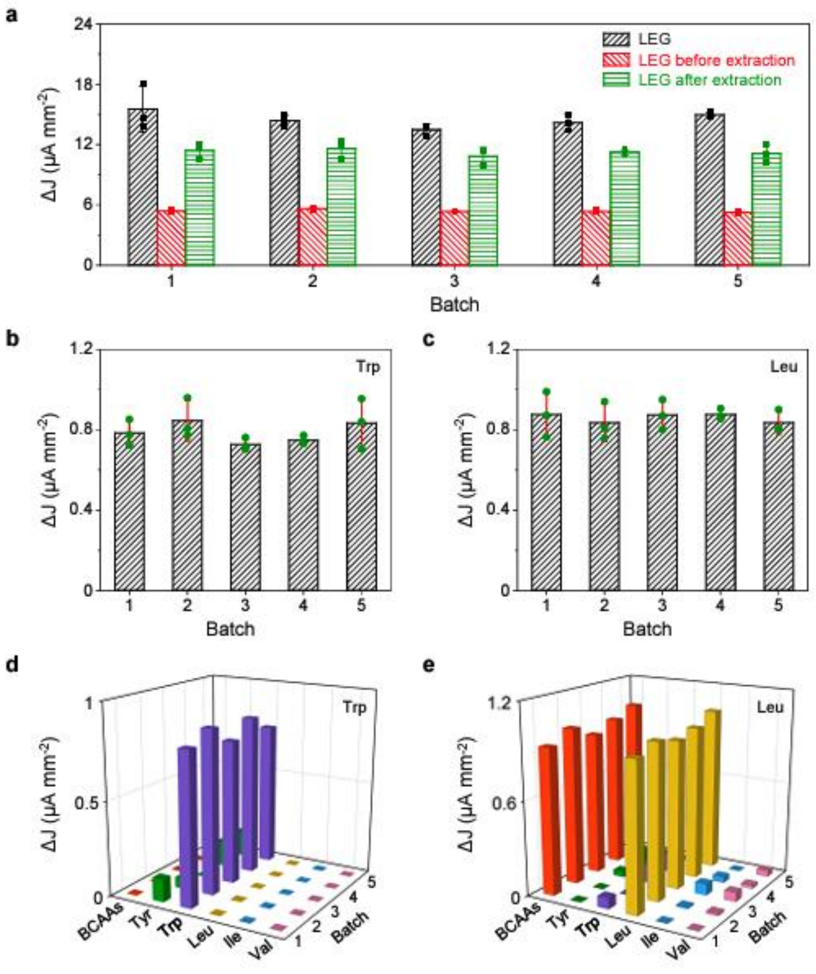

Figure B20: Characterization of the reproducibility of the LEG-MIP sensors from five different batches. **a**, Device-to-device variations in MIP film preparation on LEG. ΔJ represents current density of the peak height in the voltammograms (DPV here) of the LEG, the LEG-MIP before template (Trp) extraction, and the LEG-MIP after template (Trp) extraction in 0.1 M KCl solution containing 2.0 mM $K_4Fe(CN)_6/K_3Fe(CN)_6$ (1:1). Error bars represent the s.d. from 3 sensors. **b**,**c**, Sensitivity reproducibility of the LEG-MIP sensors. Batch-to-batch comparison of the sensitivity (ΔJ) of the Trp LEG-MIP sensors (**b**) and the Leu LEG-PB-MIP sensors (**c**) in the presence of 50 μM target. Error bars represent the s.d. from 3 sensors. **d**,**e**, Selectivity reproducibility of the LEG-MIP sensors. Batch-to-batch comparison of the selectivity of the Trp LEG-MIP sensors (**d**) and the Leu LEG-PB-MIP sensors (**e**) over other amino acids. 50 μM was used for each amino acid.

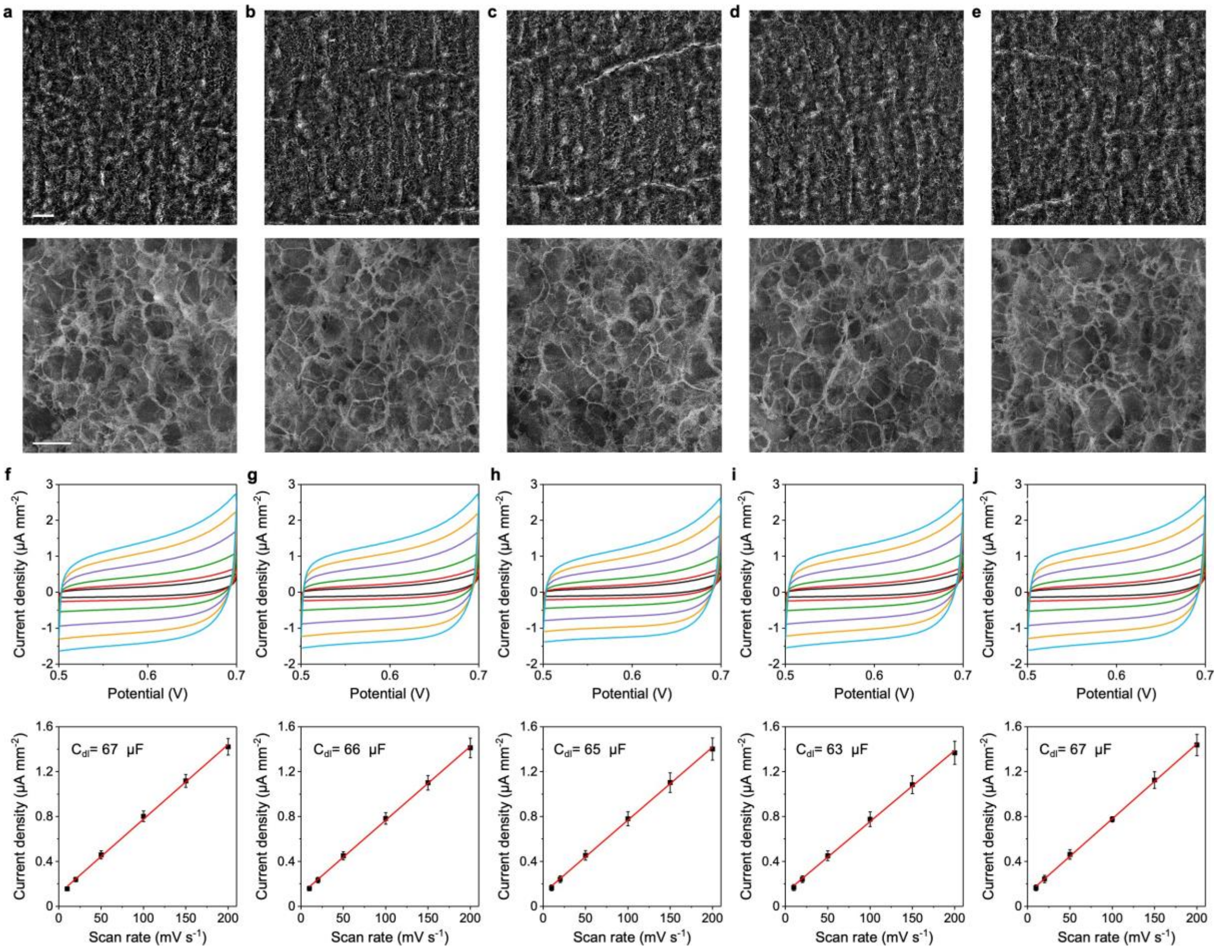

Figure B21: Microscopic and electrochemical characterization of the surface of the LEG- MIP electrodes. a–e, SEM characterization of the surface of LEG-MIP Trp electrodes from 5 different batches. Scale bars, 100 μm and 10 μm for upper and lower rows, respectively. **f–j**, Electrochemical characterization of the surface of LEG-MIP Trp electrodes from 5 different batches. C_{dl}, electrochemical double layer capacitance. Cyclic voltammograms were obtained for each LEG-MIP Trp electrode at the scan rates in PBS (pH 6.5). Current density in the calibration plot represents the oxidation current height at 0.6 V. Error bars represent the s.d. from 3 sensors. Solid lines in calibration plots represent linear fit trendlines.

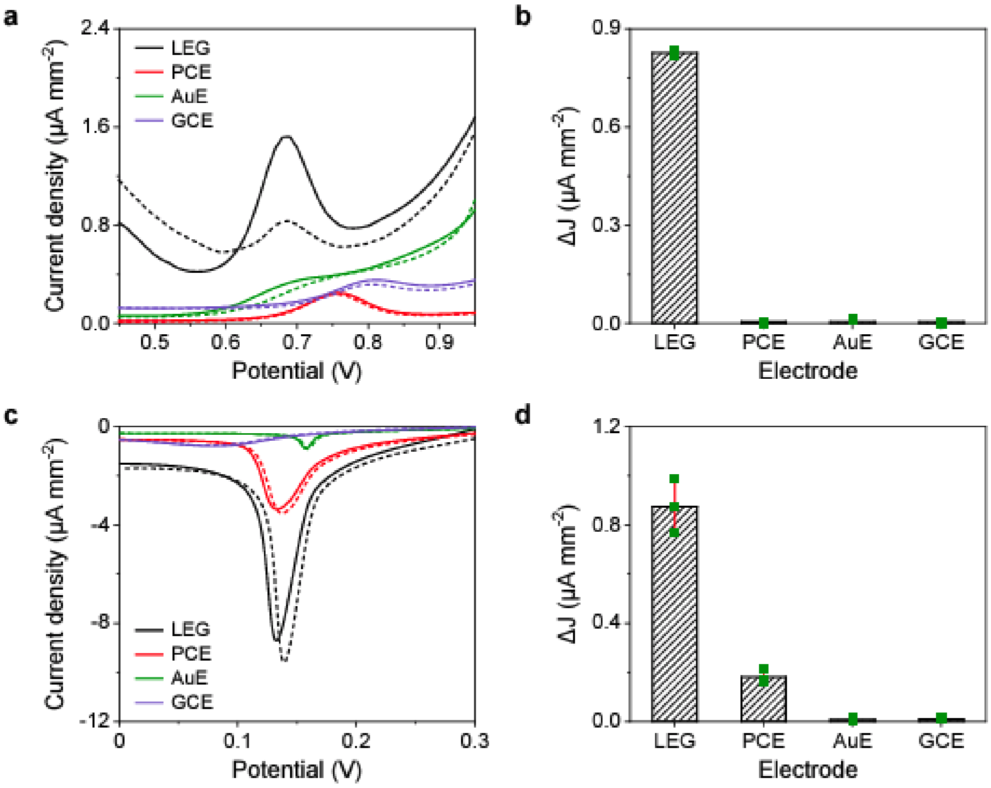

Figure B22: Comparison of the performance of the MIP sensors based on different electrodes: LEG, printed carbon electrode (PCE), Au electrode (AuE), and glassy carbon electrode (GCE). a,b, DPV voltammograms **(a)** and ΔJ (**b**) of the Trp MIP sensors before (dotted line) and after (solid line) incubation in 50 μM Trp. **c,d,** LSV voltammograms **(c)** and ΔJ (**d**) of the Leu PB-MIP sensors before (dotted line) and after (solid line) incubation in 50 μM Leu. Error bars represent the s.d. from 3 electrodes.

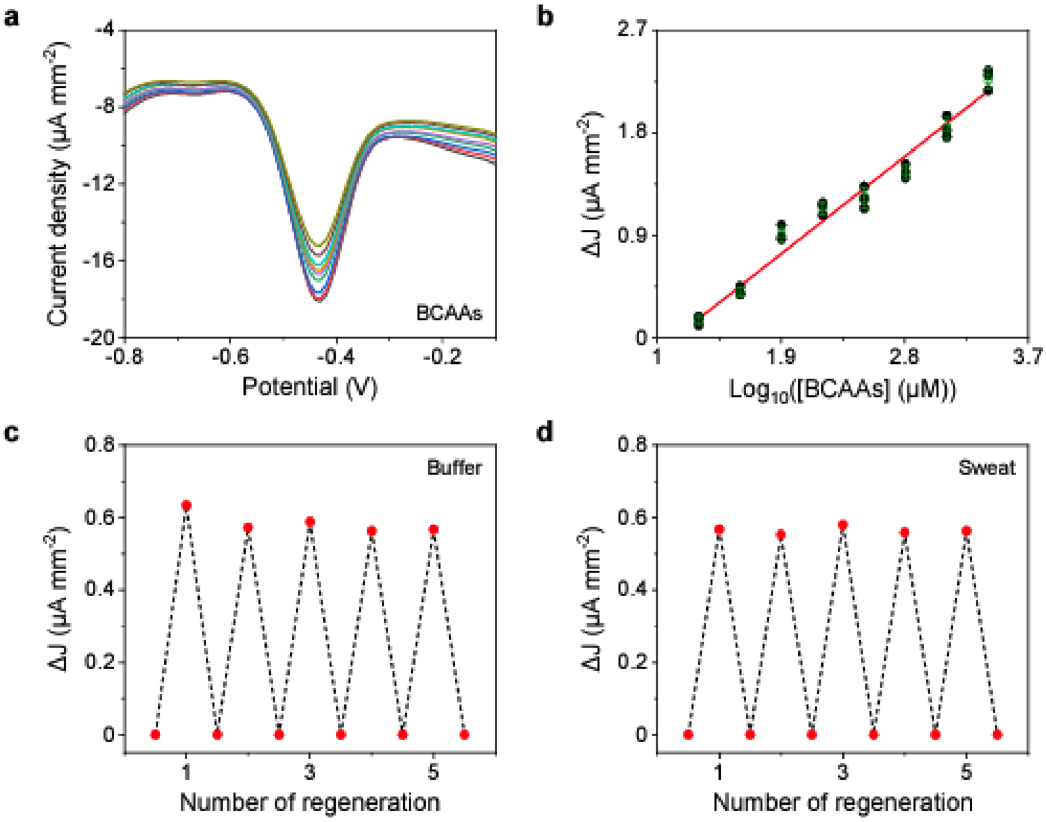

Figure B23: Characterization of the performance of the LEG-AQCA-multi-MIP BCAA sensor. a,**b**, Negative DPV voltammograms (**a**) and the corresponding calibration plot (**b**) of an LEG-AQCA- multi-MIP sensor for BCAA quantification. Error bars represent the s.d. from 3 sensors. Solid line in **b** represent a linear fit trendline. **c**,**d**, *In situ* regeneration of an LEG-AQCA-MIP BCAAs sensor in PBS buffer containing 60 µM total BCAAs (1:1:1) (**c**) and a raw sweat sample collected from a healthy subject (**d**).

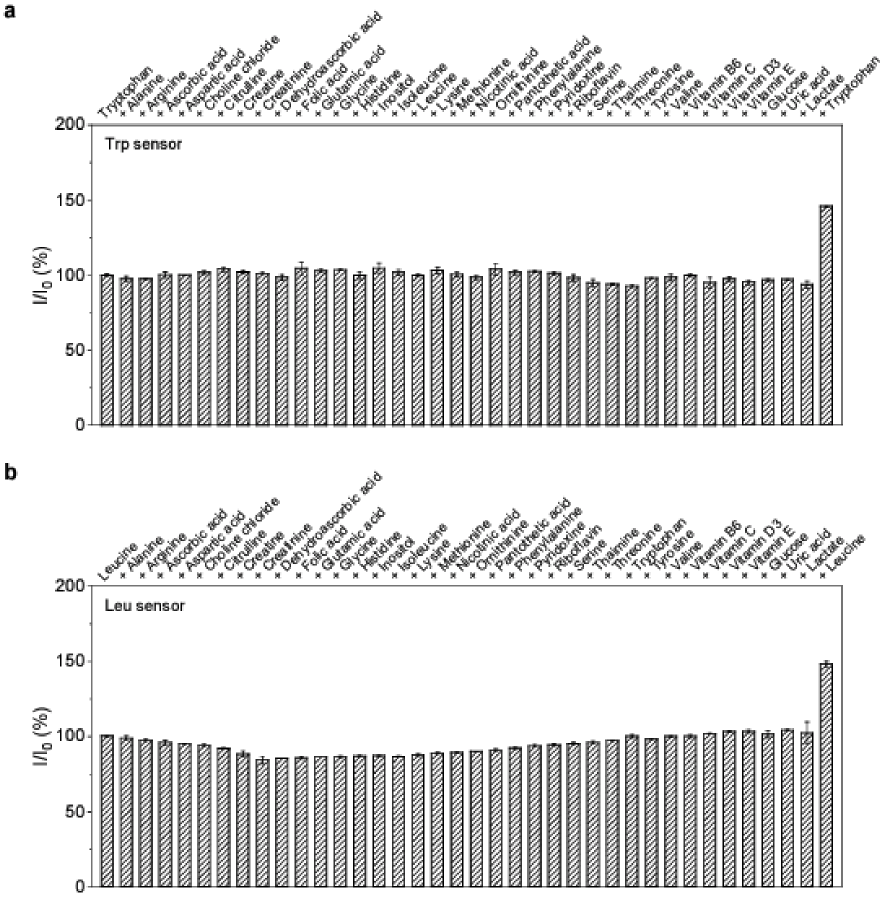

Figure B24: Selectivity of the LEG-MIP Trp sensors and the LEG-PB-MIP Leu sensors over other major analytes in human sweat. a,**b**, The selectivity of the Trp LEG-MIP sensors (**a**) and the Leu LEG-MIP sensors (**b**). I and I_0 represent the peak amplitude obtained from the LEG-MIP sensors, and the average peak amplitude obtained from the starting target solution, respectively. The concentrations of the initial Trp, Leu and other sweat analytes are based on **Supplementary Table 2**. Trp and Leu concentrations were increased by 50% in the end. Error bars represent the s.d. from 3 independent measurements.

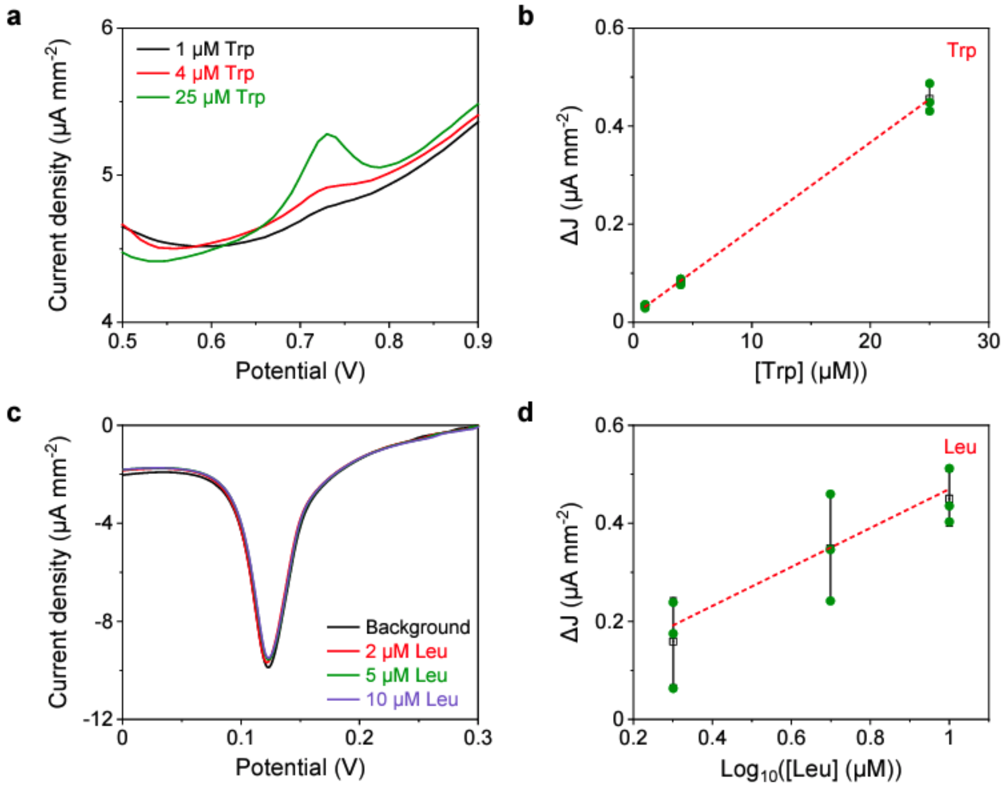

Figure B25: **Evaluation of the LEG-MIP sensor for low concentration amino acid analysis.** Error bars represent the s.d. from 3 sensors. Dashed lines in b,d represent linear fit trendlines.

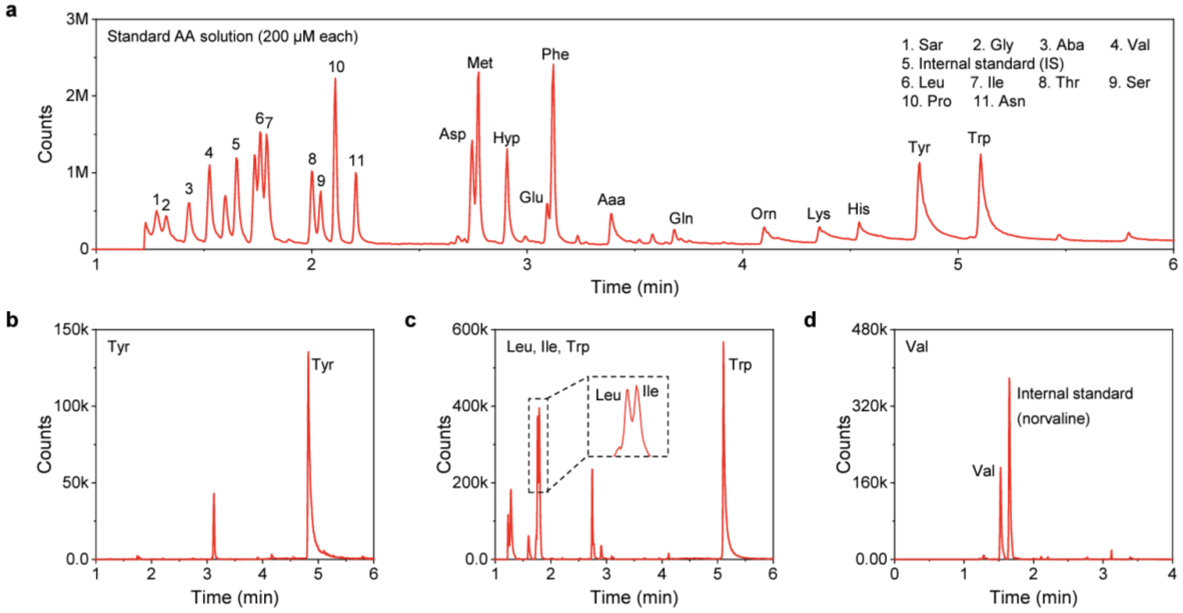

Figure B26: GC-MS analyses of the Tyr, Try, Leu, Ile and Val in standard analyte solution. Each amino acid (200 µM added) displays a characteristic specific peak at its specific ion number. **a**, Merged spectrum of all ion numbers displaying all amino acids detectable by the EZ:Faast amino acid kit. **b**, Characteristic peak of Tyr in Ion 164. **c**, Characteristic peak of Leu, Ile and Trp in Ion 130. **d**, Characteristic peak of Val in Ion 158.

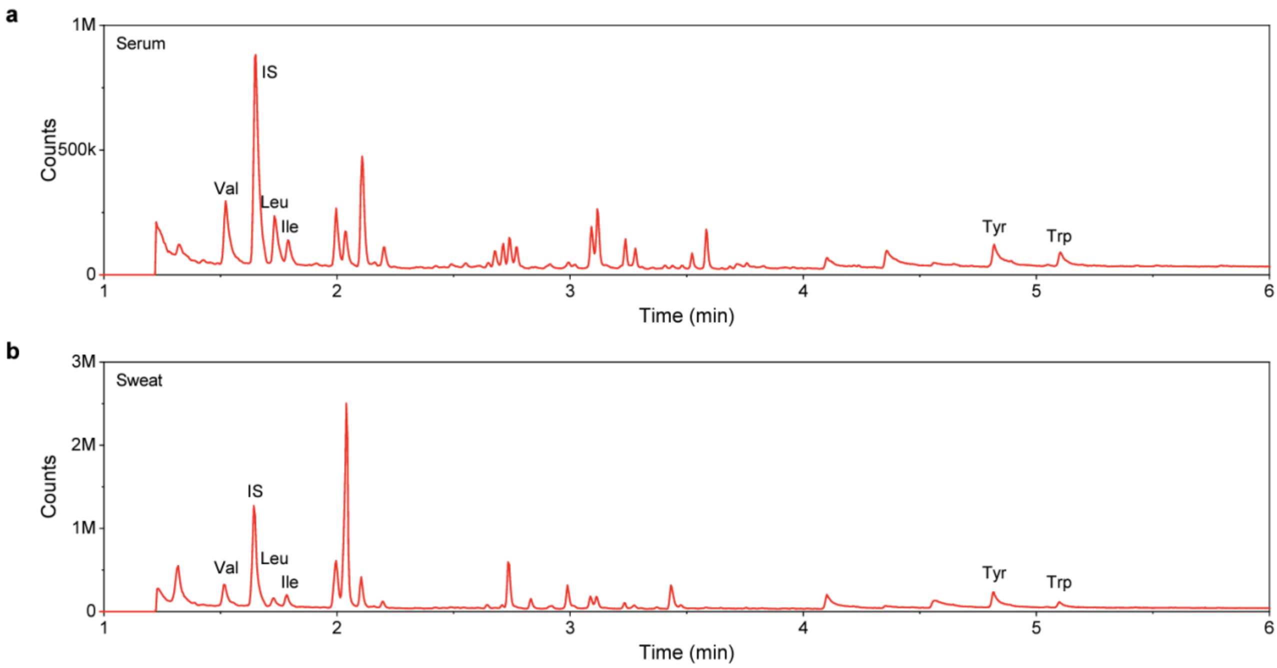

Figure B27: GC-MS analyses of human sweat and serum samples collected at the same time. Serum and sweat samples are diluted for 4 and 6.66 times, respectively. Merged spectra of all ion numbers are shown here. Compared to sweat, merged spectra of all ion numbers in serum displayed more peaks showing more amino acid peaks.

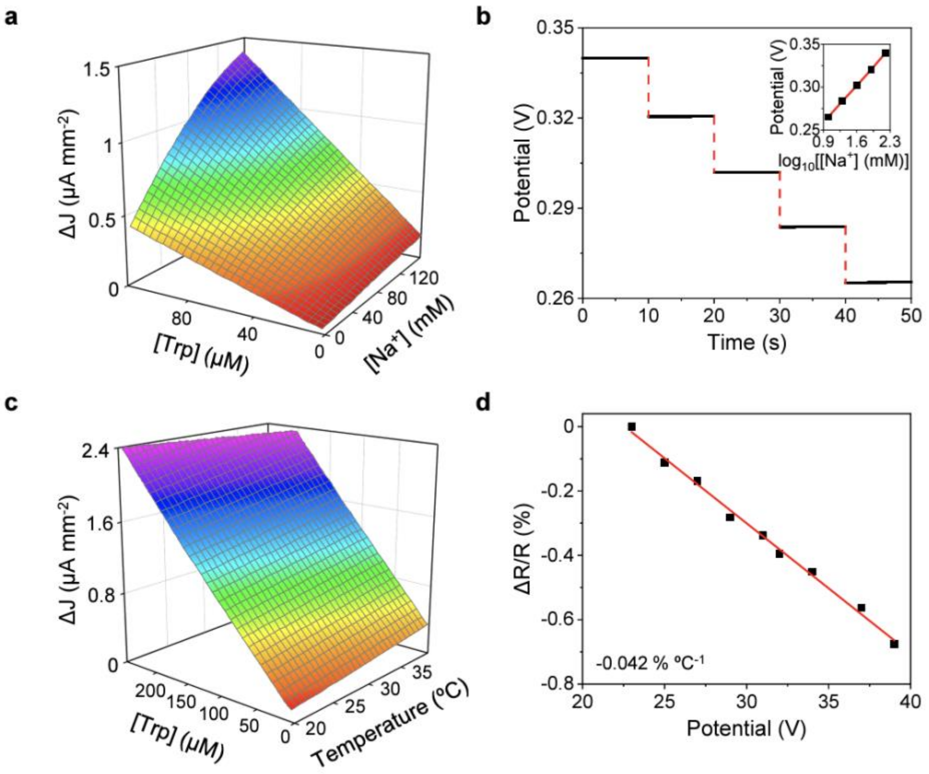

Figure B28: The performance of the LEG-MIP sensor under varied temperature and electrolyte levels. a, Color map showing the dependence of the LEG-MIP Trp sensor response on Trp and Na^+ concentrations. **b**, Open circuit potential responses of an LEG-based Na^+ sensor in the presence of varied Na^+ concentrations. Inset, calibration plot of an LEG-based Na^+ sensor. **c**, Color map showing the dependence of the LEG-MIP Trp sensor response on Trp and temperature. **d**, Calibration plot of an LEG- based temperature sensor in the physiological temperature range. Solid calibration lines in **b**,**d** represent linear fit trendlines.

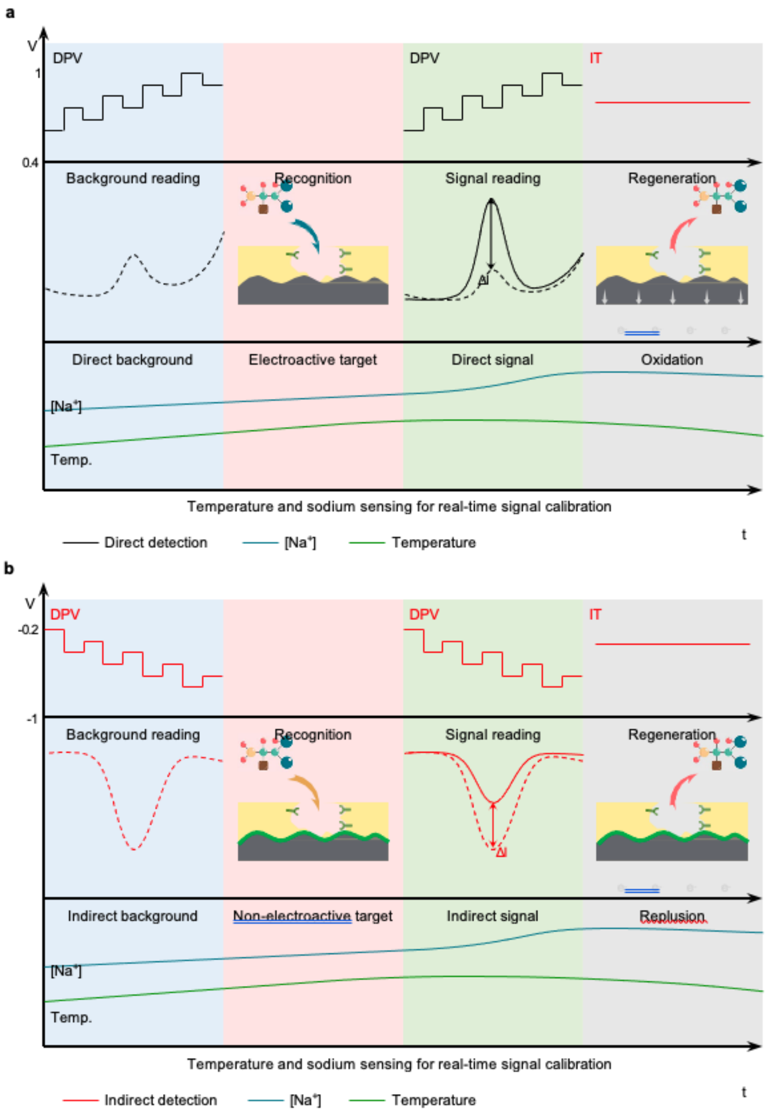

Figure B29: *In situ* calibration strategies of the wearable LEG-MIP sensors involving a two-step DPV-scan calibration and real-time temperature/electrolyte calibrations. (**A** and **B**) *In situ* calibration strategies of the MIP-LEG sensor with direct detection mechanism (**a**) and the MIP-RAR (AQCA used here for wearable sensing)-LEG sensor with indirect detection mechanism (**b**) to obtain accurate reading continuously during on-body use.

Bibliography for Appendix B

1. Liu, Y.-C., Hwang, B.-J., Jian, W.-J. & Santhanam, R. In situ cyclic voltammetry-surface-enhanced Raman spectroscopy: studies on the doping–undoping of polypyrrole film. Thin Solid Films 374, 85–91 (2000).

2. Huang, B. et al. Electrochemical sensing platform based on molecularly imprinted polymer decorated N,S co-doped activated graphene for ultrasensitive and selective determination of cyclophosphamide. Talanta 164, 601–607 (2017).

3. Sharma, P. S., Pietrzyk-Le, A., D’Souza, F. & Kutner, W. Electrochemically synthesized polymers in molecular imprinting for chemical sensing. Anal. Bioanal. Chem. 402, 3177–3204 (2012).

4. Neese, F. Software update: the ORCA program system, version 4.0. WIREs Comput. Mol. Sci. 8, e1327 (2018).

5. Dechtrirat, D. et al. An electrochemical MIP sensor for selective detection of salbutamol based on a graphene/PEDOT:PSS modified screen printed carbon electrode. RSC Adv. 8, 206–212 (2018).

Chapter 6: Printable molecule-selective core-shell nanoparticles for wearable and implantable sensing

This chapter is temporarily embargoed

Chapter 7: Future and Outlook

This chapter is temporarily embargoed.

Bibliography

This chapter is temporarily embargoed